# Validation of a three-dimensional Depth-Semi-Averaged model

M. Antuono,[1, a)] S. Valenza,[2, 1] C. Lugni,[1, 3] and G. Colicchio[1, 3]

[1)] *CNR-INM, Institute of Marine Engineering, Rome, Italy*

[2)] *University of Rome "Sapienza", Rome, Italy*

[3)] *AMOS, NTNU, Dept. of Marine Technology, Trondheim, Norway*

(Dated: 15 January 2019)

The present work completes the validation of the Depth-Semi-Averaged model defined in [M. Antuono, G. Colicchio, C. Lugni, M. Greco, M. Brocchini, "A depth semi-averaged model for coastal dynamics", Physics of Fluids 29, 056603 (2017)] providing a numerical implementation in three spatial dimensions. In particular, the model is aimed at describing a wide variety of phenomena typical of the coastal region, as for example nonlinear interaction between waves and the bottom bathymetry (diffraction/refraction phenomena), dispersion effects and beach inundation. To this purpose, the proposed scheme is tested against benchmark experimental data available in the literature for wave propagation problems in both intermediate and shallow water conditions. A final simulation is carried on by considering a tsunami wave running over a prototype bathymetry resembling a bay-promontory coastline. Different widths of the bay have been considered, describing their influence on the run-up dynamics.

PACS numbers: 47.35.Bb

Keywords: gravity waves, non-hydrostatic models, Boussinesq models, depth-averaged models

[a)] Electronic mail: matteo.antuono@cnr.it

## I. INTRODUCTION

The modelling of the wave dynamics from deep water towards the surf and nearshore region represents a challenging problem in fluid dynamics, for it includes several theoretical and numerical complexities. The theoretical issues concern the definition of models able to describe the main features of wave propagation, namely non-linearity, dispersion, shoaling, refraction and diffraction, and provide a simplified description of the flow dynamics, i.e. retaining just the spatial- and time-scales of interest. This generally leads to closure problems that need to be properly modelled. At this stage, the almost unavoidable use of approximations causes an inaccurate prediction of dispersive effects when the wave propagation occurs in intermediate/deep-water conditions. Numerical issues lie in the construction of a robust and accurate scheme capable to conciliate both nonlinear and dispersive effects, the latter being non-negligible as waves propagate in intermediate/deep water condition.

Because of the need of a simplified description, the most widespread models for coastal dynamics are obtained through integration over the water depth of Laplace, Euler or Navier-Stokes equations, assuming that the horizontal dynamics predominates the vertical one. The main drawback of the above approach is that the depth-averaged equations cannot be completely represented through depth-averaged quantities, namely the water depth and the depth-averaged velocity field. Consequently, some approximations are needed to achieve a closed system of equations.

The simplest system is represented by the Nonlinear-Shallow Water Equations that include the principal nonlinear terms (see, for example, Toro[1], Antuono and Brocchini[2, 3], Bjørnestad and Kalisch[4]) but, in turn, completely disregard the dispersive effects. A correct inclusion of dispersion is of fundamental importance when the wave motion occurs in intermediate depths, and, for these reasons, the Boussinesq-type equations are usually preferred to the NSWEs. These equations are obtained through a sort of asymptotic expansion of the depth-averaged terms in the parameter $\mu$ (i.e. the ratio between the vertical and horizontal reference lengths) and constitute a wide family of models with different features, according to the accuracy of the adopted expansion (for an extensive review on Boussinesq models we address the interested readers to Brocchini[5], Kirby[6]). Despite their ability of providing a satisfactory description of the wave dynamics in the nearshore region,

the Boussinesq-models show both theoretical and numerical limits. As discussed in Madsen et al.[7], the exact linear dispersion relation can be only attained through the use an infinite number of terms in the asymptotic expansion. Further, each order of the expansion leads to the presence of terms with high-order derivatives (generally fifth or seventh order) that represent a critical issue for the numerical implementation.

The need to overcome the above issues led to the definition of a novel class of models that retain, partially or completely, the vertical dynamics. Despite the increased computational cost with respect to Boussinesq schemes, these approaches allow for a theoretically sound description of both nonlinear and dispersive effects and for a simpler and more robust numerical implementation (generally, third-order derivatives appear). These schemes are usually called non-hydrostatic models, since the pressure field is not just the leading-order hydrostatic contribution and, therefore, require the solution of a Poisson equation for the dynamics pressure component (see, for example, Yamazaki et al.[8], Zijlema and Stelling[9], Ma et al.[10], Lu and Xie[11], Raoult et al.[12]).

The Depth-Semi-Averaged scheme proposed in Antuono and Brocchini[13] belongs to such a class of models but, differently from those based on the solution of a Poisson equation for the dynamic pressure field, it relies on the solution of a Poisson equation for the vertical velocity component or, alternatively, for its semi-integrated value $\Upsilon$. In particular, the use of the latter variable has several advantages, as shown in Antuono et al.[14]. From a theoretical point of view, it provides a closed formulation, since both the forcing term and the boundary conditions of the Poisson equation are expressed in terms of the principal depth-averaged quantities. This avoids the use of simplifications/approximations and, in fact, the model described in Antuono et al.[14] results in a rearrangement of the Navier-Stokes equations. From a numerical point of view, the use of $\Upsilon$ allows for a robust and accurate implementation, in comparison to the use of the Poisson equation for the vertical velocity component.

In the present work we complete the analysis started in Antuono et al.[14] (that was limited to two-dimensional benchmarks) by extending the validation of the model with experimental data for three-dimensional problems. A final simulation of the run-up of a solitary wave over a prototype bay-promontory coastline is considered as a proof of concept of the ability of the proposed scheme in describing the wave dynamics in the coastal region.

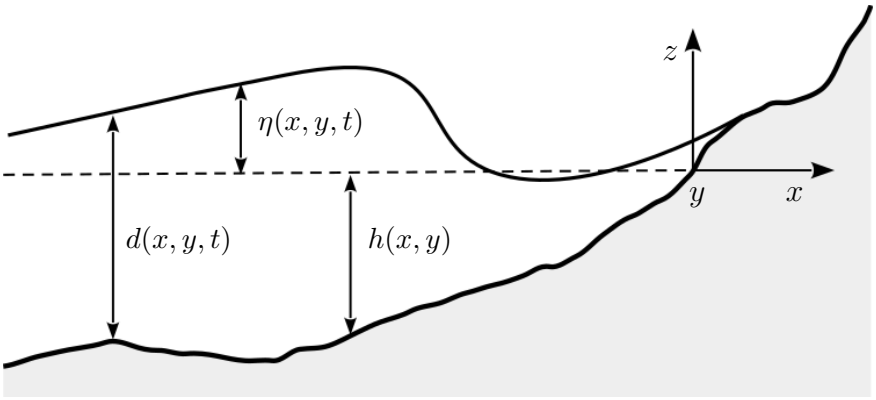


FIG. 1. Sketch of the coastal flow geometry (the $y$-axis points in the transverse direction, forming a right-handed Cartesian frame of reference). The horizontal dashed line indicates still water level.

## II. THE DEPTH-SEMI-AVERAGED MODEL

Here we briefly recall the structure of the Depth-Semi-Averaged model proposed in Antuono et al.[14] (hereinafter referred to as *DepSeA* model). Incidentally, we highlight that the theoretical model described in Antuono et al.[14] was already derived in three dimensions while the numerical validation was only performed against two-dimensional benchmarks. In the following description we neglect all the turbulent and vortical terms, as well as the friction along the bottom. In fact, these effects generally play a secondary role in the time-scale of the problems considered hereinafter (see, for example, Alberello et al.[15]).

The *DepSeA* model is obtained through a proper rearrangement of the Semi-Integrated model proposed by Antuono and Brocchini[13]. The resulting constitutive equations are written in the following compact form:

$$d_t + \nabla \cdot \boldsymbol{Q} = 0\,, \tag{1a}$$

$$\boldsymbol{M}_t + \nabla \cdot \mathbb{F} = (g\,d + p_b)\,\nabla h\,, \tag{1b}$$

$$\Upsilon_{xx} + \Upsilon_{yy} + \Upsilon_{zz} = \nabla \cdot \left(\frac{\boldsymbol{M}}{d}\right), \tag{1c}$$

where $g$ is the gravitational acceleration, $\nabla = (\partial/\partial x,\, \partial/\partial y)$ is the two-dimensional gradient operator, and $d$ denotes the total water depth. Figure 1 displays a sketch of a typical beach nearshore problem and indicates the main geometrical variables. The $z$-coordinate

points upward and the tern $(x, y, z)$ forms a right-handed Cartesian reference frame (in the figure $y$ acts in transverse direction). In particular, $d = \eta + h$ where $\eta$ is the wave elevation with respect to the still water level (set at $z = 0$) and $h$ is the sea bottom level (assumed to be independent of time). Equations (1a) and (1b) express conservation of fluid mass and momentum, and represent a depth-averaged subset that is similar to the common Boussinesq-type equations. Equation (1c) is a Poisson equation that accounts for the three-dimensional dynamics, and is used to derive the dispersive contributions. Here, $\Upsilon$ represents the semi-averaged vertical velocity component (i.e. averaged over a portion of the water column) and $\boldsymbol{M}$ is the generalized mass flux. These are given by the following expressions:

$$\Upsilon \,=\, \int_z^\eta w \, d\zeta \,, \qquad \boldsymbol{M} \,=\, \boldsymbol{Q} \,+\, \int_{-h}^\eta \nabla\Upsilon \mathrm{d}z \,, \tag{2}$$

where the variable $w$ denotes the vertical component of the velocity field. As usual, $\boldsymbol{Q} \,=\, (U_1 d, U_2 d)$ indicates the mass flux vector, and $\boldsymbol{U} \,=\, (U_1, U_2)$ is the depth-averaged velocity vector in the horizontal plane. All terms associated with linear dispersion are included inside the generalized mass flux $\boldsymbol{M}$ through the integral of $\nabla\Upsilon$. Note that the structure of the momentum equations is similar to that of many Boussinesq-type models (see, for example, Wei et al.[16], Shi et al.[17]) and avoids the presence of time derivatives in the flux tensor $\mathbb{F}$. Meanwhile, the flux term includes the remaining dispersive contributions and the classic shallow-water terms:

$$\mathbb{F} = \left( \frac{g\, d^2}{2} \,+\, D_{isp} \right) \mathbb{1} + \left( d\, \boldsymbol{U} \otimes \boldsymbol{U} + \int_{-h}^\eta (\delta\boldsymbol{u} \otimes \delta\boldsymbol{u}) \, \mathrm{d}z \right) , \tag{3}$$

where $\otimes$ indicates the dyadic product and $\delta\boldsymbol{u}$ represents the deviation of the horizontal velocity field, namely $\boldsymbol{u} = (u_1, u_2)$, with respect to the depth-averaged field $\boldsymbol{U}$. These are linked through the following relations:

$$\boldsymbol{u} \,=\, \boldsymbol{U} \,+\, \delta\boldsymbol{u} \,, \qquad \delta\boldsymbol{u} \,=\, -\,\nabla\Upsilon \,+\, \frac{1}{d}\int_{-h}^\eta \nabla\Upsilon \mathrm{d}z \,. \tag{4}$$

The term $D_{isp}$ contains the non-linear dispersive contributions arising from the integral of the dynamic pressure:

$$D_{isp} \,=\, \nabla \cdot \left( \int_{-h}^\eta \int_z^\eta w\, \boldsymbol{u} \, \mathrm{d}\zeta \right) \,-\, \int_{-h}^\eta w \, (w + \boldsymbol{u} \cdot \nabla h) \, \mathrm{d}z \,. \tag{5}$$

Finally, $p_b$ is given below as:

$$p_b \,=\, \nabla \cdot \left( \int_{-h}^\eta w\, \boldsymbol{u} \, \mathrm{d}\zeta \right) \tag{6}$$

The boundary conditions for the Poisson equation are:

$$\begin{cases} \left.\dfrac{\partial \Upsilon}{\partial n}\right|_{z=-h} = -\left[h_t + \dfrac{\boldsymbol{M}}{d}\cdot\nabla h\right] \Big/ \sqrt{1+\|\nabla h\|^2}\,, \\ \\ \Upsilon|_{z=\eta} = 0\,, \qquad \left.\dfrac{\partial \Upsilon}{\partial n}\right|_{\mathscr{D}_L} = c_N\,, \end{cases} \tag{7}$$

where $\mathscr{D}_L$ denotes the lateral boundary of the fluid domain and $c_N$ is the assigned condition along such a boundary. We highlight that both the forcing term of the Poisson equation and the boundary condition along the bottom are expressed in terms of $\boldsymbol{M}$ and $d$ and, therefore, provide a closed formulation for the system (1a)-(1c). In fact, the knowledge of $\Upsilon$ allows for the computation of $w$ and $\delta\boldsymbol{u}$ through equations (2) and (4), and, then, of all remaining terms.

Regarding the numerical implementation, this follows the scheme described in Antuono et al.[14]. In particular, a fourth-order finite-volume discretization based on an HLL-MUSCL-Hancock scheme and a fourth-order Adams-Bashforth-Moulton predictor/corrector algorithm for the time integration are used to solve the depth-averaged subset made up by equations (1a) and (1b). Conversely, a second-order finite-difference discretization with a diffuse-boundary approach is implemented for the Poisson equation (1c). A Cartesian grid is used to solve both the depth-averaged subset and the Poisson equation. The time stepping is computed through the formula below:

$$\Delta t = C_{cfl}\,\min\left\{ \min_i\left[\frac{\Delta x_i}{|U_{1,i}|+\sqrt{g d_i}}\right],\ \min_i\left[\frac{\Delta y_i}{|U_{2,i}|+\sqrt{g d_i}}\right]\right\} \tag{8}$$

where $(\Delta x_i, \Delta y_i)$ denotes the grid spacing of the $i$-th cell in the $x$- and $y$-direction respectively and $C_{cfl}$ is the Courant-Friedrichs-Lewy number, here set equal to 0.4. In the Appendices A and B, we report some details about the solution for $\Upsilon$ in shallow water conditions and the treatment of the wet/dry interface.

## A. Some theoretical insights

It is interesting to investigate the physical meaning of the terms $\boldsymbol{M}$ and $\Upsilon$, for they are closely related to the free surface dynamics. Here, we assume that flow is irrotational and that the velocity field is expressed through the (three-dimensional) gradient of the potential

$\phi$, namely:

$$\boldsymbol{v} \,=\, (\, u_1,\, u_2,\, w\,) \,=\, \hat{\nabla}\phi\,, \quad \text{where} \quad \hat{\nabla} = (\, \partial/\partial x,\, \partial/\partial y,\, \partial/\partial z\,)\ . \tag{9}$$

Using the definition of $\Upsilon$ in equation (2), we immediately find:

$$\Upsilon \,=\, \phi_F \,-\, \phi\,, \tag{10}$$

where the subscript 'F' is hereinafter used to denote the quantities evaluated along the free surface $\eta$. This means that $\Upsilon$ accounts for the difference between the potential along the free surface and the potential inside the fluid domain. Applying the two-dimensional gradient to equation (10), we obtain:

$$\nabla\Upsilon \,=\, \nabla\phi_F \,-\, \nabla\phi \,=\, (\, \boldsymbol{u}_F \,+\, w_F\,\nabla\eta\,) \,-\, \boldsymbol{u}\,, \tag{11}$$

where $\boldsymbol{u} = (u_1, u_2)$, as usual. Finally, substituting the above expression in the definition of $\boldsymbol{M}$ in equation (2), we also find:

$$\boldsymbol{M} \,=\, d\,(\, \boldsymbol{u}_F \,+\, w_F\,\nabla\eta\,)\ . \tag{12}$$

Therefore, the generalized mass flux $\boldsymbol{M}$ contains a contribution due to the horizontal velocity components at the free-surface and a further contribution generated by the deformation of such an interface due to the vertical velocity component $w_F$. In shallow-water conditions this latter term is expected to be negligible while the former one reduces to $\boldsymbol{Q}$, since $\boldsymbol{u}_F \simeq \boldsymbol{U}$. On the contrary, both terms are non-negligible as waves travel seaward. Incidentally, we highlight that, differently from $\boldsymbol{M}$, the mass flux $\boldsymbol{Q}$ becomes less significant as waves propagate in deep water. In this condition, indeed, the depth-averaging procedure is performed over a fluid region where, for a large extent, the velocity is practically null.

## III. APPLICATIONS

In the present Section we test the proposed three-dimensional model against typical problems of wave propagation in both intermediate and shallow water conditions. We introduce here the following dispersive and nonlinear dimensionless parameters:

$$\mu \,=\, 2\pi\,\frac{h_0}{L}\,, \qquad \epsilon \,=\, \frac{H}{h_0}\,, \tag{13}$$

where $L$ is the wave length, $h_0$ is the reference water depth (generally, the still water depth) and $H$ is the wave height. These parameters will be used in the continuation to characterize the problems under consideration.

## A. Wave transformation over an elliptical shoal on a sloped bottom

Here, we consider the experiment conducted by Berkhoff et al.[18] in the wave basin of the Delft Hydraulics Laboratory on the propagation of regular waves over an elliptical shoal placed along a sloping bottom. This benchmark is widely used for testing the ability of 3D propagation models in simulating wave diffraction and refraction over uneven bathymetry. More information about the measurements can be found in Report W 154-VIII of the Delft Hydraulics Laboratory.

In the experiment the wave tank was approximately 25 m long ($x \in$ [-15, 10] m) and 20 m wide ($y \in$ [-10, 10] m). A submerged elliptical shoal was located over a plane beach with slope 1:50 connecting two uniform-depth regions of 0.45 $m$ and 0.1 $m$. The slope-oriented coordinates ($x'$, $y'$) were rotated by $-20°$ with respect to the global coordinate system ($x$, $y$) and both frames of reference had their origin at the centre of the elliptical shoal. In particular, the minor semi-axis of the ellipse was equal to 3 $m$ while its major semi-axis was equal to 4 $m$. The boundary of the shoal was given by:

$$\left(\frac{x'}{3}\right)^2 + \left(\frac{y'}{4}\right)^2 = 1 \tag{14}$$

where

$$\begin{cases} x' = x\,\cos(\alpha) + y\,\sin(\alpha)\,, \\ y' = x\,\sin(\alpha) - y\,\cos(\alpha)\,, \end{cases} \tag{15}$$

with $\alpha = -20°$. The thickness of the shoal was:

$$d'(x', y') = -0.30 + 0.50\sqrt{1 - \left(\frac{x'}{3.75}\right)^2 - \left(\frac{y'}{5}\right)^2} \tag{16}$$

within the elliptical region, while it was zero in the remaining domain. Finally, the bed elevation was defined as:

$$h(x', y') = min[\,0.45,\; max[\,0.10,\; 0.45 - 0.02 \cdot (5.82 + x')\,]\,] - d'(x', y').$$

Figure 2 displays the depth profile along a section at $y = 0\,m$.

A wavemaker was installed at $x = -15\ m$, while on the opposite side (i.e. in the shallow water region) a gravel beach was realized to dissipate the wave energy by a breaking process. In the experiment, regular waves with period 1.0 $s$ and wave height 0.0464 $m$ were generated

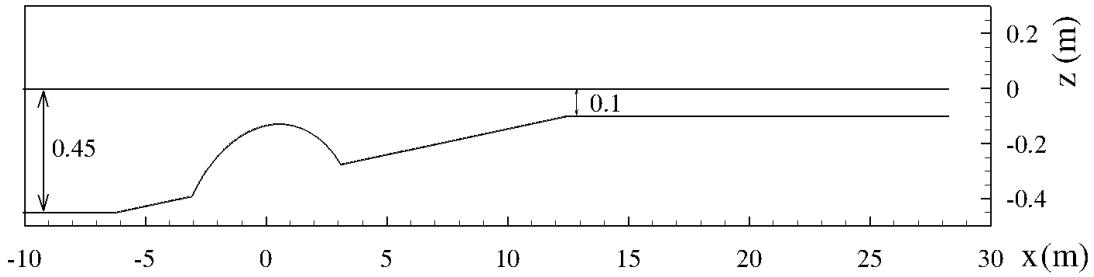


FIG. 2. Spatial depth profile for the elliptical shoal experiment (section at $y = 0\ m$).

and initially propagated over a reference depth of $0.45m$. This corresponds to a wavelength $L = 1.485\ m$, $\mu = 1.904$ (intermediate depth) and $\epsilon = 0.103$ (weakly-nonlinear waves).

During the experiment, eight measurement section cuts were used to record the wave elevation: five transversal transects above and behind the shoal $(1-5)$ and three longitudinal transect $(6-8)$. The positions of the section cuts are listed in Table I. The experimental data are available as wave height coefficients, which represent the maximum wave heights at a certain point, averaged over several wave periods and normalized with the input wave height. A schematic view of the gage transect locations is given in Figure 3 along with a snapshot of the evolution predicted by the numerical solver which highlights the refraction and shoaling processes and the focusing of the wave pattern past the submerged shoal.

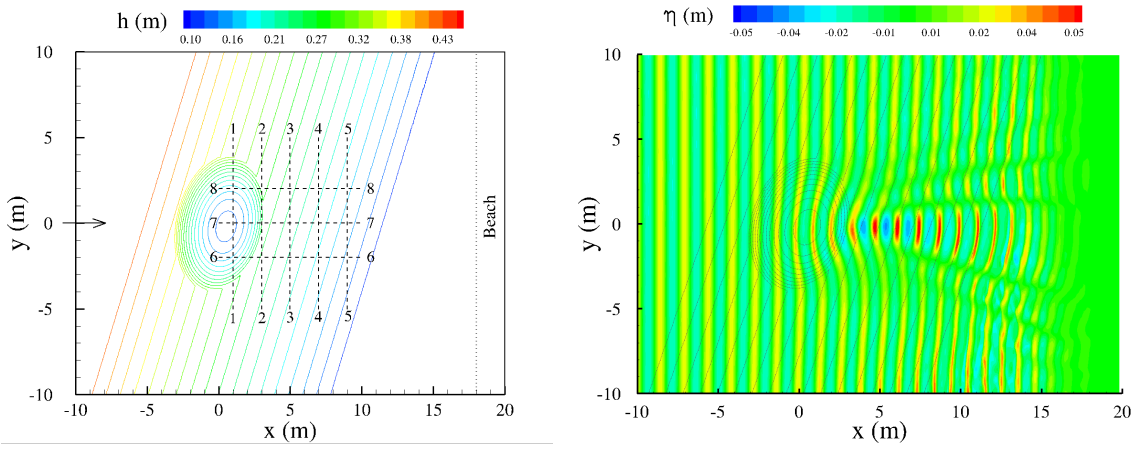


FIG. 3. Left: contour lines of the bathymetry and schematic view of the gage transect locations. Right: a snapshot of the evolution as predicted by the numerical scheme.

The numerical simulation is performed by discretizing the fluid domain through a Cartesian grid with uniform spacing in each direction. Specifically, we choose $\Delta x = 0.025\, m$,

| Section cut | Orientation | Coordinate |
|---|---|---|
| 1-1 | Transverse | x = 1.0 m |
| 2-2 | Transverse | x = 3.0 m |
| 3-3 | Transverse | x = 5.0 m |
| 4-4 | Transverse | x = 7.0 m |
| 5-5 | Transverse | x = 9.0 m |
| 6-6 | Longitudinal | y = -2.0 m |
| 7-7 | Longitudinal | y = 0.0 m |
| 8-8 | Longitudinal | y = 2.0 m |

TABLE I. Locations of the eight section cuts.

$\Delta y = 0.1\,m$, $\Delta z = 0.05\,m$, corresponding to $L/\Delta x = 60$ and $h_0/\Delta z = 9$. For the present test case, it is a common practice to use a larger spatial step in the $y$-direction (see, for example, Zijlema and Stelling[9], Ma et al.[10], Lu and Xie[11]), since the dynamics in the transversal direction is slightly weaker than that in the $x$-direction. Incidentally, we highlight that the adopted vertical discretization is very coarse in comparison to the wave height. In this case, the ability of describing wave propagation is essentially due to the use of depth-averaged quantities along with a basic description of the vertical dynamics. This is typical of non-hydrostatic models in general (see, for example, Yamazaki et al.[8], Zijlema and Stelling[9], Ma et al.[10], Lu and Xie[11], Meftah et al.[19]). Finally, a stretched mesh (namely, an acoustic beach) in the $x$-direction has been used for $x \geq 18m$ to simulate the gravel beach in the physical experiment. The model is run to simulate $40\,s$ of physical evolution, but only the last $6\,s$ have been saved, after a steady wave field is achieved. The wave height is calculated as the mean of $H = \eta_{max} - \eta_{min}$ over five wave periods, where $\eta_{max}$ and $\eta_{min}$ are the maximum and minimum water surface elevations, respectively.

The total number of computational nodes for this problem ranges from 1,380,000 to 1,562,000 (the number changes according to the free surface configuration) and the simulation has been run on a six-core Intel Xeon(R), CPU X5650, 2.67 GHz. The total computational time for $40\,s$ of physical evolution is about 16 days with 8906 iterations that corresponds to about $156\,s$ per iteration. The numerical solution of the three dimensional Poisson equation represents the most onerous part of the computational effort and has been obtained by using the MUltifrontal Massively Parallel Solver (MUMPS) described in Amestoy and Duff[20], Amestoy et al.[21] with 6 cores. Conversely, the depth-averaged subset has not been parallelized because of its small computational cost.

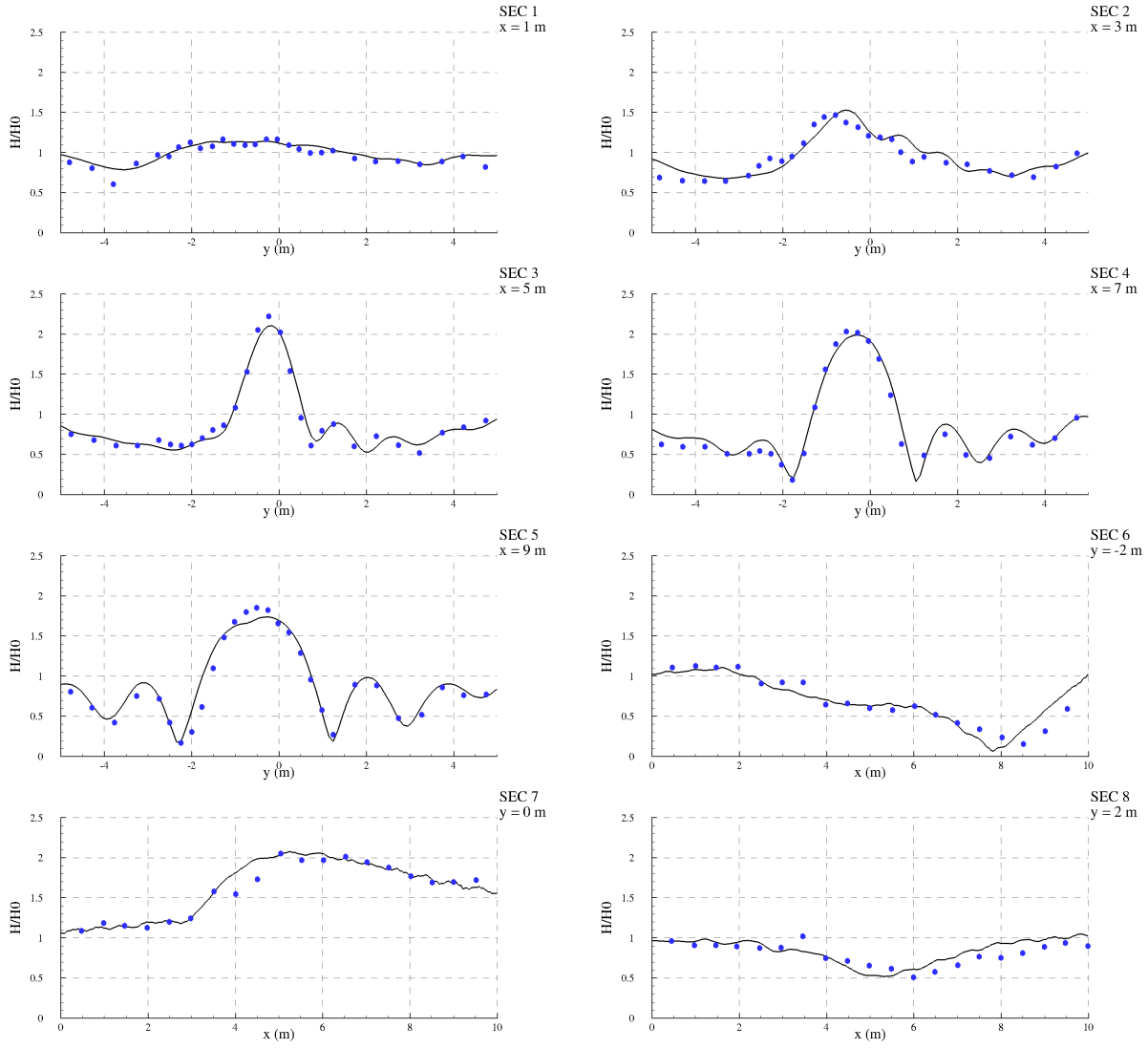


FIG. 4. Water surface profiles of the eight sections in Table I. The black solid lines and the blue dots show the numerical prediction and the experimental data, respectively.

Figure 4 shows the comparisons between the experimental measures and the computed wave height at the eight measurement sections. Generally, the numerical prediction well matches the observed data. In the first section (namely, 1–1) the wave field is not significantly affected by the presence of the shoal, and just a slight increase in wave height is observed about $y = 0\ m$. For what concerns the $2-2$, $3-3$, $4-4$ and $5-5$ sections, the numerical code correctly simulates both the maximum peaks (apart from a slight underestimation at sections $3-3$ and $5-5$) and the transverse variations of the wave field resulting from the combined effect of refraction/shoaling triggered by the co-existence of the elliptical shoal and

of sloped beach. Since the sloped beach is not parallel to the $y$-axis but rotated 20° clockwise from the latter, the distributions of the wave height in $y$ direction is not symmetric. This distinctive asymmetry is also accurately modelled by the present non-hydrostatic model. The longitudinal sections $6-6$ and $8-8$ (which are just aside to the maximum peak of the elliptical shoal, see Figure 3) quite well capture the general trend of the wave field, namely a slight steepening close to the shoal, and a pronounced decrease of the wave height past it. Finally, along the longitudinal transect $7-7$ (placed at $y = 0\,m$), the model predicts well the wave shoaling, the focusing and the gradual decrease of the wave height after the shoal. Due to refraction, wave focusing occurs behind the shoal and the maximum relative wave height, located around $x = 5\,m$ and $y = 0\,m$, is about 2.11, that is close to the experimental data.

### B. Wave run-up on a conical island

The interaction of solitary waves climbing up a conical island is studied here. In particular, we consider the laboratory physical data presented in Briggs et al.[22] as a benchmark for the validation of the proposed 3D model. The experiments were performed in both flume and basin facilities at CERC. The basin was $25\,m$ wide and $30\,m$ long. The truncated cone island was located in the center of basin (i.e. $x = 13\,m$, $y = 15\,m$). The diameters of the island at the toe, still water line and top were respectively $7.2\,m$, $4.64\,m$ and $2.2\,m$. The conical island with a slope 1:4, which corresponds to a vertical height of about $0.62\,m$, was placed on a flat bottom in the basin. The water depth of the basin was $0.32\,m$. The wavemaker was installed along the $y$-axis and was used to generate solitary waves, while the $x$-axis was perpendicular to it. The origin of the global coordinate system was located at the end of the wavemaker. An additional polar coordinate system was defined with the origin at the center of the island. The 0° direction corresponded to the positive $x$-axis and the angles were measured in counterclockwise direction. Moreover all sides of the basin were upholstered with wave absorber to minimize the wave impacts. To measure surface wave elevations, 27 capacitance wave gages were installed. The first four gages, parallel to the wavemaker, were used to measure incident wave conditions. These were located in front of the island at a distance from the toe corresponding to half wave length of the generated wave, in order to record the tsunami waves at the same stage of evolution. A

circular measurements grid of six concentric circles covered the island up to a distance $2.5\,m$ outside the toe. Measurement points were placed at the intersection of the circles with the 90° radial lines. The shallowest gages were located in $0.08\,m$ water depth and the deepest gages over the toe. The remaining 8 gages were equally spaced between these points along the 90° radial lines. Two additional gages were spaced in the deep water part at distances of $1.0\,m$ and $2.5\,m$ from the toe, except for the 0° and 270° transects. Furthermore digital run-up gauge were used to record run-up time histories. A sketch of the island geometry is shown in Figure 5.

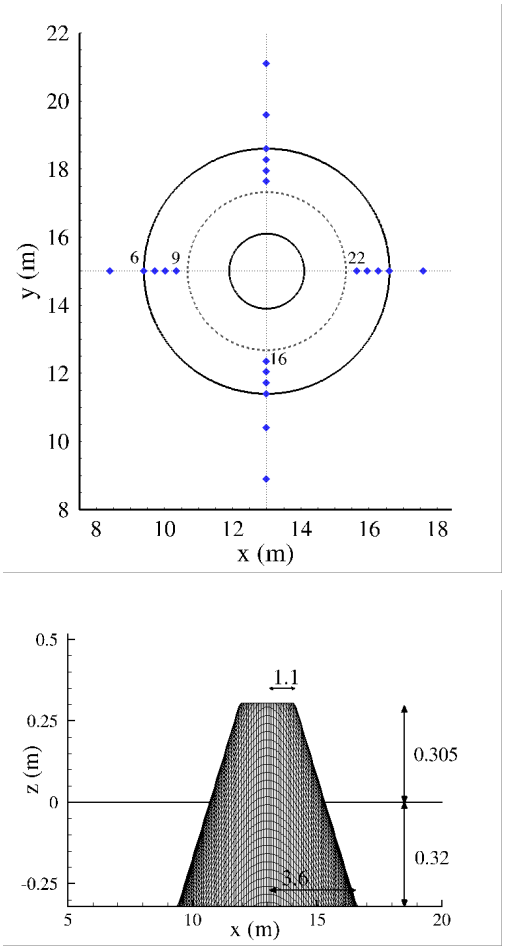


| Gauge ID | x (m) | y (m) | z (cm) | Position |
|---|---|---|---|---|
| 1 | f(L/2) | 18.75 | 32.0 | Incident Gage |
| 2 | f(L/2) | 16.25 | 32.0 | Incident Gage |
| 3 | f(L/2) | 13.75 | 32.0 | Incident Gage |
| 4 | f(L/2) | 11.25 | 32.0 | Incident Gage |
| 5 | 8.4 | 15.0 | 32.0 | 270° transect |
| 6 | 9.4 | 15.0 | 32.0 | 270° transect |
| 7 | 9.72 | 15.0 | 24.0 | 270° transect |
| 8 | 10.04 | 15.0 | 16.0 | 270° transect |
| 9 | 10.36 | 15.0 | 8.0 | 270° transect |
| 10 | 13.0 | 21.1 | 32.0 | 180° transect |
| 11 | 13.0 | 19.6 | 32.0 | 180° transect |
| 12 | 13.0 | 18.6 | 32.0 | 180° transect |
| 13 | 13.0 | 18.28 | 24.0 | 180° transect |
| 14 | 13.0 | 17.96 | 16.0 | 180° transect |
| 15 | 13.0 | 17.64 | 8.0 | 180° transect |
| 16 | 13.0 | 12.36 | 8.0 | 0° transect |
| 17 | 13.0 | 12.04 | 16.0 | 0° transect |
| 18 | 13.0 | 11.72 | 24.0 | 0° transect |
| 19 | 13.0 | 11.4 | 32.0 | 0° transect |
| 20 | 13.0 | 10.4 | 32.0 | 0° transect |
| 21 | 13.0 | 8.9 | 32.0 | 0° transect |
| 22 | 15.64 | 15.0 | 8.0 | 90° transect |
| 23 | 15.96 | 15.0 | 16.0 | 90° transect |
| 24 | 16.28 | 15.0 | 24.0 | 90° transect |
| 25 | 16.6 | 15.0 | 32.0 | 90° transect |
| 26 | 17.6 | 15.0 | 32.0 | 90° transect |
| 27 | 19.1 | 15.0 | 32.0 | 90° transect |

FIG. 5. Top left panel: top view of the island; the blue diamonds indicate the probes listed in the Table on the right. Bottom left panel: vertical view of the circular island on the cross-section $y = 15\,m$.

Tsunami waves were modelled by using the solitary wave solution predicted by the Korteweg-de Vries equation (see, for example, Dean and Dalrymple[23]). The surface profile

$\eta(x,t)$ for a wave centred at $x = X_1$ and time $t = 0$ is defined as:

$$\eta(x,0) \;=\; H\,\mathrm{sech}^2[\,\gamma\,(x - X_1)\,] \qquad \gamma = \sqrt{\frac{3\,H}{h_0}}\,. \tag{17}$$

In the experiments three different target initial solitary wave profiles were used with $\epsilon = H/h_0 = 0.05, 0.1$ and $0.2$. The reference length (which was used in the experiments to place the gauge 3) is given by the following formula:

$$L \;=\; \frac{2h_0}{\gamma}\,\mathrm{arcsinh}(\sqrt{20}) \tag{18}$$

and indicates the distance between the two end points in the symmetric profile where the height is 5 percent of the height at the crest.

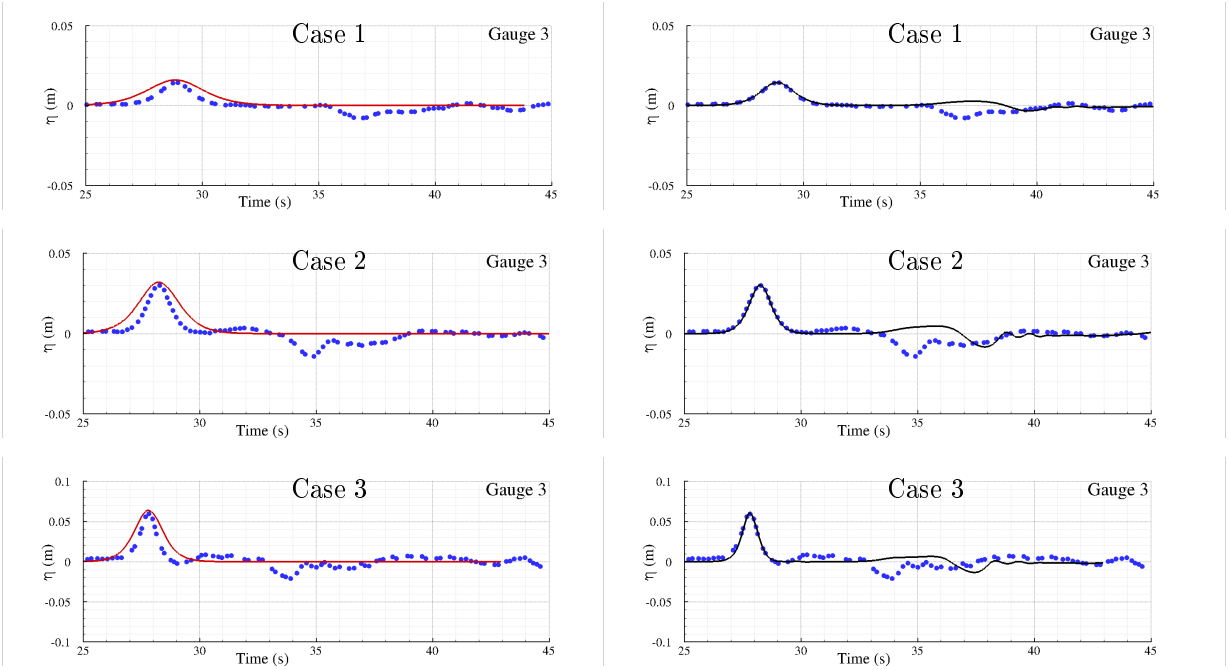


FIG. 6. Solitary wave on a conical island (see Table II for details on the test cases). Left: comparison between the measured free-surface elevation at gauge 3 (dots) and the analytical solution in equation (17) (solid lines). Right: comparison between the measured free-surface elevation at gauge 3 (dots) and the numerical solution after the calibration (solid lines).

In the numerical simulations the domain is discretized with a Cartesian grid with $\Delta x = \Delta y = 0.1\,m$ and $\Delta z = 0.08\,m$. Wall conditions are assigned along the lateral boundaries with exception of the boundary at $x = 0\,m$ where inflow conditions are set by using the analytical solution in (17). An initial comparison for the three cases $\epsilon = 0.05, 0.1$

and 0.2 (see left panel of Figure 6) shows that the experimental signals at gauge 3 (the closest to the wave maker) differ from the analytical solution in both the wave width and the crest height. For this reason, a calibration of both the parameters $\epsilon$ and $\gamma$ in equation (17) has been carried out to find the best fitting between the experiments and the numerical input datum. The calibrated parameters are reported in Table II. Note that, differently from the analytical solution in equation (17), the parameter $\gamma$ is treated as a free parameter (i.e., it has been chosen independently of $\epsilon$).

| *Test cases* | $\epsilon_i$ | $\epsilon_f$ | $H_i$ (m) | $H_f$ (m) | $\gamma_i$ | $\gamma_f$ |
|---|---|---|---|---|---|---|
| 1 | 0.05 | 0.045 | 0.016 | 0.0144 | 0.194 | 1.0 |
| 2 | 0.1 | 0.09375 | 0.032 | 0.03 | 0.274 | 1.45 |
| 3 | 0.2 | 0.1875 | 0.064 | 0.06 | 0.387 | 2.0 |

TABLE II. Target solitary wave parameters pre and post calibration: the subscript $i$ indicates the nominal value of the experiment while the subscript $f$ denotes the value obtained after the calibration.

The right panel of Figure 6 shows the comparison between the experimental signals at gauge 3 and the numerical solutions after calibration. The leading wave is well described both in terms of maximum height and width while the numerical outputs show a slight delay in the subsequent depression wave caused by the reflection of the solitary wave during the run-up on the island. This phenomenon is likely due to a difference in the gauge location in comparison to the physical experiments. Indeed, we recall that in Briggs et al.[22] the position of the gauge 3 was set by using the reference length of the tsunami wave, but this was not explicitly reported. Further, the calibration process make the assessment of the location of the gauge 3 rather ambiguous. To support this hypothesis, we anticipate that the above delay does not appear in the signals recorded in the remaining gauges. We also observe that the experimental measurements are affected by a spurious noise following the leading solitary-wave signal. In Briggs et al.[22] no mention is done about this phenomenon which may be caused to the data acquisition system as well as to the wave-maker motion. Due to its spurious nature, this cannot be reproduced in the numerical solution.

For the case with the steepest wave input, the total number of computational nodes ranges between $505,000$ and $542,000$ and the simulations has been run by using two cores.

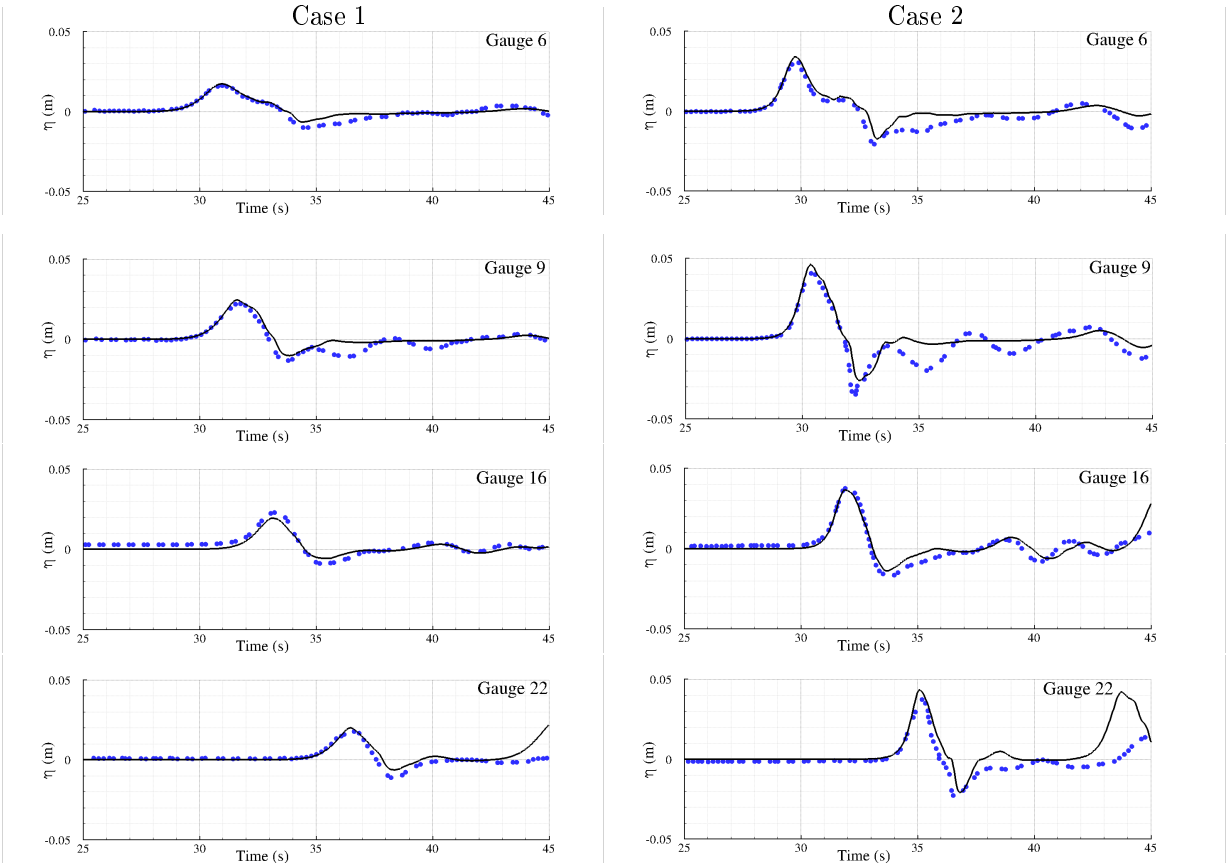


FIG. 7. Comparison for the free-surface time series of the case 1 (left column) and 2 (right column). See Table II for details on the test cases. Black solid lines: numerical solution. Blue dots: experiments.

The total computational time for 20 $s$ of physical evolution is about 0.65 days with 1129 iterations that corresponds to about 50 $s$ per iteration. The computational costs for the remaining cases are similar to those mentioned above.

The left and right columns of Figure 7 displays the comparisons at the gauges 6, 9, 16 and 22 for the case 1 and 2 respectively (see Table II). In all the cases the leading waves are well described by the numerical solver while a small underestimation of the subsequent depression waves is observed. The numerical solutions also appear smoother in comparison to the experiments which show some oscillations after the leading and depression waves. This phenomenon may be a consequence of the initial noise in the inflow signals (see Figure 6) even though, at present, we have not enough details to draw definite conclusions. On the lee side of the island the reflection of the solitary waves at the boundary (wall) of the domain is also evident (see the gauge 22 in the bottom panels of the same figure). However,

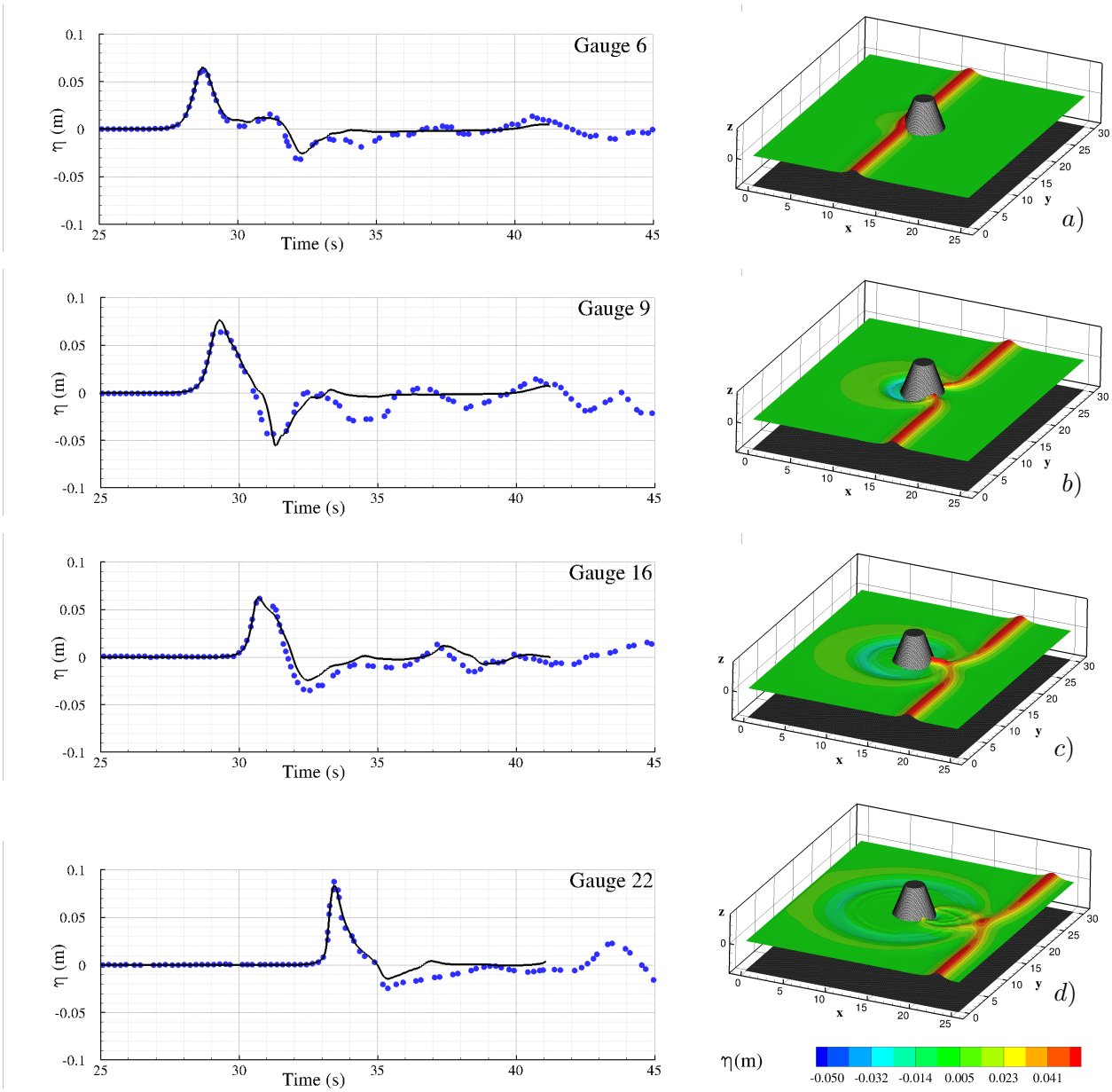


FIG. 8. Left: comparison for the free-surface time series of the case 3: black solid lines indicates the numerical solutions and the dots the experiments. Right: some snapshots of the evolution as predicted by the numerical scheme.

these reflected waves do not affect the maximum run-up heights observed in the laboratory.

The case 3 is discussed apart from the previous experiments, since a stronger dynamics occurs and, as reported in Briggs et al.[22], an incipient wave-breaking event was observed during the experiments. Despite the numerical scheme does not implement any model for breaking waves, the agreement with the experimental measurements is still good (see the

left column of figure 8). In right column of the same figure some snapshots of the solitary wave evolution for the case 3 are displayed. After the initial run-up on the island (panel $a$ of the right column), the wave front undergoes a strong deformation as a consequence of the compound action of refraction and diffraction. This phenomenon leads to the generation of a pair of edge waves (panel $b$) that travel alongshore the island and, finally, superimpose at the lee side generating a secondary run-up (panel $c$). Then, a run-down and a further pair of smaller edge waves develops, travelling back toward the front side of the island (panel $d$). Incidentally, we highlight that the same dynamics (even if weaker) occurs for the cases 1 and 2.

As a final validation, the maximum horizontal run-up around the island is compared to the measured one (see the left column of Figure 9). The waterline and the island toe are shown for reference. In the numerical scheme the shoreline has been detected by using a linear reconstruction algorithm between dry and wet cells (see appendix B for detail) . For the test case 1 (top left panel) the run-up is fairly uniform around the perimeter of the island and is lightly higher on the front side. The numerical data slightly overestimates the experimental run-up on the back side because of difficulties in modelling the interface between the dry cells and wet cells, especially for small wave heights. For the case test 2 (middle left panel), the run-up on the back side is slightly larger than that on the front side. Refraction and diffraction cause the wave to bend around the island as edge waves. Because the island is symmetric, the wave wraps evenly around the island and produces relatively large run-up on the back side. In any case, a good agreement between numerical and measured data is observed, apart for a small overestimation of the maximum run-up at $\pm\pi/8$. This may be due to the difficulty of the shoreline-tracking algorithm in accurately describing the dynamics on the back side, since this is strong and very localized in both time and space. Finally, for the case test 3 (bottom left panel), the run-up on the front side is larger than on the back side of the island. Here, a distinctive pattern of run-up due to edge waves propagating around the island is evident. Some minor differences are shown between the numerical result and the laboratory data. These maybe due to the fact that the numerical solver does not include a model for wave breaking.

To complete the analysis, the right column of Figure 9 displays the maximum run-down around the island as predicted by the *DepSeA* model (note that in this case no experimental measurements are available). In the case 1 (top right panel of Figure 9) the maximum

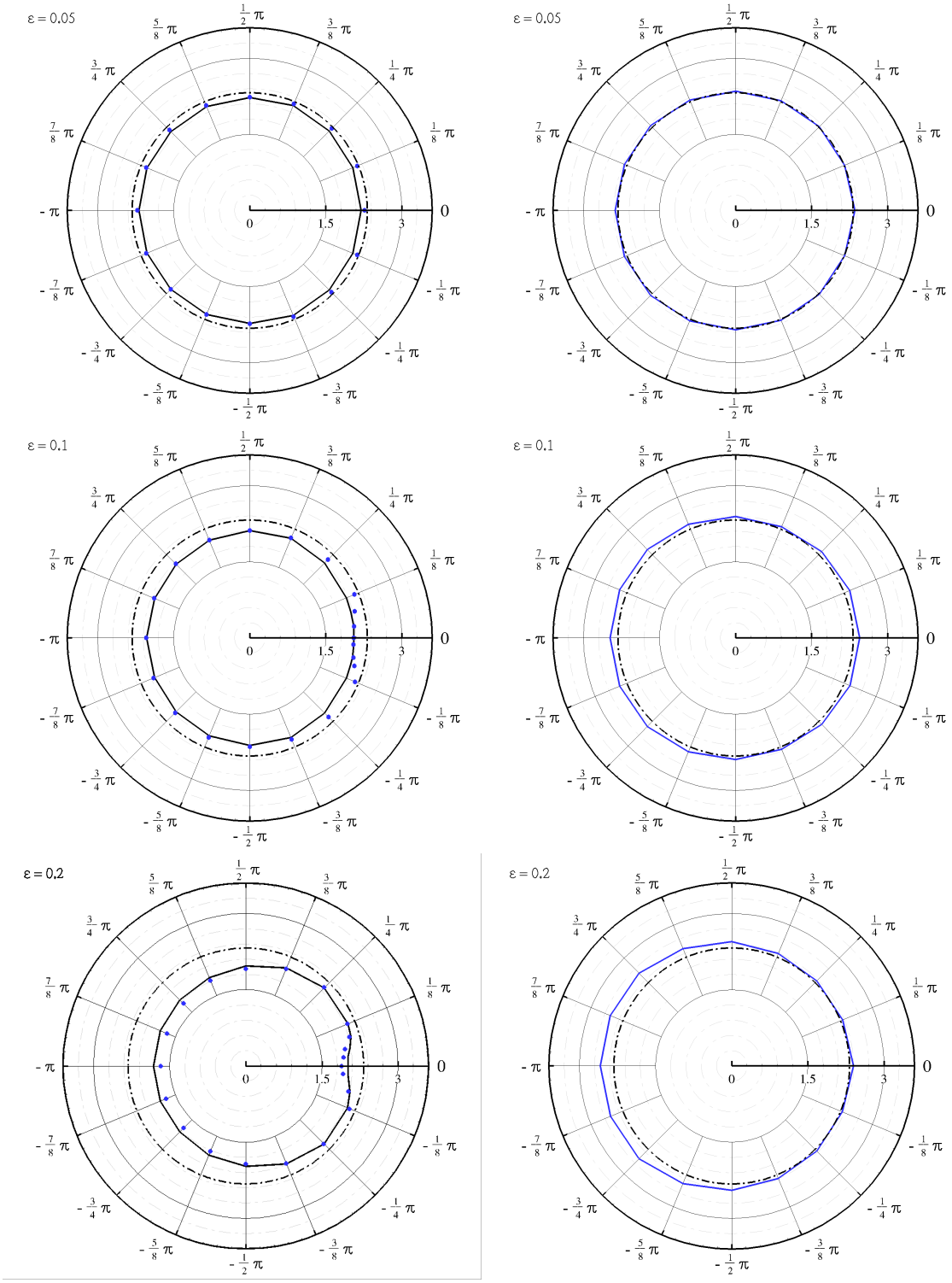


FIG. 9. Left column: comparison between the numerical (solid lines) and experimental (dots) maximum run-up for the test cases 1, 2 and 3 (from top to bottom). Right column: the maximum run-down predicted by the numerical scheme. The dash-dotted lines represent the mean sea level.

displacement is rather small while a slightly more pronounced run-down is observed for the case 2. In this latter configuration, the displacements on the front and lee side of the island are comparable. This symmetry is lost in the case 3 (bottom right panel of Figure 9) where a larger maximum run-down occurs in the front side of the obstacle. This is consistent with the stronger dynamics of the run-up on the same side of the island (bottom left panel). In all the cases, the wave focusing on the lee side seems to have a negligible effect on the maximum run-down.

### C. Run-up of a solitary wave on a Bay-Promontory pattern

This final test is carried out to show a possible application to a full-scale coastline. In particular, we study the evolution of a solitary wave propagating towards a possible coast, as realistic as possible, composed by a central bay and two side headlands. The problem is scaled with $h_0$, that is the reference depth in still-water conditions at the seaward limit of the domain, and the following scales are used:

$$\begin{array}{llll} \mathbf{x} = h_0\,\mathbf{x}^*, & z = h_0\,z^*, & \mathbf{u} = \sqrt{g\,h_0}\,\mathbf{u}^*, & w = \sqrt{g\,h_0}\,w^*, \\ t = \sqrt{h_0/g}\,t^*, & h = h_0\,h^*, & \eta = h_0\,\eta^*, & d = h_0\,d^*, \end{array} \tag{19}$$

where $\mathbf{x} = (x, y)$, $\mathbf{u} = (u, v)$ and the superscript '$*$' identifies the dimensionless variables. In fact, this corresponds to run a simulation with the gravity acceleration set equal to 1. The chosen geometry combines a constant-depth bottom ($x^* < 0$) with a beach ($x^* \geq 0$) whose slope is modulated in the along-shore direction (e.g. y-direction). Specifically, the beach is defined by:

$$h^*(x^*, y^*) = 1 - \beta\,\left[1 - A\,\cos\left(\omega_y^*\,y^*\right)\right]\,x^* \tag{20}$$

where $\beta$ is the non-modulated slope (set equal to 0.07), $A$ is the amplitude of the sinusoidal variation in $y^*$-direction (equal to 0.5) and $\omega_y^*$ is the phase of this variation. The latter is function of the cross-cutting dimension of the computational domain, according to the relation $\omega_y^* = 2\pi/L_y^*$. Clearly, the bottom varies linearly in the $(x^*, z^*)$ plane while the $(y^*, z^*)$ plane presents a sinusoidal variation which is function of the domain dimension. In practise, it is sufficient to decrease (increase) $L_y^*$ to obtain a narrower (wider) bay, maintaining the same slopes along the symmetry axis (namely $y^* = 0$) and at the extrema of the domain (namely $y^* = \pm L_y^*/2$).

The computational domain is characterized by $L_x^* = 70$ with $x^* \in [-10, 60]$ and three different bays are considered, namely $L_y^* = 30, 60, 90$ corresponding to $y^* \in [-15, 15]$, $y^* \in [-30, 30]$ and $y^* \in [-45, 45]$. The grid size is the same in all the above cases with $\Delta x^* = \Delta y^* = 0.125$ and $\Delta z^* = 0.2$. The inflow wave is a solitary wave with $\epsilon = H/h_0 = 0.2$ [see the equation (17) for details] and is generated at the seaward limit of the domain, namely $x^* = -10$. Wall conditions are imposed along the remaining boundaries. All simulations have been run up to $t^* = 150$ to simulate the whole wave evolution (run-up and run-down motions). For $L_y^* = 90$ the total number of computational points ranges between 360,000 and 424,000 while for $L_y^* = 30$ it goes from about 121,000 to 143,000. In all the cases the three dimensional problem has been solved by using 2 cores. The total computational time in the former case is about 1.5 days with 3561 iterations that corresponds to about 38 $s$ per iteration, while for $L_y^* = 30$ it is about 0.44 days with 3568 iterations that corresponds to about 10.6 $s$ per iteration.

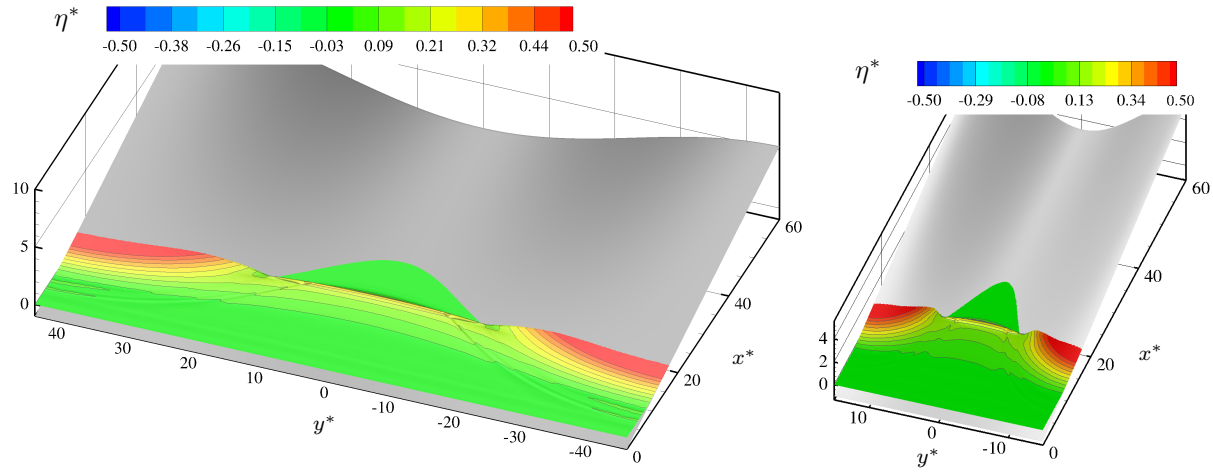


FIG. 10. Snapshots of the solitary wave run-up (contour plot of the surface elevation). Left panel: bay with $L_y^* = 90$ at $t^* = 33.05$. Right panel: bay with $L_y^* = 30$ at $t^* = 33.21$.

Incidentally, we highlight that in all the simulations the numerical model predicts the occurrence of steep wave fronts, probably resembling wave breaking events. Though no breaking model has been implemented, the conservative structure of the numerical model allows for a direct simulation of these dynamics. In this case, the dissipation induced by the breaking event is only due to the entropy condition prescribed by the HLL approximate solver (see, for example, Toro[1]) and is, therefore, underestimated in comparison to real breaking events.

In the following part we first describe the evolution of the solitary wave over the widest and narrowest bay, $L_y^* = 90$ and $L_y^* = 30$ respectively. In fact, the dynamics in the $L_y^* = 60$ lies in the middle between the above bathymetries. Figure 10 displays the early stages of the tsunami wave climbing over the bays. Both the cases show a similar behaviour, even if for the narrowest bay (right panel) a slightly more intense run-up is observed along the two lateral headlands.

In the subsequent instants, the different widths of the bays play a relevant role and lead to different dynamics. In particular, the top panels of figure 11 show that in the widest bay (panel $a$) two lenses of high elevation (red coloured) develops along the headlands and move towards the centre while in the narrowest bay (panel $b$) these split in two components, one reflected seaward and one climbing along the headlands.

This phenomenon strongly influences the subsequent dynamics. In fact, the lateral waves interact differently in the two bays. For $L_y^* = 90$ the wave fronts generated along the headlands move one against the other and focus at the bay center (panels $c$ and $e$ of figure 11). Conversely, for $L_y^* = 30$ the waves climbing along the headlands propagate obliquely to the direction of the incoming wave and, then, intersect and generate a cusped front that propagates onshore (panels $d$ and $f$ of figure 11).

We highlight that the dynamics over the widest bay is slightly slower than the case $L_y^* = 30$ and, at this stage, its maximum wave elevation is larger. This behaviour changes in the subsequent evolution. Indeed, the left column of Figure 12 (panels $a$ and $c$) clearly shows that for $L_y^* = 90$ the wave front advances very weakly in the onshore direction while it mainly broadens in the $y$-direction. On the contrary, the constructive interaction of the lateral fronts in the narrowest bay (right column) further feeds the run-up motion, generating an "arrow" profile that continues moving in the onshore direction (panels $b$ and $d$ of Figure 12). Because of this behaviour, the maximum run-up for the bay with $L_y^* = 30$ is significantly larger than that observed for $L_y^* = 90$ (see Table III). The snapshots corresponding to the maximum run-ups are displayed in the middle panels of figure 12 (namely, panels $c$ and $d$).

Finally, the run-down stages are plotted in the bottom panels of figure 12. In this case, the narrowest bay (namely, $L_y^* = 30$) shows the slowest and weakest dynamics (panel $f$). On the contrary, because of the larger amount of water entrapped in the bay, the case with $L_y^* = 90$ displays a stronger run-down motion and the generation of two strong edge waves that propagate alongshore (panel $e$).

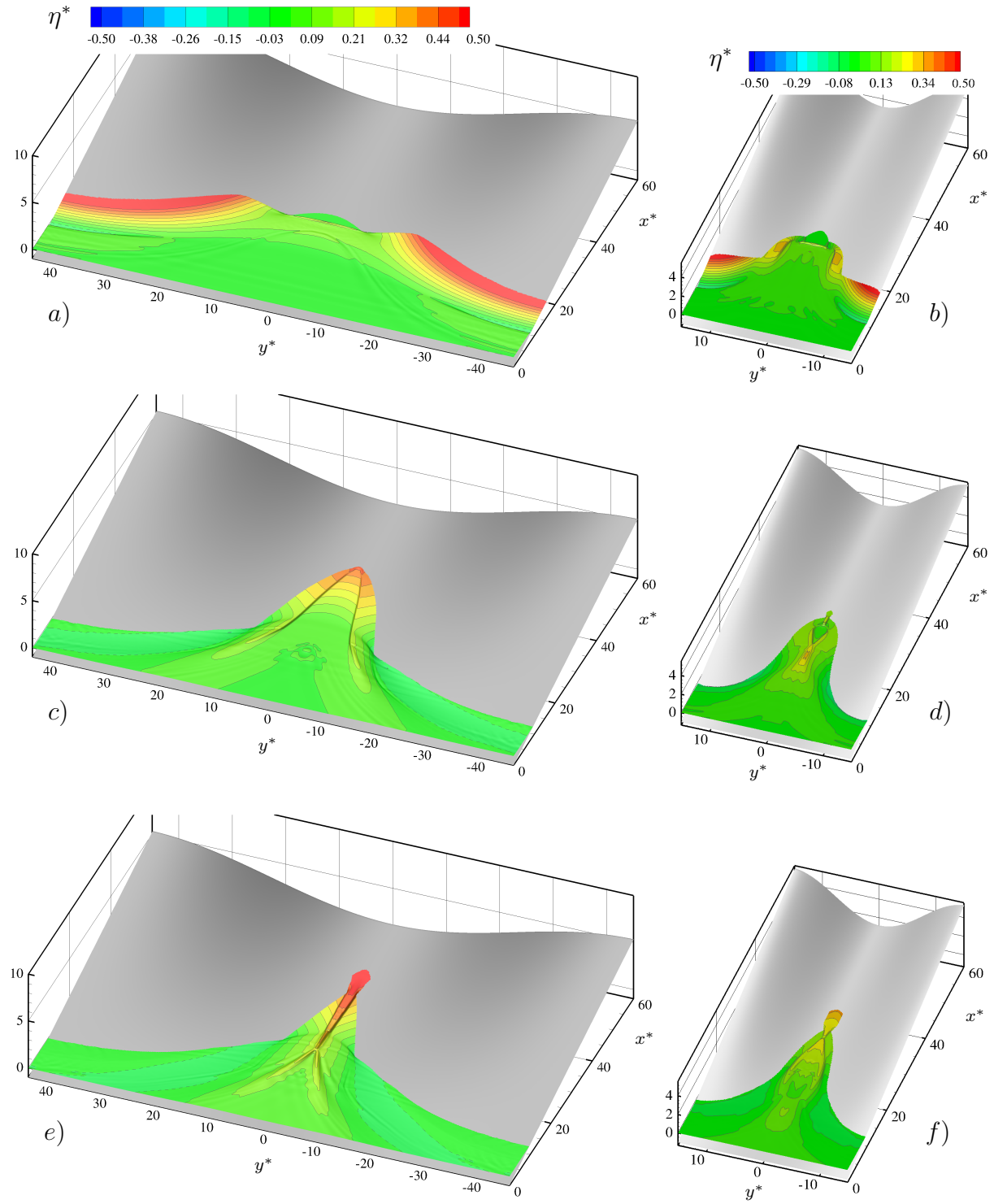


FIG. 11. Snapshots of the solitary wave run-up (contour plot of the surface elevation). Left column: bay with $L_y^* = 90$ at $t^* = 41.12, 60.63, 68.07$. Right column: bay with $L_y^* = 30$ at $t^* = 41.05, 46.66, 51.20$.

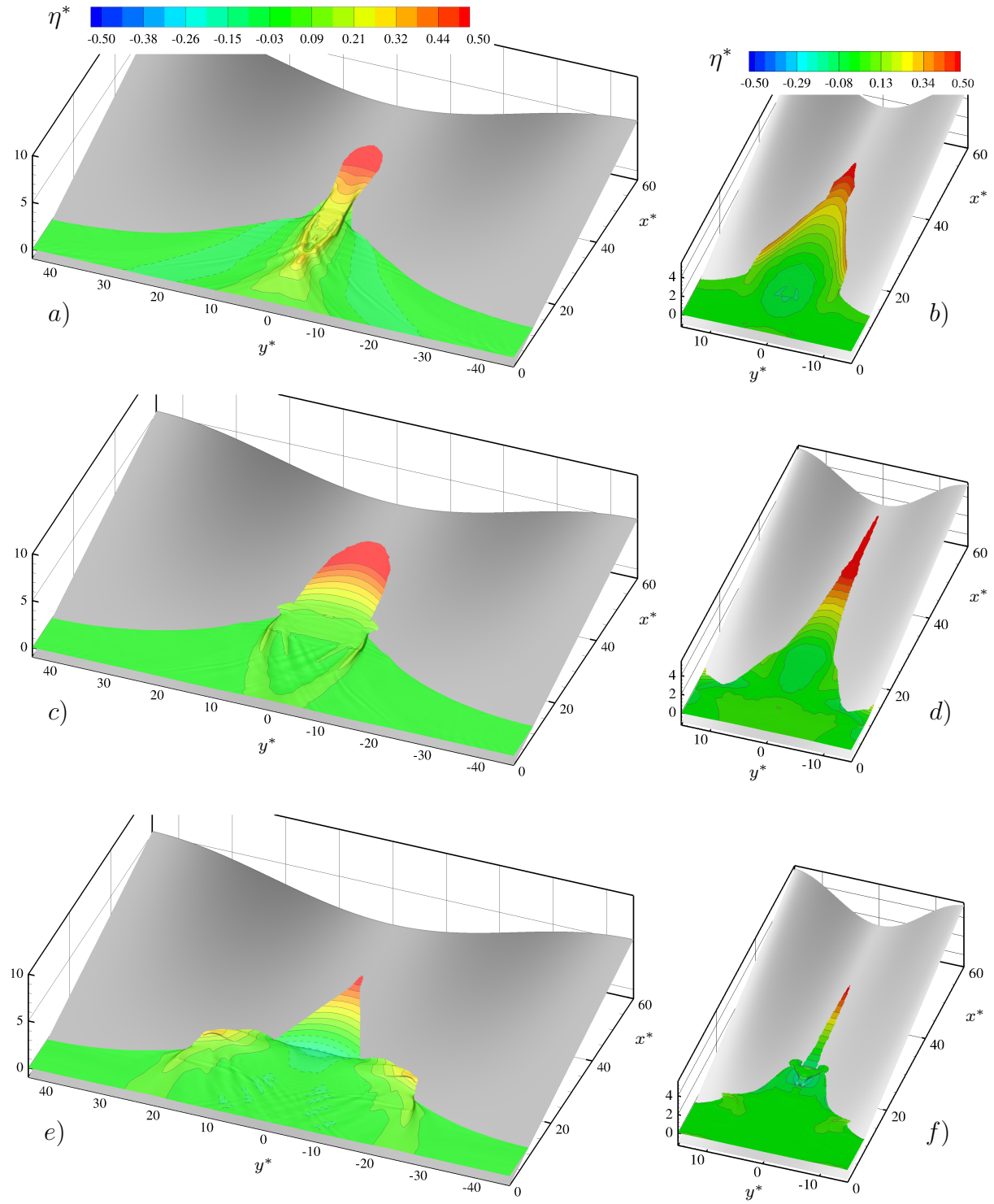


FIG. 12. Snapshots of the solitary wave run-up (contour plot of the surface elevation). Left column: bay with $L_y^* = 90$ at $t^* = 72.70, 80.79, 98.83$. Right column: bay with $L_y^* = 30$ at $t^* = 58.31, 80.13, 112.36$.

| Test cases | $L_y^* = 90$ | $L_y^* = 60$ | $L_y^* = 30$ |
|---|---|---|---|
| $\eta_{max}^*$ | 0.717 | 0.835 | 1.005 |
| $x_{max}^*$ | 49.06 | 52.43 | 57.31 |

TABLE III. Maximum wave elevation and maximum run-up for the three bays.

Finally, Table III shows the maximum run-up for the three bays (namely $L_y^* = 30, 60, 90$) along with the maximum wave elevation. In all the cases, this is attained at $y^* = 0$, i.e. along the symmetry axis of the bay. As already anticipated, the maximum run-up tends to increase as the bay width decreases, confirming the constructing interaction of the wave fronts reflected by the headlands. A bit more complex is the evolution of the depth-averaged velocity field, since violent phenomena of run-up/run-down occur in different zones of the coastline. To better highlight where the dynamics is more intense, we consider the kinetic energy associated with the depth-averaged velocity, namely $E_{kin} = (U^2 + V^2)/2$. Figure 13 displays some snapshots of the evolution of $E_{kin}$ for the bay with $L^* = 90$ (for the sake of simplicity, only the upper plane, namely $y^* \geq 0$, is depicted). The panel $a$ shows that two run-up events occur almost simultaneously close to the promontory (at about $y^* = 45$) and to the bay center (at about $y^* = 10$). In the former case the run-up dynamics is immediately followed by a strong run-down motion (panel $b$) that subsequently evolves alongshore towards the bay center (see the panels $b$ and $c$). On the contrary, the second run-up event continues its evolution and slowly moves towards the bay center (panels $b$ and $c$). In this latter case the dynamics is weaker than that characterizing the run-down motion close to the promontory (panel $b$) and this suggests that an intense beach erosion may occur along the headlands.

Rather different is the dynamics in the narrowest bay, that is for $L^* = 30$. In this case, the run-up/run-down motion close to the promontory still occurs but the kinetic energy attains smaller values (see the figure 14). Moreover, differently from the case with $L^* = 90$, this phenomenon does not distinctly generate a wave system moving toward the bay center since, as described in the panel $b$ of figure 11, waves are reflected away from the beach. Apart from this, an intense dynamics is observed in the central part of the bay where the kinetic energy attains values which are of the order of unity. This explains the occurrence of a larger maximum run-up in comparison with the widest bay and confirms that in the narrowest bay a stronger dynamics occurs in the central part.

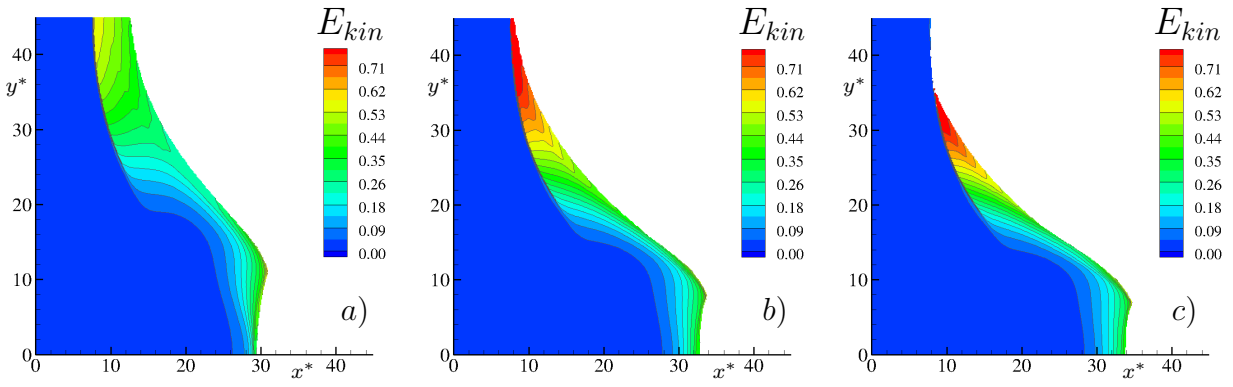


FIG. 13. Contour plot of the kinetic energy for the bay with $L_y^* = 90$ at different time instants, namely $t^* = 45.49$ (panel $a$), $t^* = 49.08$ (panel $b$) and $t^* = 50.36$ (panel $c$).

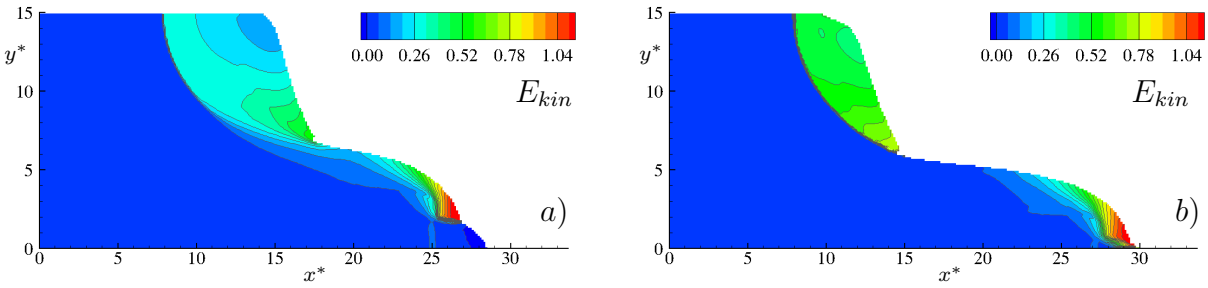


FIG. 14. Contour plot of the kinetic energy for the bay with $L_y^* = 30$ at different time instants, namely $t^* = 41.05$ (panel $a$) and $t^* = 44.00$ (panel $b$).

## IV. CONCLUSIONS

In the present work we extend the *DepSeA* scheme described in Antuono et al.[14] to deal with three-dimensional problems. In the first part of the work we test the proposed scheme against reference benchmarks available in the literature. In particular, we consider the transformation of a regular wave train propagating over a submerged elliptical shoal placed over an inclined planar beach. As a second test, the run-up of a solitary wave on a conical island is simulated. In both the cases the comparisons with the experimental measurements are good, proving the accuracy and the robustness of the proposed numerical scheme and suggest that this is a reliable tool for the modelling of the wave motion in the nearshore region.

As a final example, we describe the run-up of a solitary wave over a bay-promontory pattern and study the influence of the bay width on the wave dynamics and on the maximum run-up. These simulations highlight rather different motions for the widest and narrowest

bays. In the former case, the beach inundation is smaller and the most intense dynamics is observed close to the promontory with the generations of a strong run-down event. Conversely, in the narrowest bay the maximum run-up is larger and the motion is more intense in the central part of the bathymetry.

**Acknowledgements**

The authors thank Prof. Paolo De Girolamo, Dr. Alessandro Romano and Prof. Maurizio Brocchini for the useful comments and discussions. This work was partially supported by the Research Council of Norway through the Centres of Excellence funding scheme NTNU/AMOS, project number 223254.

**Appendix A: Shallow water conditions**

In the water regions where the depth is very shallow and the vertical discretization is not fine enough, the three-dimensional problem is not solved but an approximate analytical solution for $\Upsilon$ is assigned. The first step to derive such a solution is to find an estimate for the vertical velocity along the bottom. The simplest approach is to assume that bottom is a mild-slope beach. Under this hypothesis, we can write:

$$w|_{z=-h} \,=\, -\,\Upsilon_z \,\simeq\, \frac{\partial \Upsilon}{\partial n}\Big|_{z=-h} \,=\, -\,\left[\, h_t \,+\, \frac{\boldsymbol{M}}{d}\cdot\nabla h \right] \Big/ \sqrt{1+\|\nabla h\|^2}\,.$$

In shallow water condition, we can as well assume that the variation along the vertical direction are negligible in comparison to the horizontal motion. As a consequence, we write:

$$\Upsilon \,\simeq\, \int_z^{\eta} w\,\mathrm{d}z \,=\, (\eta - z)\, w|_{z=-h}\,, \tag{A1}$$

which is the desired relation. The above approximation is used where the vertical discretization is less than two points over the depth. In particular, it is adopted to estimate the deviation $(\boldsymbol{M}-\boldsymbol{Q})$ and the remaining nonlinear diffusive terms. In the latter case, the velocity deviations $\delta\boldsymbol{u}$ are assumed to be negligible and $\boldsymbol{u}\simeq\boldsymbol{U}$ is imposed. Finally, the above approximation is used as Dirichlet condition for the three-dimensional Poisson equation along the boundary with the shallow water region.

## Appendix B: Wet-dry interface

Since the *DepSeA* model is expressed by means of conservative variables (namely, $\boldsymbol{Q}$ and $d$), the depth-averaged velocity field $\boldsymbol{U}$ is computed though the ratio $\boldsymbol{Q}/d$. Numerically, it is infeasible to define the wet-dry interface as the border of the fluid domain where $d = 0$, because the above ratio would be meaningless. Further, even when the depth is positive but very shallow, such a ratio may be numerically ill-conditioned and may lead to the occurrence of large spurious oscillations in the $\boldsymbol{U}$ field (see, for example, Toro[1]). For these reasons, it is convenient to identify the wet-dry interface through the use of a proper threshold depth: if the water depth predicted by the model is smaller than such a threshold value, the cell is set to dry conditions (i.e. $\eta = -h$, $\boldsymbol{U} = \boldsymbol{M} = 0$ and $\Upsilon = 0$). The threshold depth has to be large enough to avoid the occurrence of spurious oscillations in the $\boldsymbol{U}$ field and, at the same time, has to be small enough to have a negligible influence on the dynamics of the wet-dry interface. Generally, such a threshold depth has to depend on both the local spatial resolution and bottom bathymetry. In particular, denoting by $\Delta x^{(i)}$ and $\Delta y^{(i)}$ the side lengths of the $i$-th cell and by $h_x^{(i)}$ and $h_y^{(i)}$ the local $x$- and $y$-derivatives of the bottom, we choose:

$$d_\epsilon^{(i)} \;=\; \max\left( d_s^{(i)}, d_h^{(i)} \right) \tag{B1}$$

where

$$d_s^{(i)} \;=\; 7.5 \cdot 10^{-4} \sqrt{\left(\Delta x^{(i)}\right)^2 + \left(\Delta y^{(i)}\right)^2}$$

$$d_h^{(i)} \;=\; 0.05 \sqrt{\left(h_x^{(i)} \Delta x^{(i)}\right)^2 + \left(h_y^{(i)} \Delta y^{(i)}\right)^2} \,.$$

Note that $d_h$ takes into account the local variation of the bottom and, therefore, is zero for a planar bathymetry. The numerical values in the definition of $d_s$ and $d_h$ (respectively, $7.5 \cdot 10^{-4}$ and $0.05$) have been chosen by tuning through several simulations of run-up/run-down motions over planar beaches with different slopes. These values guarantee that $d_\epsilon$ is small enough to have a negligible influence on the maximum run-up/run-down and, at the same time, large enough to ensure smooth solutions for the depth-averaged velocity field $\boldsymbol{U}$ at the shoreline.

### 1. Well-balancedness

As a consequence the use of $d_\epsilon$, a jump occurs in the surface elevation across the wet/dry interface. To guarantee the well-balanced property of the scheme, it is therefore necessary to appropriately reconstruct the values of $\boldsymbol{U}$ and $\eta$ along the dry side of the interface. While it is sufficient to impose that the fluid velocity is zero, a more complex algorithm is needed for the reconstruction of $\eta$. The basic idea is to define a value of the water depth *on the dry side* of the cell that satisfies the hydrostatic solution when the variation of the surface elevation across the interface is smaller than $d_\epsilon$.

More in depth, let us assume that the wet/dry interface is placed between the $i$-th (wet) and ($i$+1)-th cell (dry) and it is indexed through ($i$+1/2). On the wet side (here indicated by the superscript 'L'), the reconstructed depth, namely $d^L_{i+1/2}$, is obtained through the method described in Yamamoto and Daiguji[24]. Conversely, on the dry side (here denoted by 'R') we impose:

$$d^R_{1+1/2} \;=\; \min\left( d^L_{i+1/2}\,, \delta^R_{i+1/2} \right)$$

where $\delta^R_{1+1/2}$ is a proper depth value that allows the fulfilment of the hydrostatic condition when

$$|\,\eta_{i+1} - \eta_i\,| \;\leq\; d_\epsilon^{(i+1)}\,, \tag{B2}$$

that is, when the jump of the surface elevation across the interface is smaller than $d_\epsilon$. Imposing the equality in equation (B2) under still water conditions, we obtain the following definition for $\delta^R_{i+1/2}$:

$$\delta^R_{i+1/2} = \max\left( \eta_{i+1} + h_{i+1/2} + d_\epsilon^{(i+1)}\,, 0 \right)\,.$$

where $h_{i+1/2}$ is the bottom level at the cell side. We recall that, in the proposed numerical scheme, we adopt the data reconstruction algorithm described in Zhou et al.[25] where $h$ is defined on a staggered grid with respect to the cell centres. As explained in Antuono et al.[14], the reconstruction is applied on primitive variables (namely, $\boldsymbol{U}$ and $\eta$) instead of conservative variables (i.e. $\boldsymbol{Q}$ and $d$), since such a procedure proves to be more robust and reliable in very shallow depths. Then, the reconstructed values for $\boldsymbol{Q}$ and $d$ are computed by using the reconstructed values for $\boldsymbol{U}$ and $\eta$ and the usual formulas, namely $d = \eta + h$ and $\boldsymbol{Q} = \boldsymbol{U}d$.

## REFERENCES


[1]E. F. Toro, *Shock-Capturing Methods for Free-Surface Shallow Flows.* Wiley and Sons Ltd., 2001.

[2]M. Antuono and M. Brocchini, "The Boundary Value Problem for the Nonlinear Shallow Water Equations," *Studies in Applied Mathematics*, vol. 119, no. 1, pp. 73–93, 2007. [Online]. Available: https://onlinelibrary.wiley.com/doi/abs/10.1111/j.1365-2966.2007.00378.x

[3]——, "Solving the nonlinear shallow-water equations in physical space," *Journal of Fluid Mechanics*, vol. 643, pp. 207–232, 2010.

[4]M. Bjørnestad and H. Kalisch, "Shallow water dynamics on linear shear flows and plane beaches," *Physics of Fluids*, vol. 29, no. 7, p. 073602, 2017. [Online]. Available: https://doi.org/10.1063/1.4994593

[5]M. Brocchini, "A reasoned overview on Boussinesq-type models: the interplay between physics, mathematics and numerics," *Proceedings of the Royal Society of London A: Mathematical, Physical and Engineering Sciences*, vol. 469, no. 2160, 2013. [Online]. Available: http://rspa.royalsocietypublishing.org/content/469/2160/20130496

[6]J. T. Kirby, "Boussinesq Models and Their Application to Coastal Processes across a Wide Range of Scales," *Journal of Waterway, Port, Coastal, and Ocean Engineering*, vol. 142, no. 6, p. 03116005, 2016.

[7]P. A. Madsen, H. B. Bingham, and H. A. Schäffer, "Boussinesq-type formulations for fully nonlinear and extremely dispersive water waves: derivation and analysis," *Proceedings of the Royal Society of London A: Mathematical, Physical and Engineering Sciences*, vol. 459, no. 2033, pp. 1075–1104, 2003. [Online]. Available: http://rspa.royalsocietypublishing.org/content/459/2033/1075

[8]Y. Yamazaki, Z. Kowalik, and K. F. Cheung, "Depth-integrated, non-hydrostatic model for wave breaking and run-up," *International Journal for Numerical Methods in Fluids*, vol. 61, no. 5, pp. 473–497, 2008. [Online]. Available: https://onlinelibrary.wiley.com/doi/abs/10.1002/fld.1952

[9]M. Zijlema and G. Stelling, "Efficient computation of surf zone waves using the nonlinear shallow water equations with non-hydrostatic pressure," *Coastal Engineering*, vol. 55, no. 10, pp. 780–790, 2008. [Online]. Available:

http://www.sciencedirect.com/science/article/pii/S0378383908000380

[10]G. Ma, F. Shi, and J. Kirby, "Shock-capturing non-hydrostatic model for fully dispersive surface wave processes," *Ocean Modelling*, vol. 43-44, pp. 22–35, 2012.

[11]X. Lu and S. Xie, "Depth-averaged non-hydrostatic numerical modeling of nearshore wave propagations based on the FORCE scheme," *Coastal Engineering*, vol. 114, pp. 208–219, 2016. [Online]. Available: http://www.sciencedirect.com/science/article/pii/S0378383916300436

[12]C. Raoult, M. Benoit, and M. L. Yates, "Validation of a fully nonlinear and dispersive wave model with laboratory non-breaking experiments," *Coastal Engineering*, vol. 114, pp. 194–207, 2016. [Online]. Available: http://www.sciencedirect.com/science/article/pii/S0378383916300461

[13]M. Antuono and M. Brocchini, "Beyond Boussinesq-type equations: Semi-integrated models for coastal dynamics," *Physics of Fluids*, vol. 25, no. 1, 2013. [Online]. Available: http://scitation.aip.org/content/aip/journal/pof2/25/1/10.1063/1.4774343

[14]M. Antuono, G. Colicchio, C. Lugni, M. Greco, and M. Brocchini, "A depth semi-averaged model for coastal dynamics," *Physics of Fluids*, vol. 29, no. 5, p. 056603, 2017.

[15]A. Alberello, M. Onorato, F. Frascoli, and A. Toffoli, "Observation of turbulence and intermittency in wave-induced oscillatory flows," *Wave Motion*, vol. 84, pp. 81–89, 2019. [Online]. Available: http://www.sciencedirect.com/science/article/pii/S0165212518302026

[16]G. Wei, J. Kirby, S. Grilli, and R. Subramanya, "A fully nonlinear Boussinesq model for surface-waves. Part 1. highly nonlinear unsteady waves," *J. Fluid Mech.*, vol. 294, pp. 71–92, 1995.

[17]F. Shi, J. T. Kirby, J. C. Harris, J. D. Geiman, and S. T. Grilli, "A high-order adptive time-stepping TVD solver for Boussinesq modelling of breaking waves and coastal inundation," *Ocean Modelling*, vol. 43-44, pp. 36–51, 2012.

[18]J. Berkhoff, N. Booy, and A. Radder, "Verification of numerical wave propagation models for simple harmonic linear water waves," *Coastal Engineering*, vol. 6, no. 3, pp. 255–279, 1982.

[19]K. Meftah, P. Sergent, and P. Gomi, "Linear analysis of a new type of extended Boussinesq model," *Coastal Engineering*, vol. 51, no. 2, pp. 185–206, 2004. [Online]. Available: http://www.sciencedirect.com/science/article/pii/S0378383904000158

[20]P. Amestoy and I. Duff, "Vectorization of a multiprocessor multifrontal code," *International Journal of Supercomputer Applications*, vol. 3, pp. 41–59, 1989.

[21]P. Amestoy, I. Duff, J. Koster, and J.-Y. L'Excellent, "A fully asynchronous multifrontal solver using distributed dynamic scheduling," *SIAM Journal on Matrix Analysis and Applications*, vol. 23, no. 1, pp. 15–41, 2001.

[22]M. J. Briggs, C. E. Synolakis, G. S. Harkins, and D. R. Green, "Laboratory experiments of tsunami runup on a circular island," *Pure and applied geophysics*, vol. 144, no. 3-4, pp. 569–593, 1995.

[23]R. G. Dean and R. A. Dalrymple, *Water wave mechanics for engineers and scientists*. World Scientific Publishing Company, 1991, vol. 2.

[24]S. Yamamoto and H. Daiguji, "Higher-order-accurate upwind schemes for solving the compressible Euler and Navier-Stokes equations," *Computers Fluids*, vol. 2, no. 3, pp. 259–270, 1993.

[25]J. Zhou, D. Causon, C. Mingham, and D. Ingram, "The Surface Gradient Method for the Treatment of Source Terms in the Shallow-Water Equations," *Journal of Computational Physics*, vol. 168, no. 1, pp. 1–25, 2001. [Online]. Available: http://www.sciencedirect.com/science/article/pii/S0021999100966701

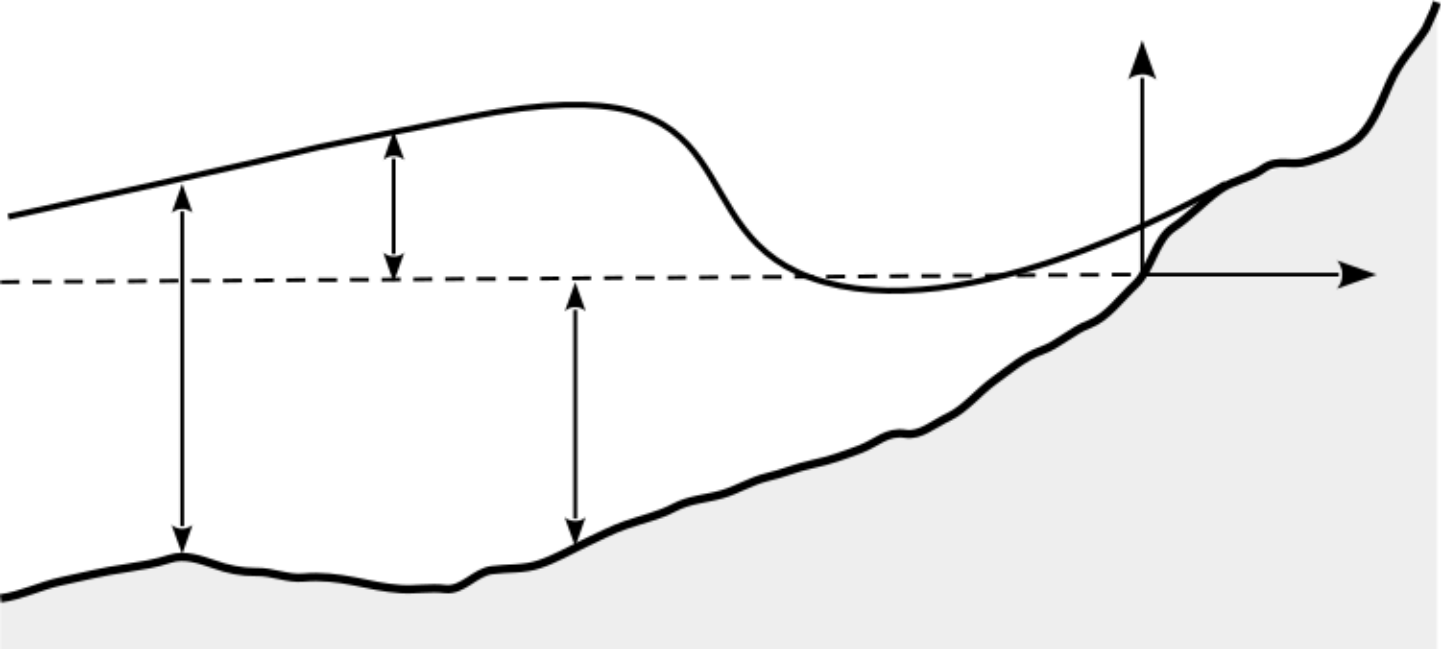

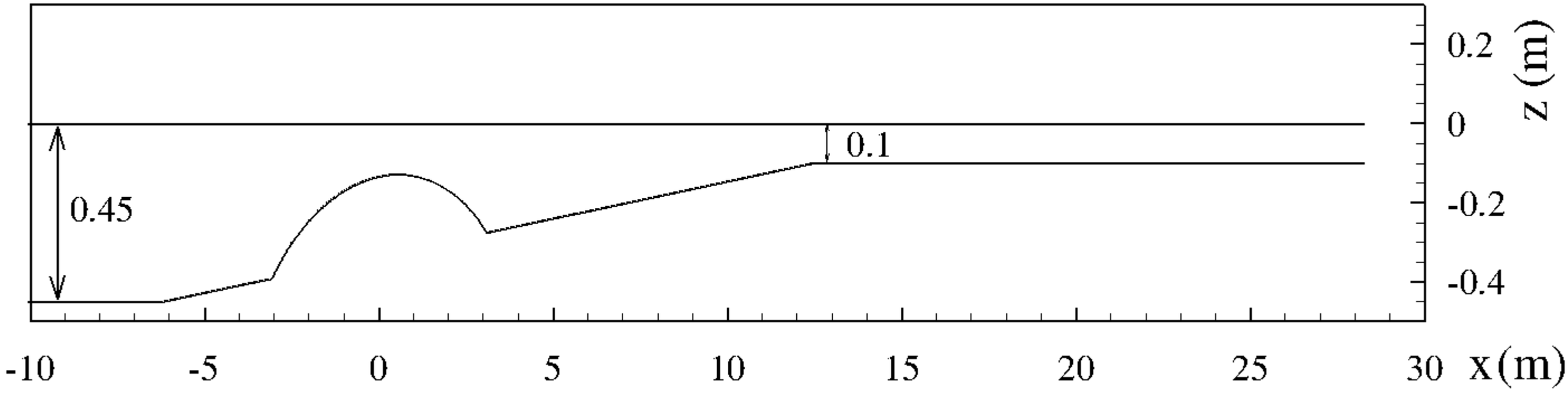
0.2
0
-0.2
-0.4
z (m)
0.45
0.1
-10
-5
0
5
10
15
20
25
30
x (m)

h (m)

0.10 0.16 0.21 0.27 0.32 0.38 0.43

10 5 0 -5 -10

y (m)

-10 -5 0 5 10 15 20

x (m)

1 2 3 4 5

6 7 8

Beach

η (m)

-0.05 -0.04 -0.02 -0.01 0.01 0.02 0.04 0.05

y (m)

10 5 0 -5 -10

-10 -5 0 5 10 15 20

x (m)

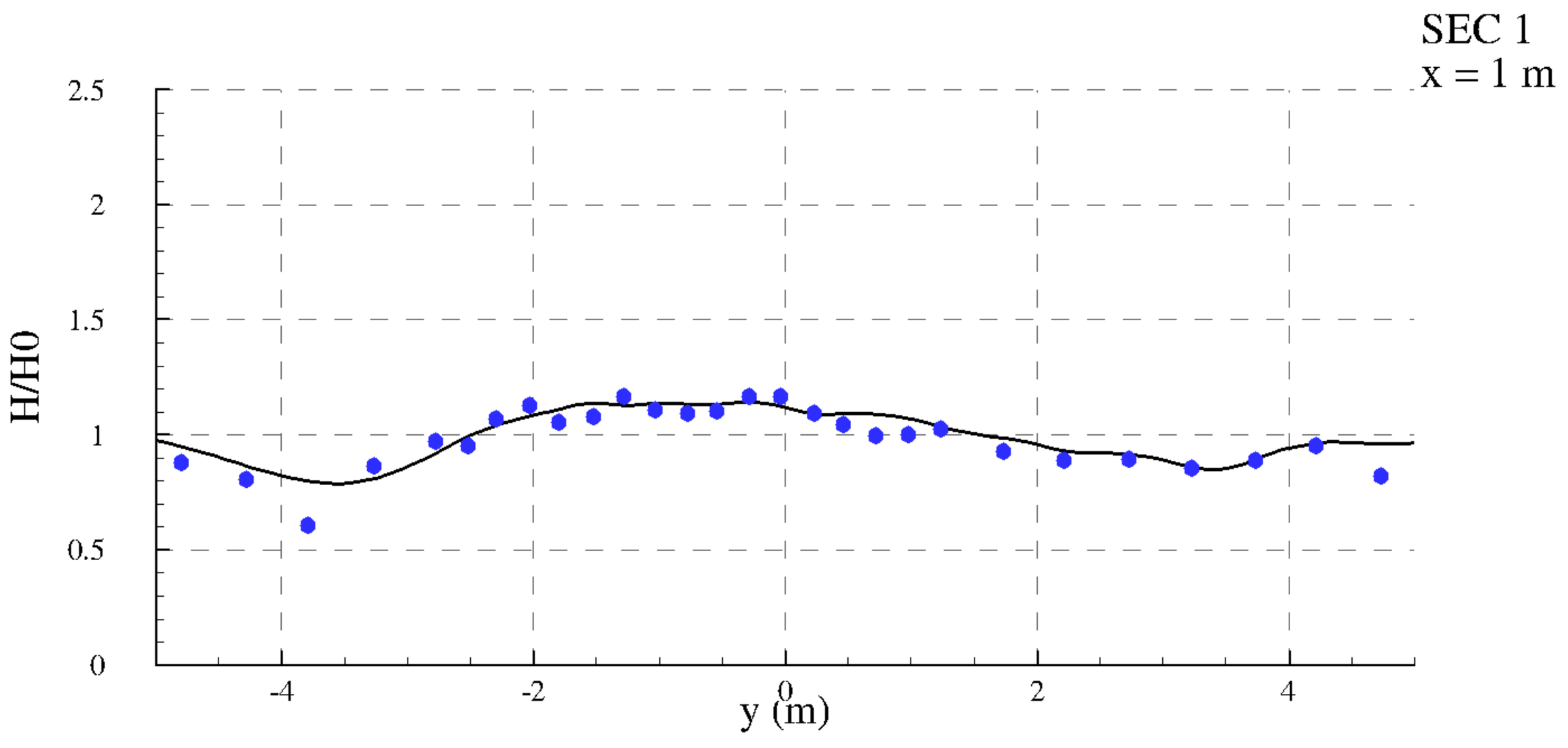
SEC 1
x = 1 m
H/H0
2.5
2
1.5
1
0.5
0
-4
-2
0
2
4
y (m)

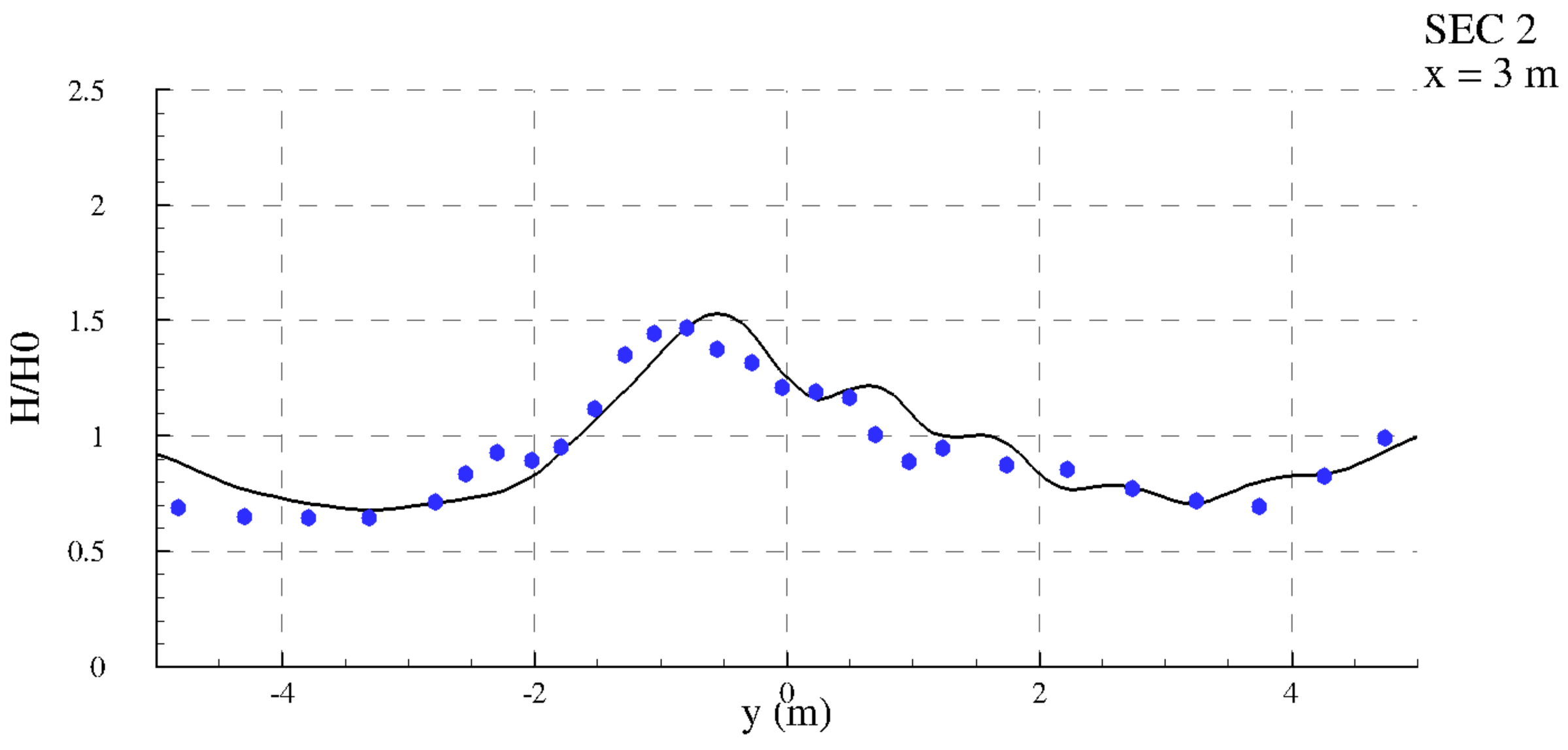
SEC 2
x = 3 m
H/H0
2.5
2
1.5
1
0.5
0
-4
-2
0
2
4
y (m)

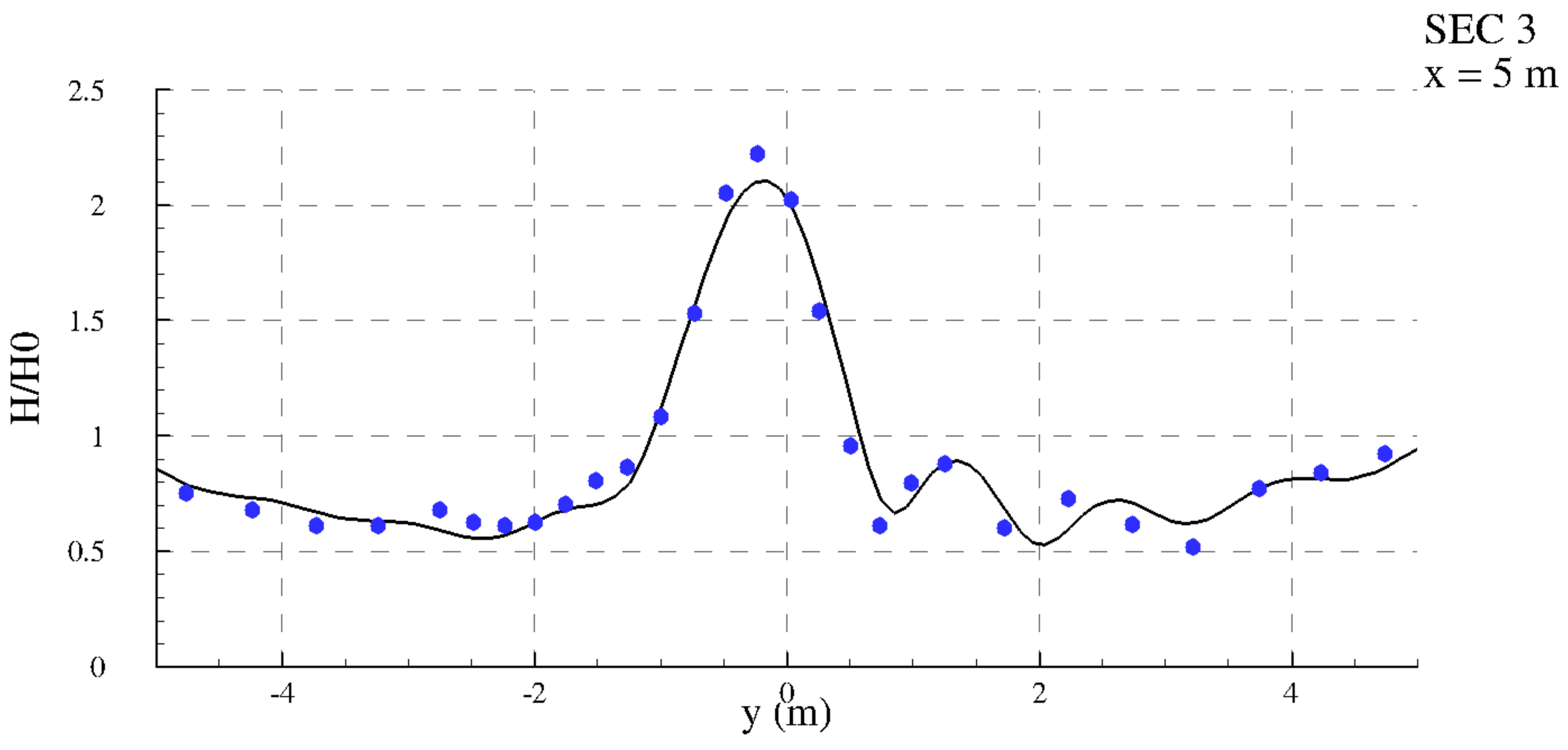
SEC 3
x = 5 m
H/H0
2.5
2
1.5
1
0.5
0
-4
-2
0
2
4
y (m)

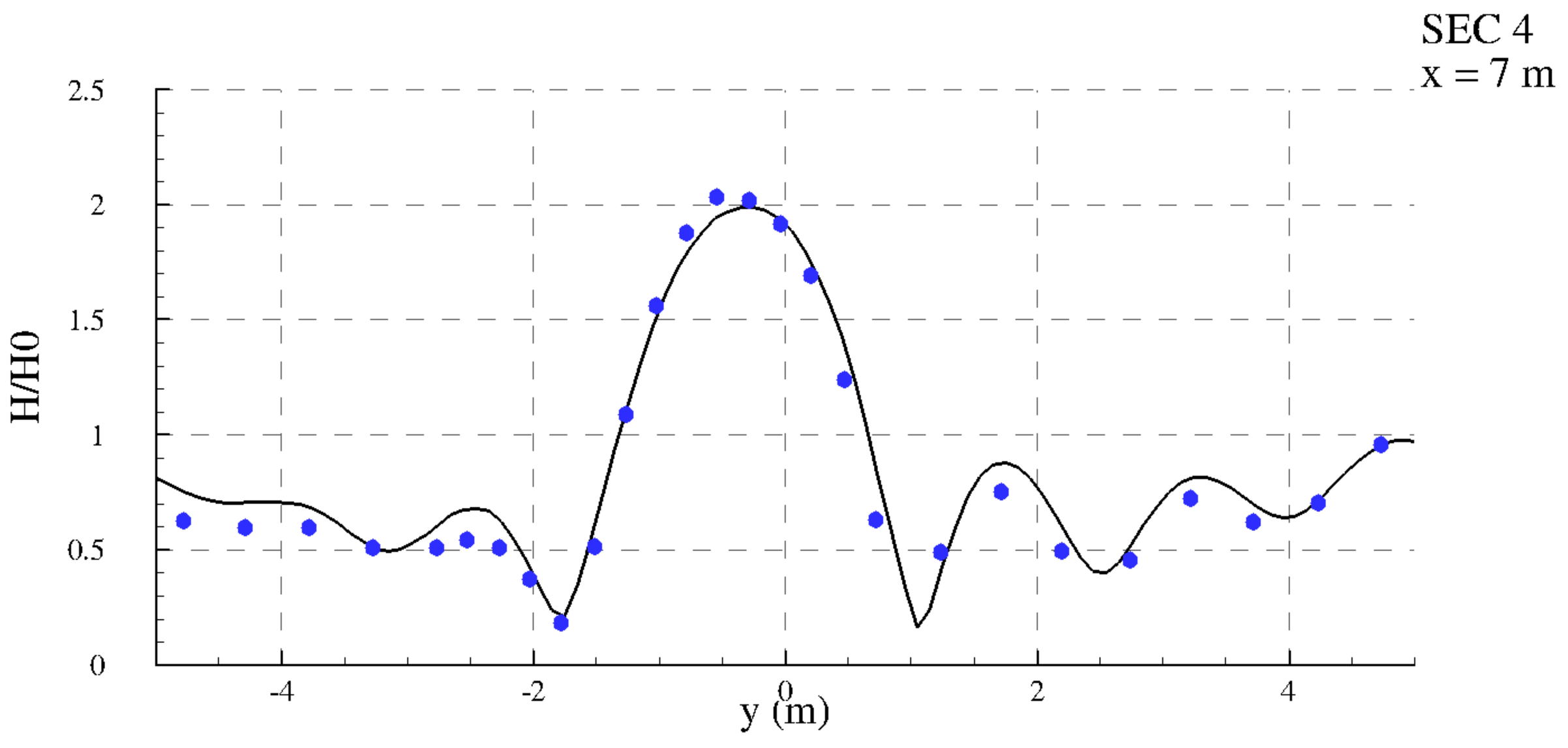
SEC 4
x = 7 m
H/H0
2.5
2
1.5
1
0.5
0
-4
-2
0
2
4
y (m)

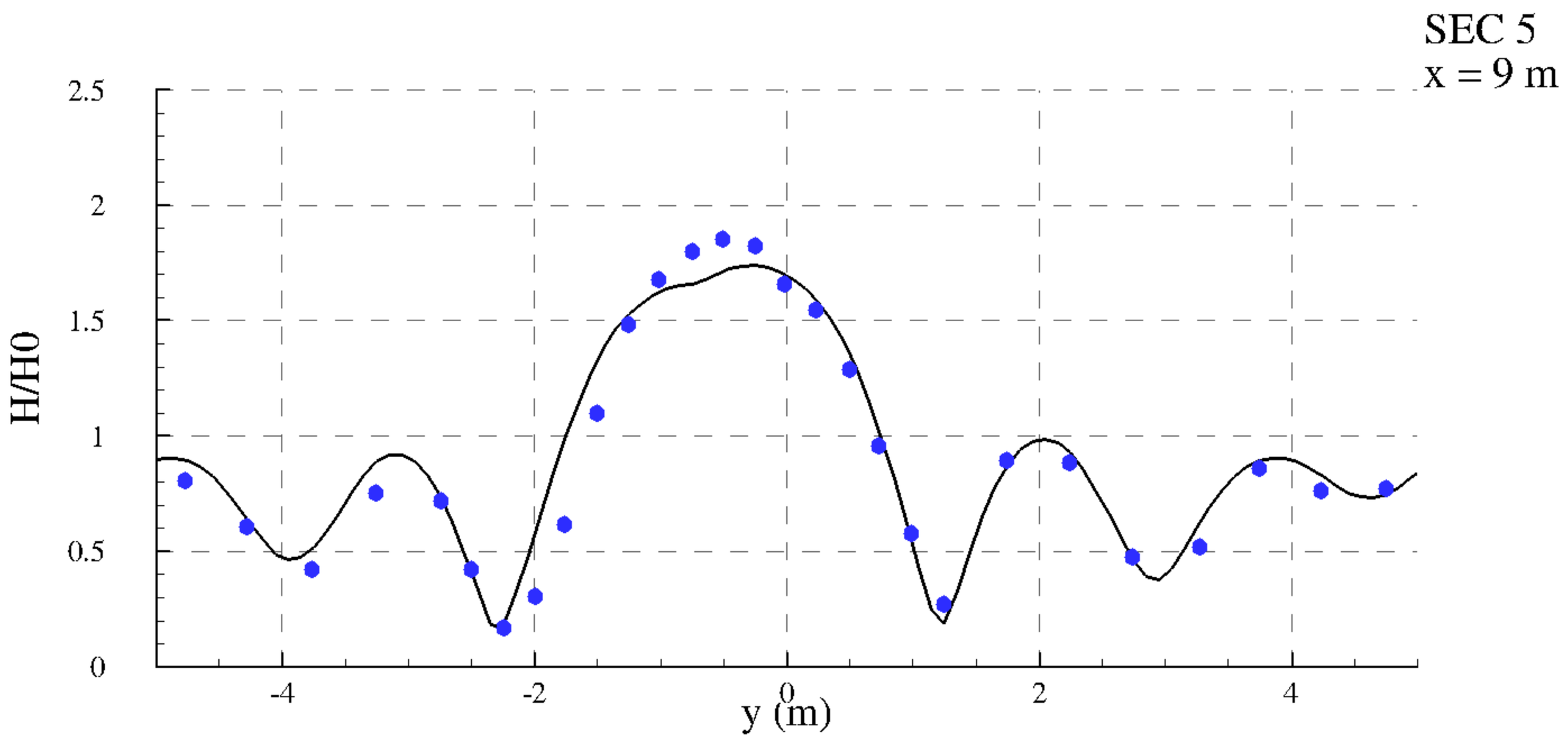
SEC 5
x = 9 m
H/H0
2.5
2
1.5
1
0.5
0
-4
-2
0
2
4
y (m)

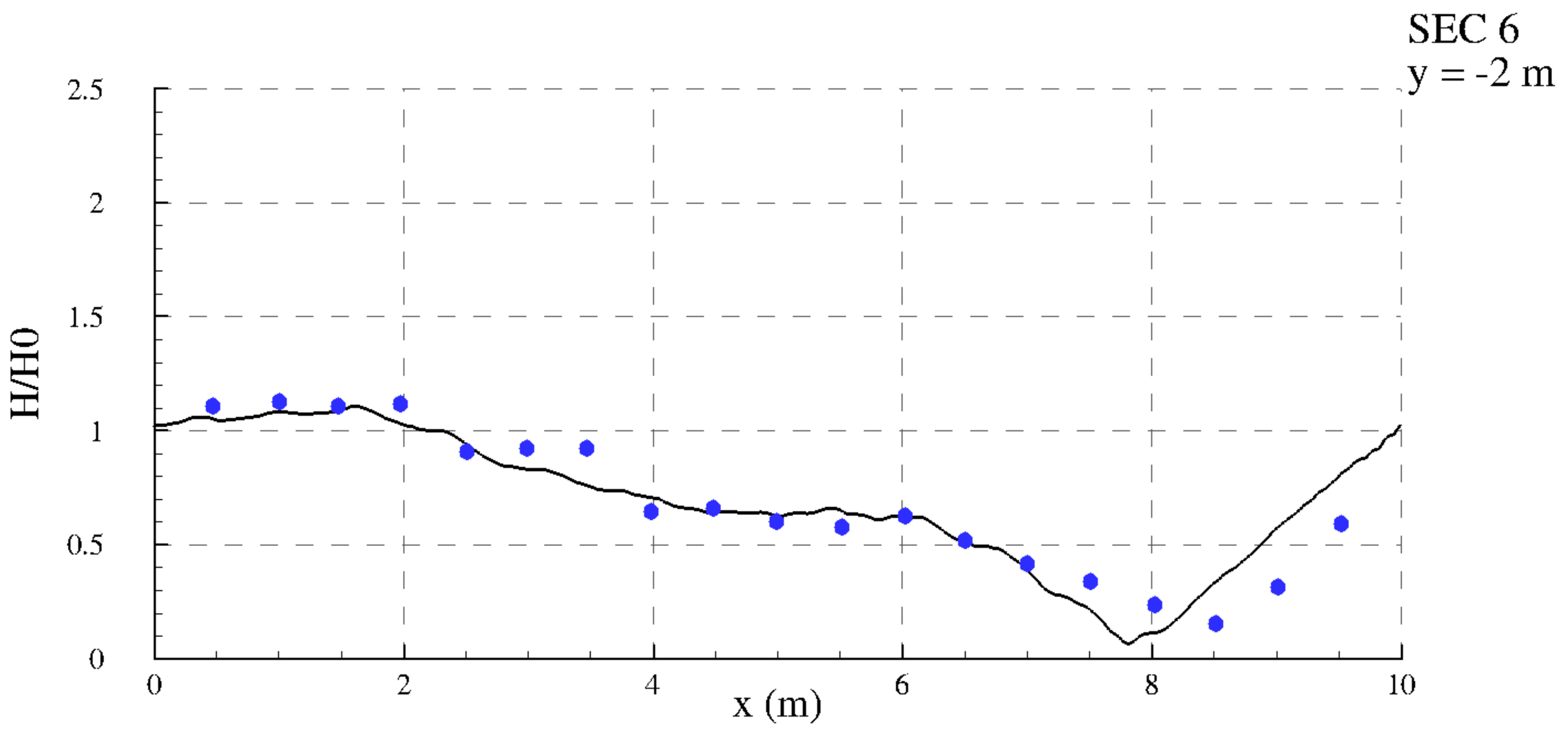
SEC 6
y = -2 m
H/H0
2.5
2
1.5
1
0.5
0
0
2
4
6
8
10
x (m)

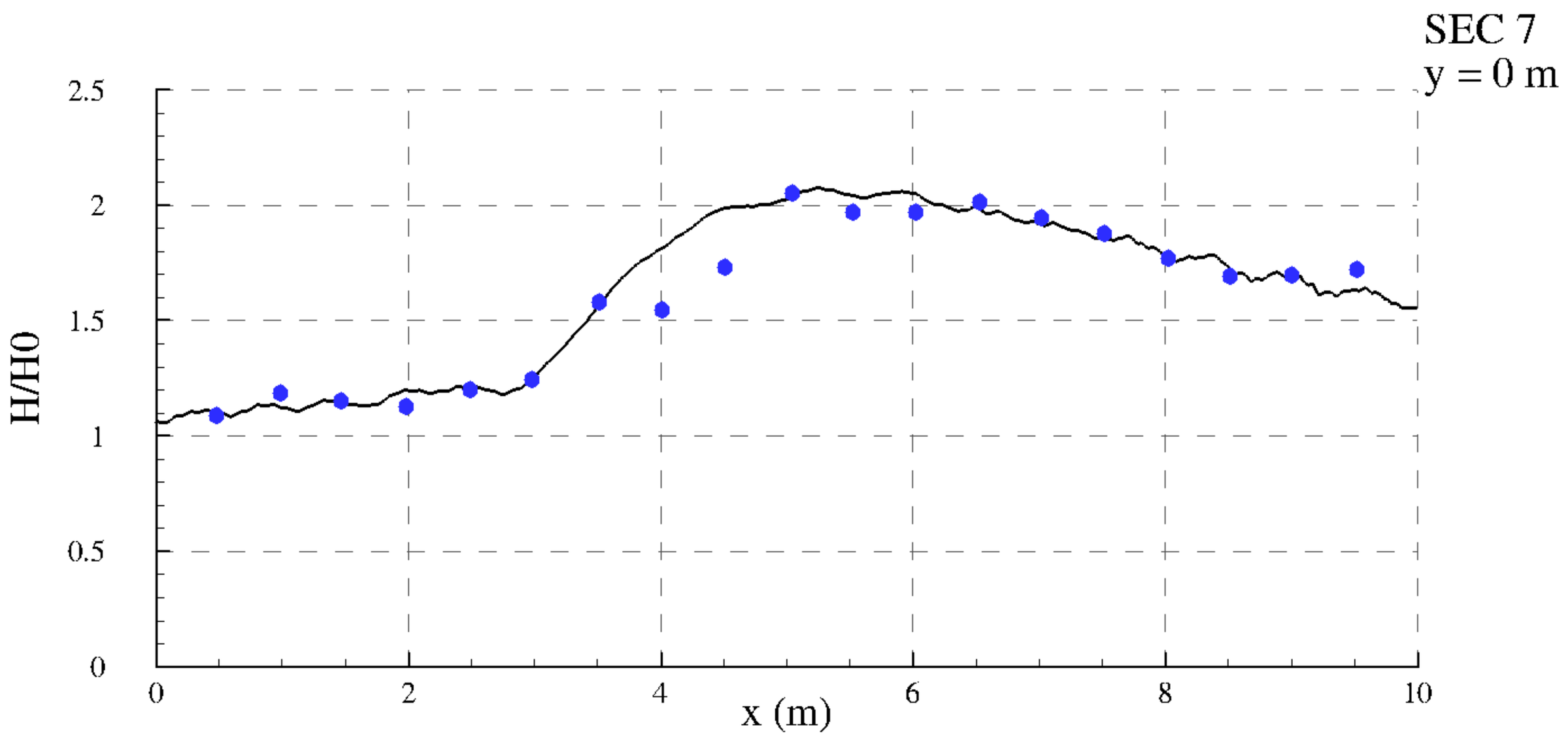
SEC 7
y = 0 m
H/H0
2.5
2
1.5
1
0.5
0
0
2
4
6
8
10
x (m)

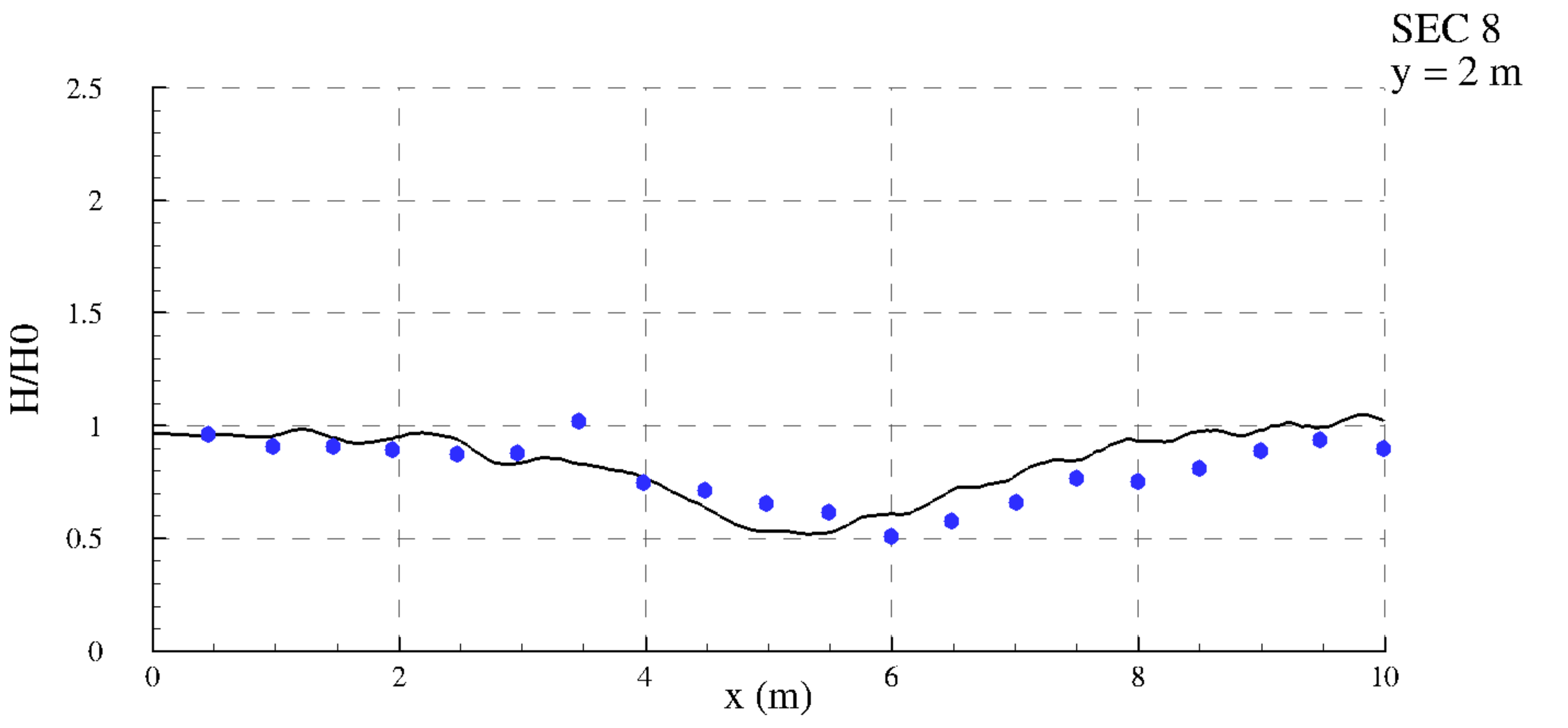
SEC 8
y = 2 m
H/H0
2.5
2
1.5
1
0.5
0
0
2
4
6
8
10
x (m)

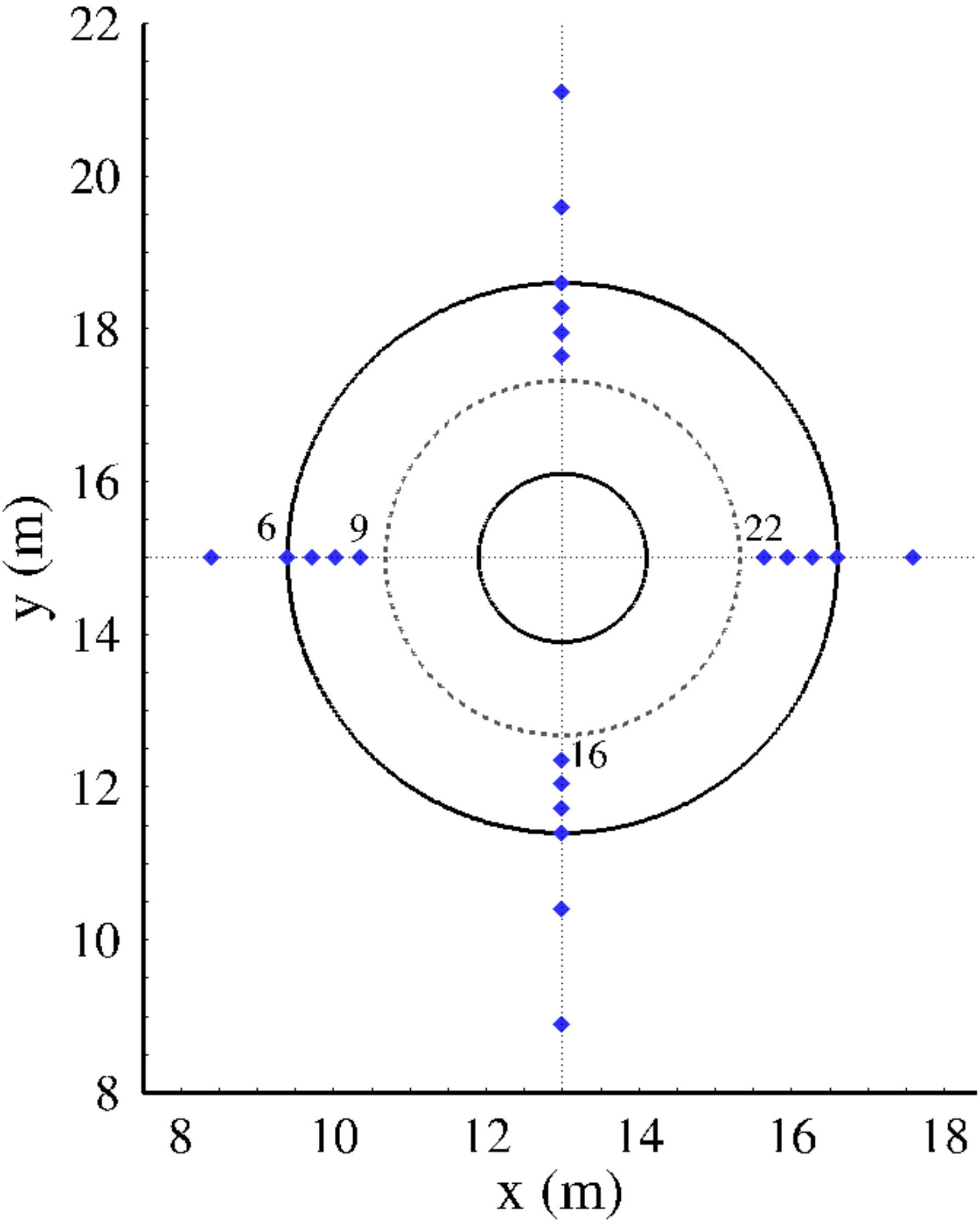
22
20
18
16
14
12
10
8
y (m)
6
9
22
16
8
10
12
14
16
18
x (m)

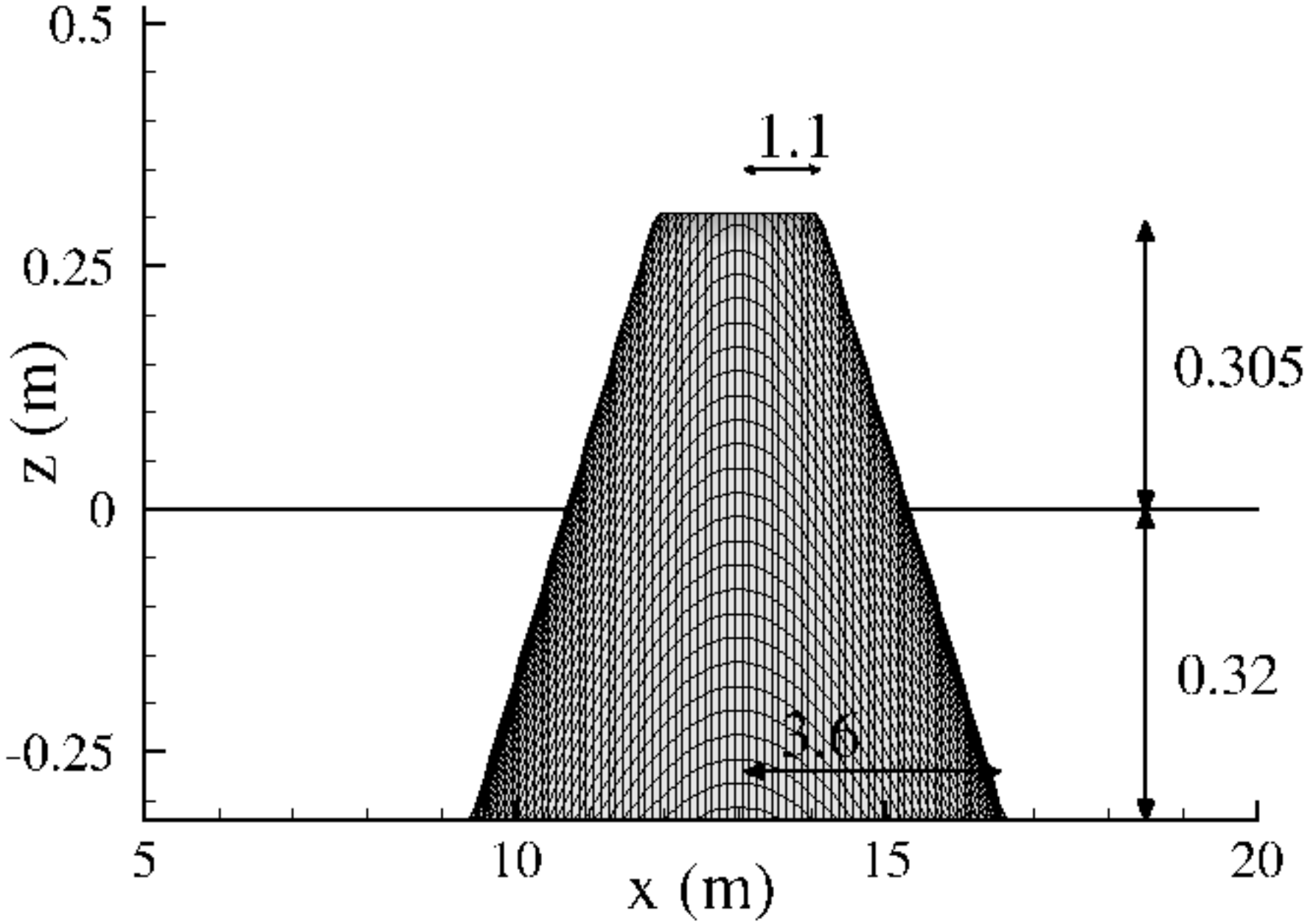
0.5
0.25
0
-0.25
z (m)
1.1
0.305
0.32
3.6
5
10
15
20
x (m)

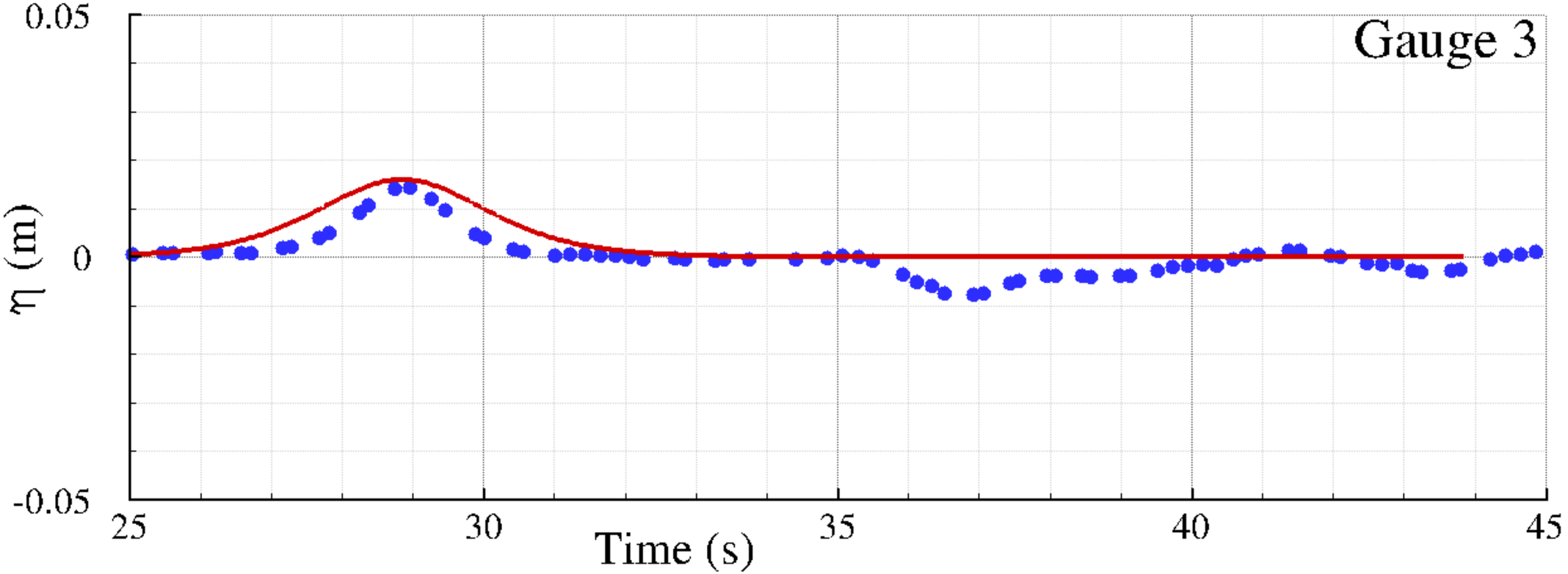
Gauge 3
0.05
0
-0.05
η (m)
25
30
35
40
45
Time (s)

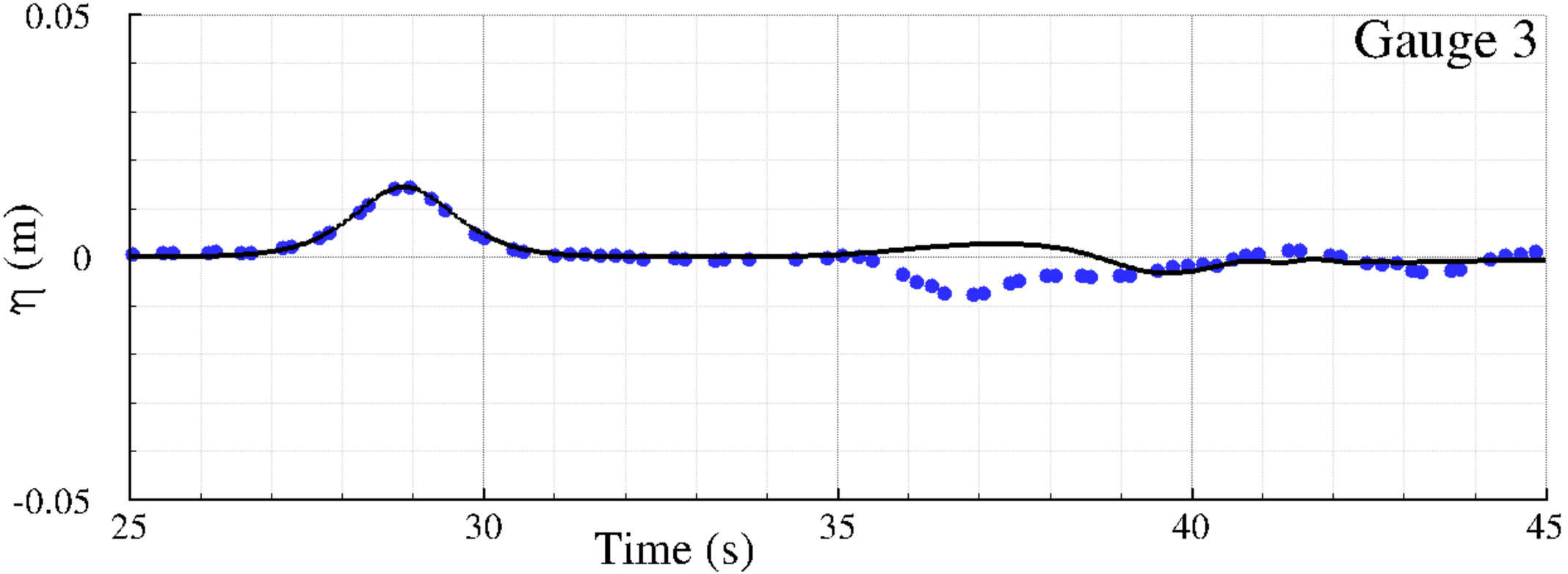
Gauge 3
0.05
0
-0.05
η (m)
25
30
35
40
45
Time (s)

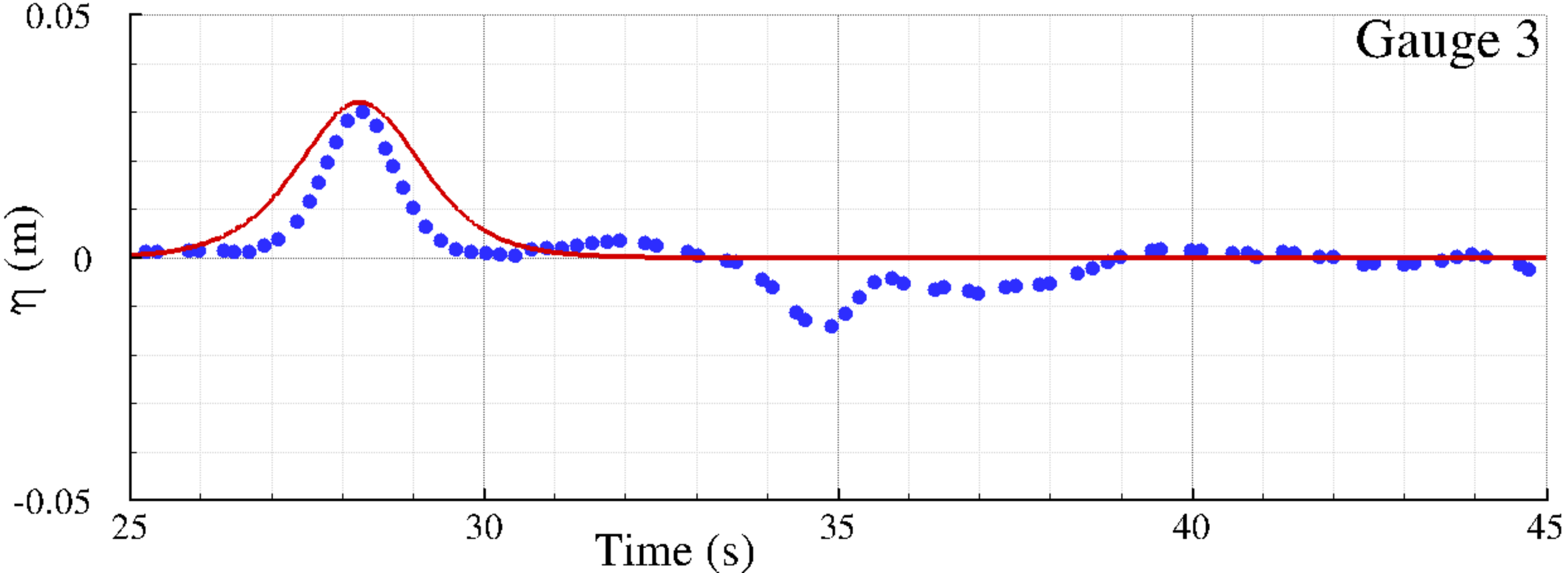
Gauge 3
0.05
0
-0.05
η (m)
25
30
35
40
45
Time (s)

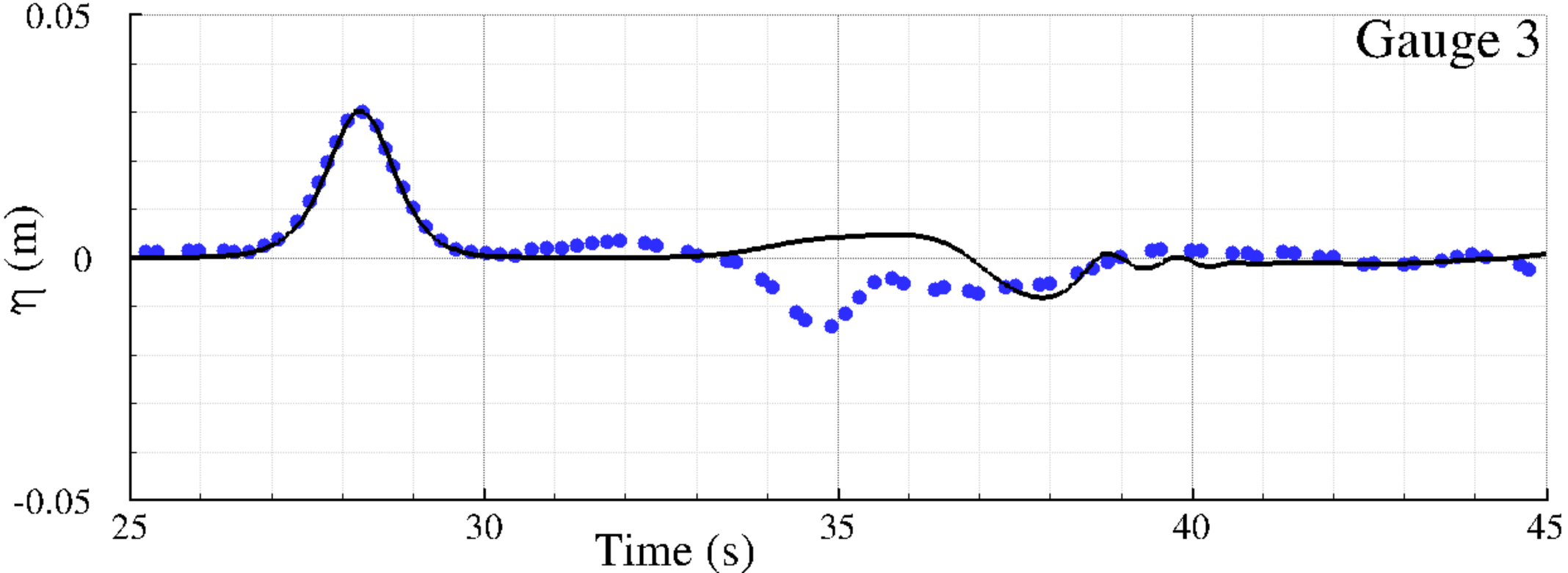
Gauge 3
0.05
0
-0.05
η (m)
25
30
35
40
45
Time (s)

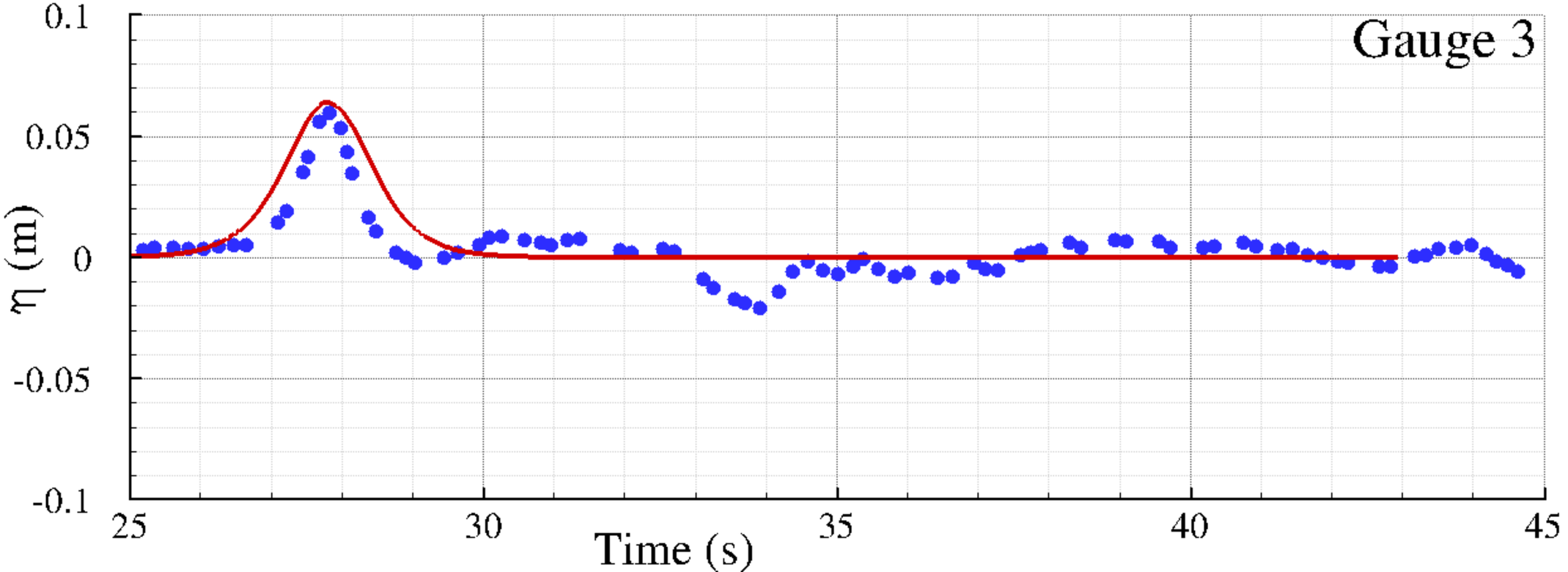
Gauge 3
0.1
0.05
0
-0.05
-0.1
η (m)
25
30
35
40
45
Time (s)

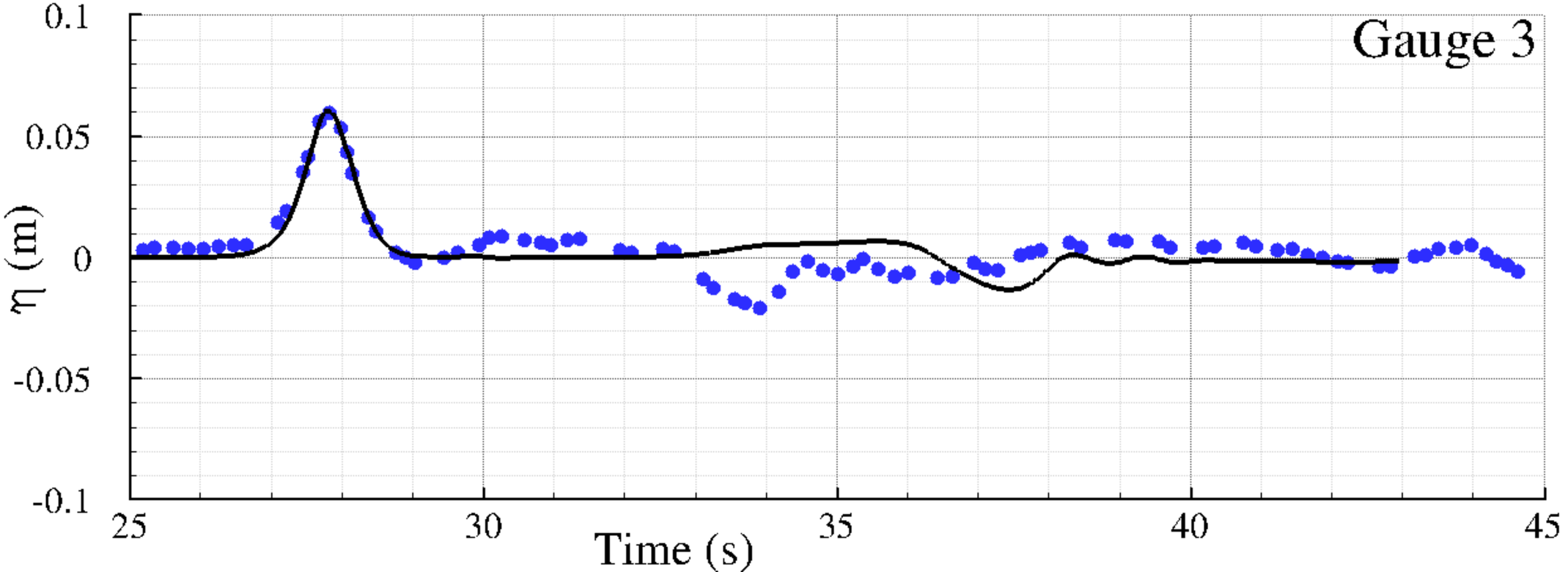
Gauge 3
0.1
0.05
0
-0.05
-0.1
η (m)
25
30
35
40
45
Time (s)

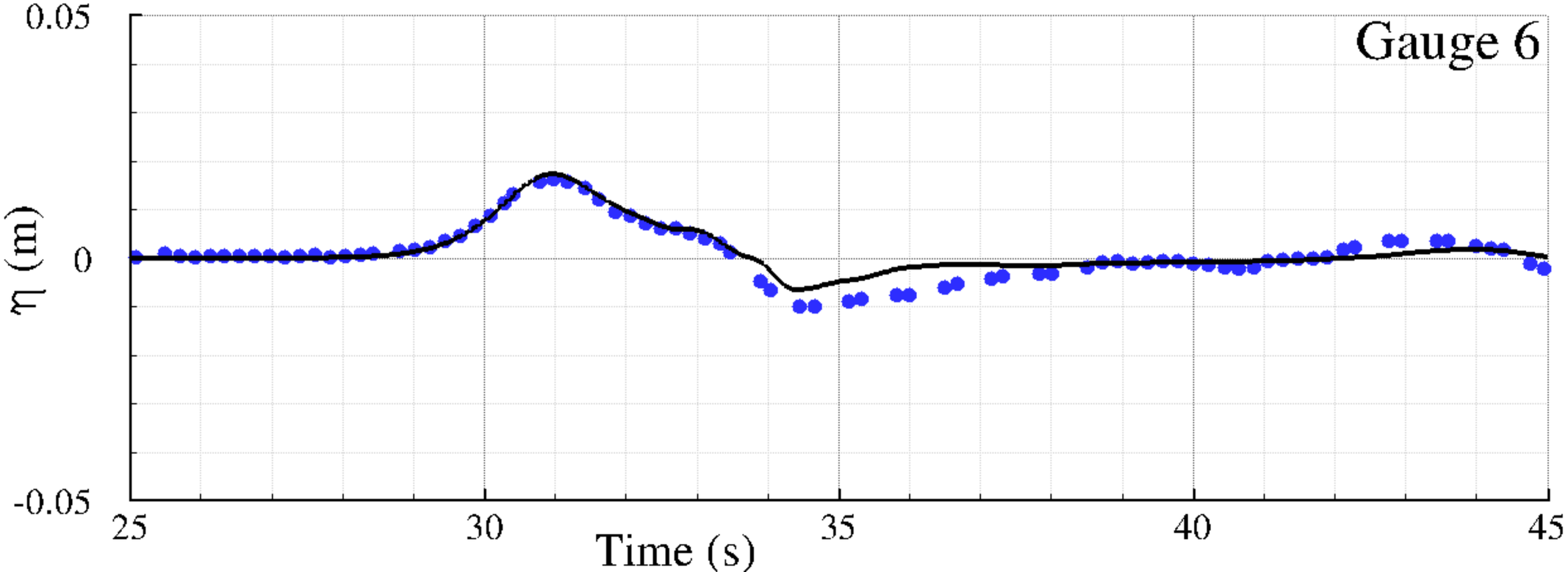
Gauge 6
0.05
0
-0.05
η (m)
25
30
35
40
45
Time (s)

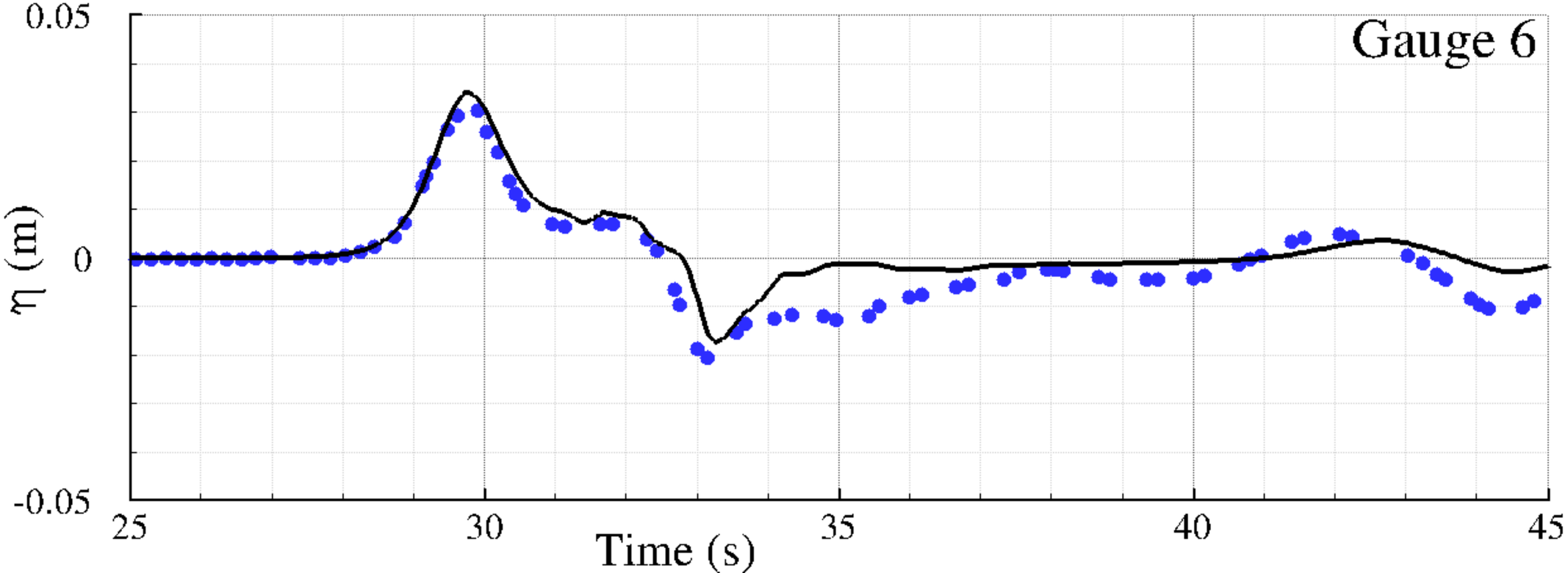
Gauge 6
0.05
0
-0.05
η (m)
25
30
35
40
45
Time (s)

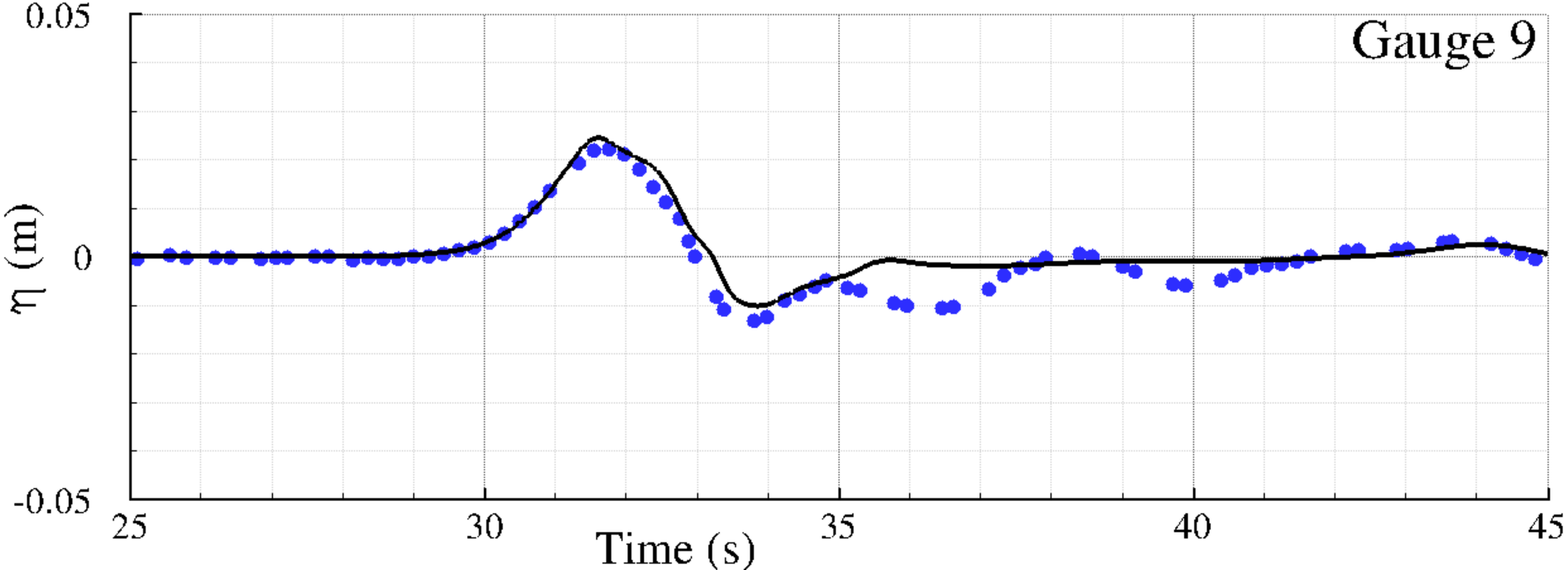
Gauge 9
0.05
0
-0.05
η (m)
25
30
35
40
45
Time (s)

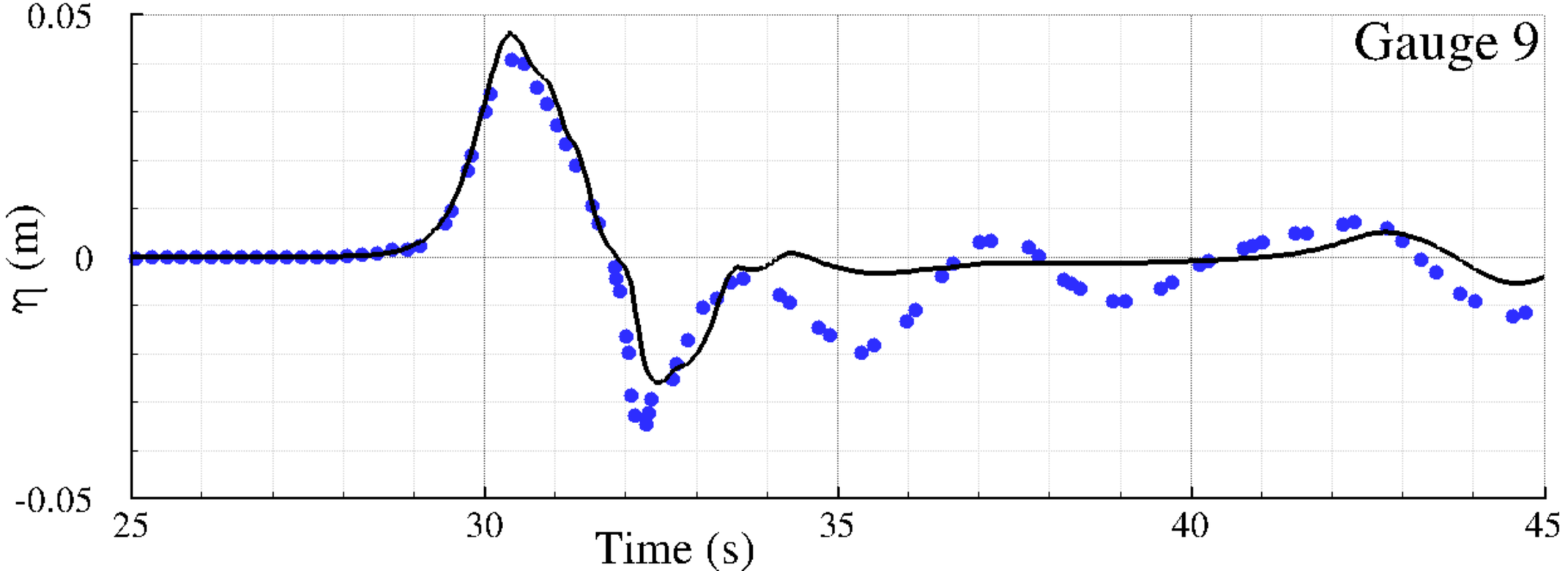
Gauge 9
0.05
0
-0.05
η (m)
25
30
35
40
45
Time (s)

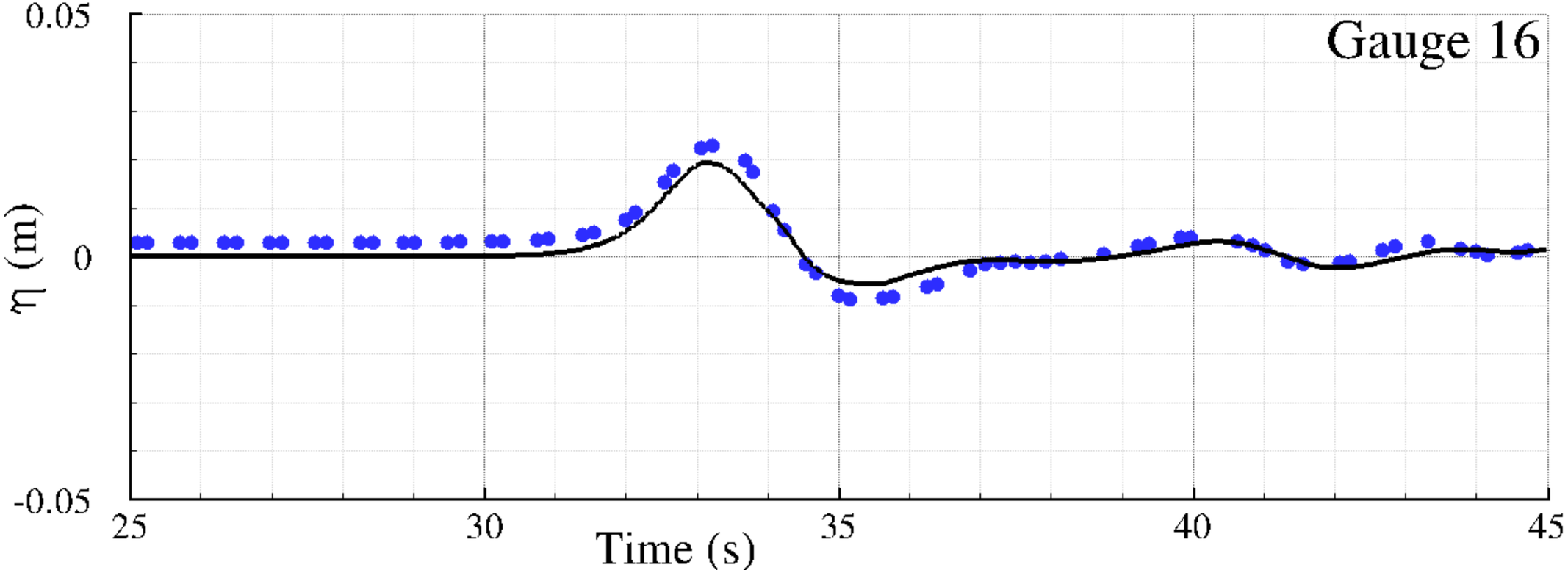
Gauge 16
0.05
0
-0.05
η (m)
25
30
35
40
45
Time (s)

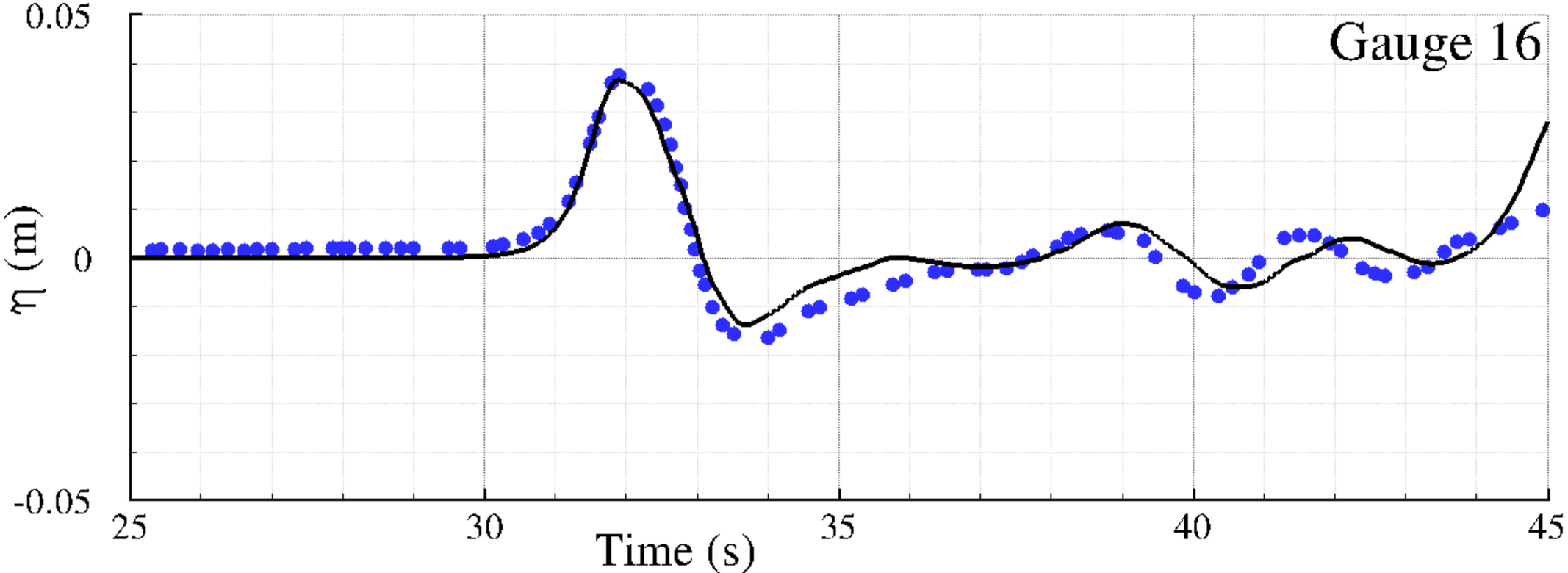
Gauge 16
0.05
0
-0.05
η (m)
25
30
35
40
45
Time (s)

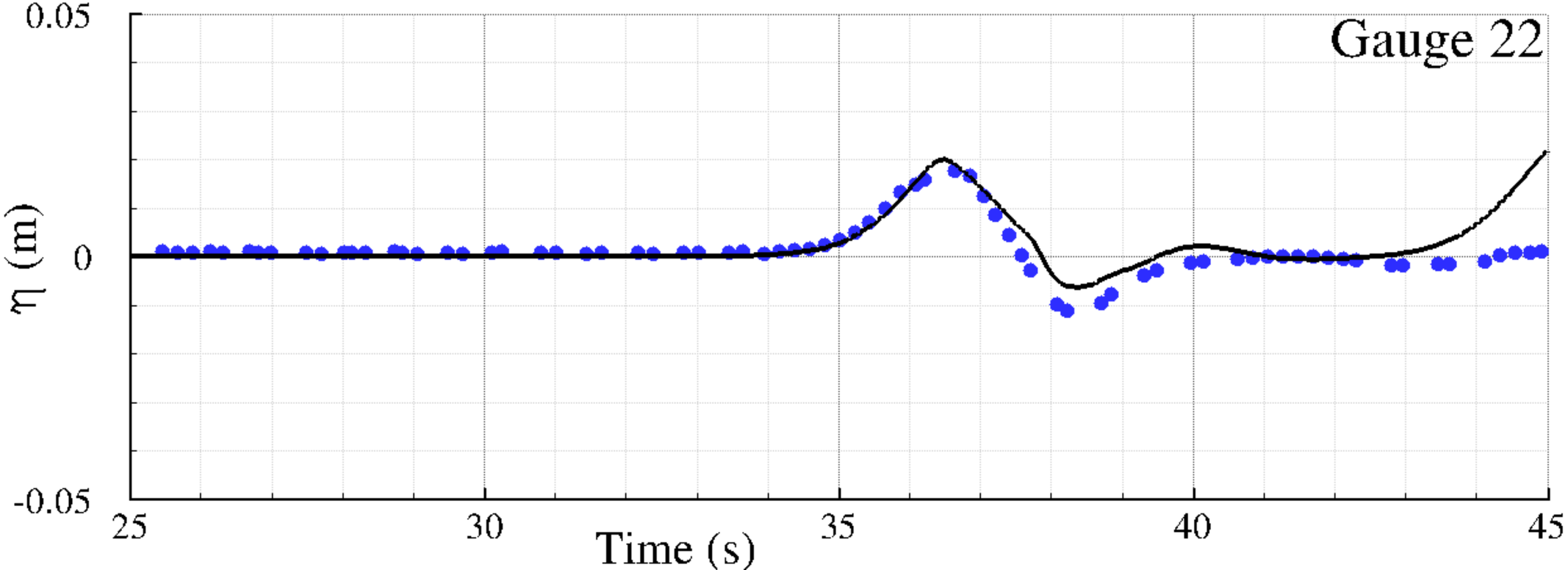
Gauge 22
0.05
0
-0.05
η (m)
25
30
35
40
45
Time (s)

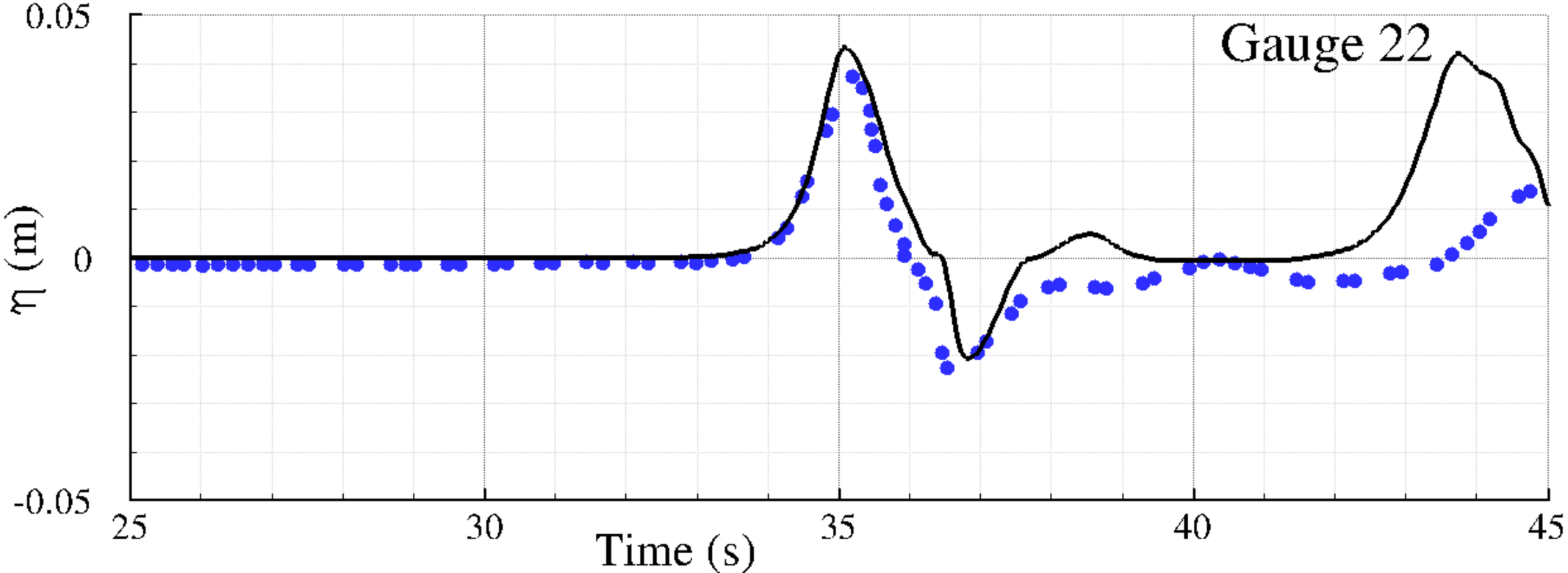
Gauge 22
0.05
0
-0.05
η (m)
25
30
35
40
45
Time (s)

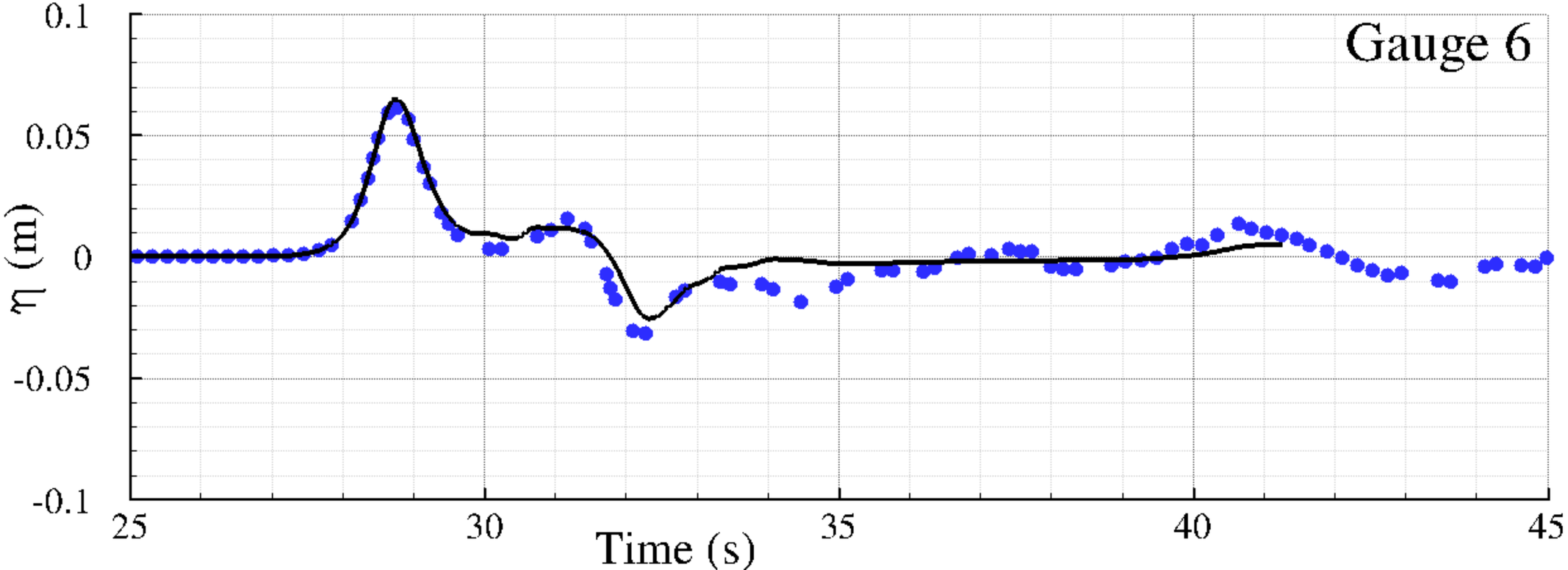
Gauge 6
0.1
0.05
0
-0.05
-0.1
η (m)
25
30
35
40
45
Time (s)

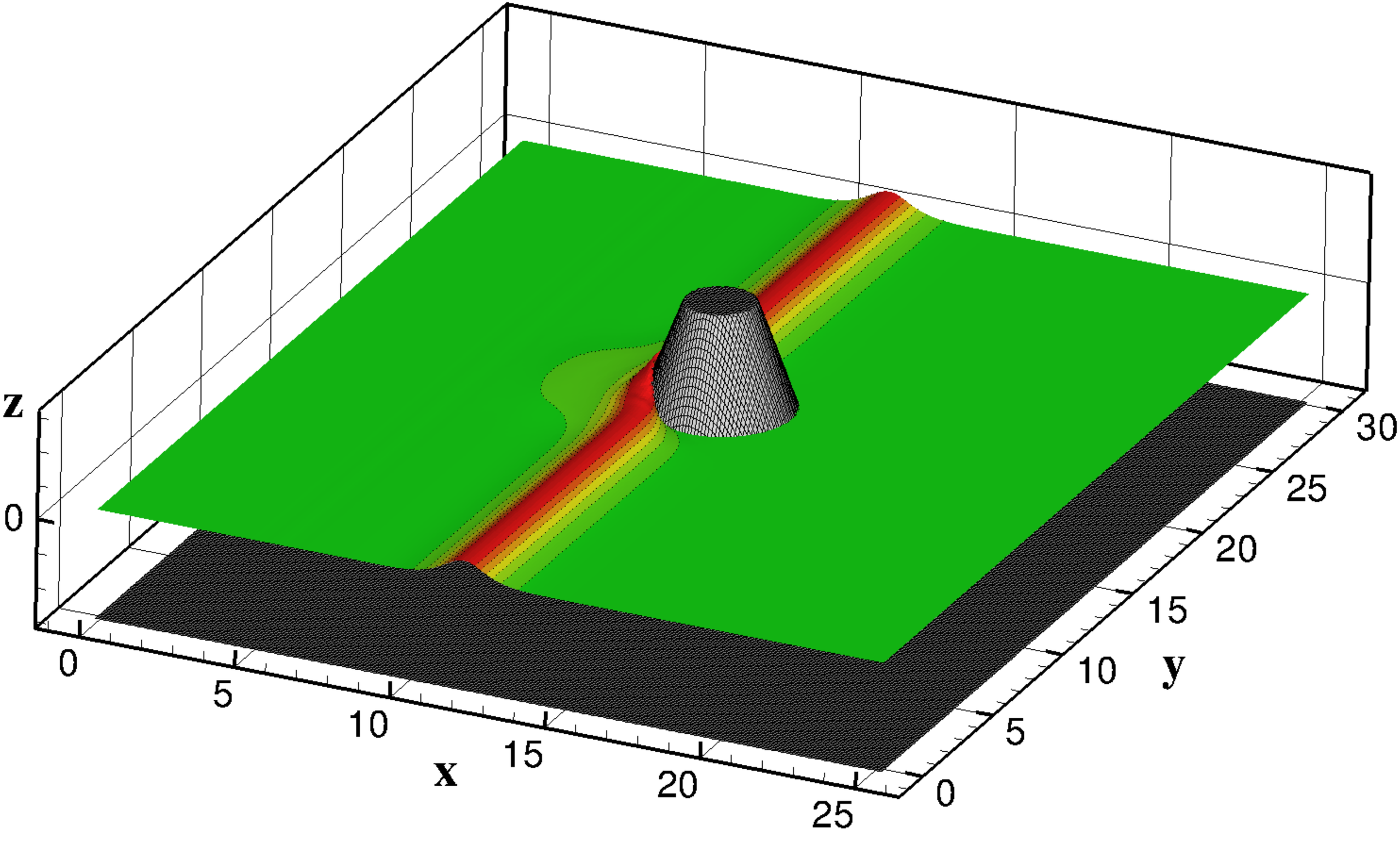
z
0
0
5
10
15
20
25
x
0
5
10
15
20
25
30
y

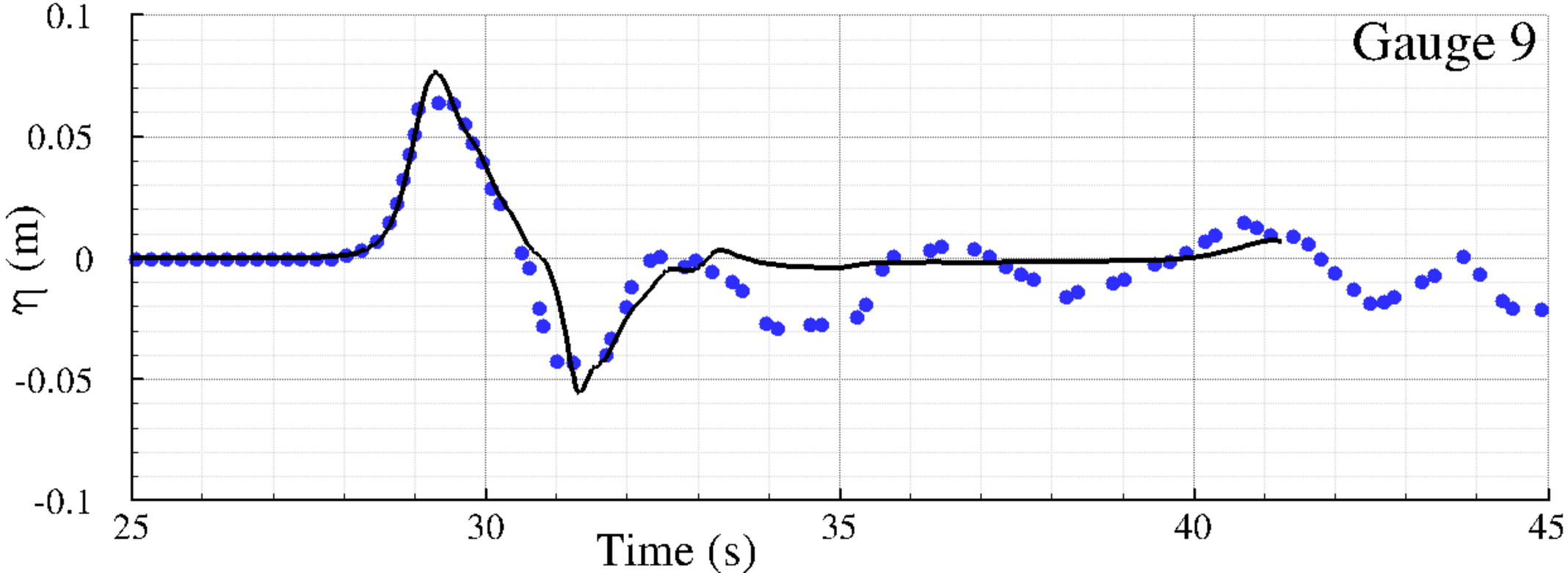
Gauge 9
0.1
0.05
0
-0.05
-0.1
η (m)
25
30
35
40
45
Time (s)

z

0

0

5

10

15

20

25

x

0

5

10

15

20

25

y

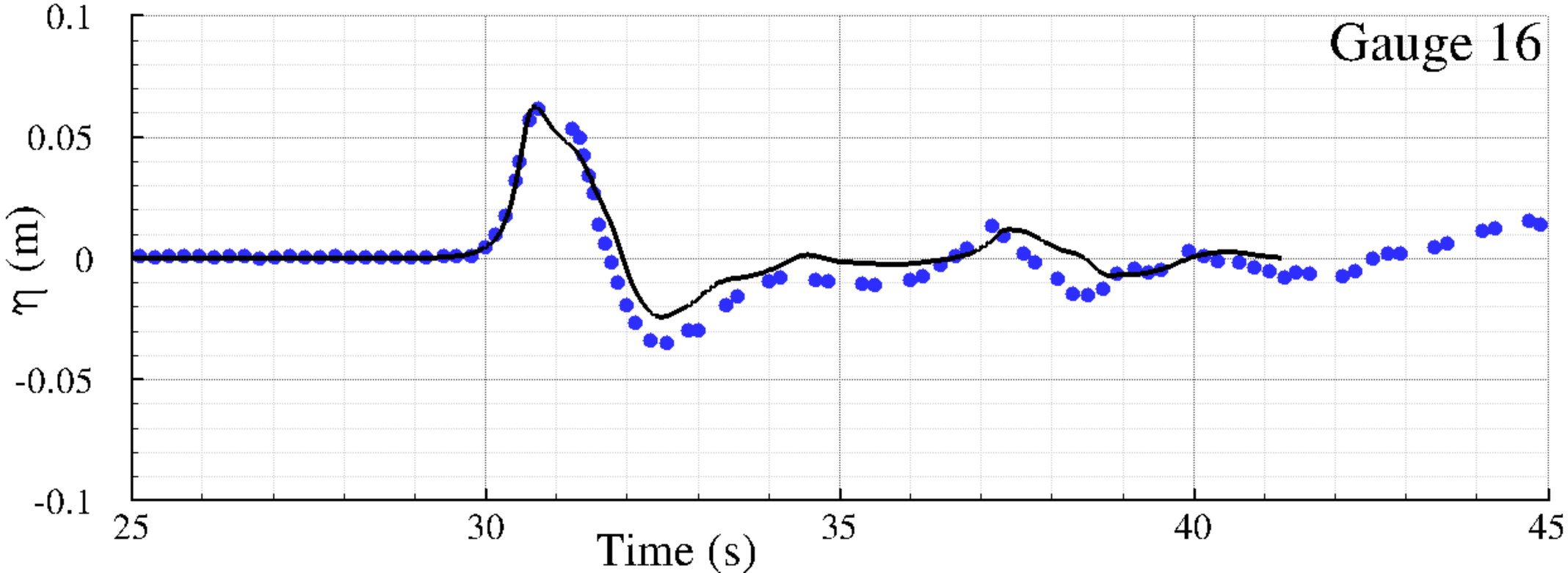
Gauge 16
0.1
0.05
0
-0.05
-0.1
η (m)
25
30
35
40
45
Time (s)

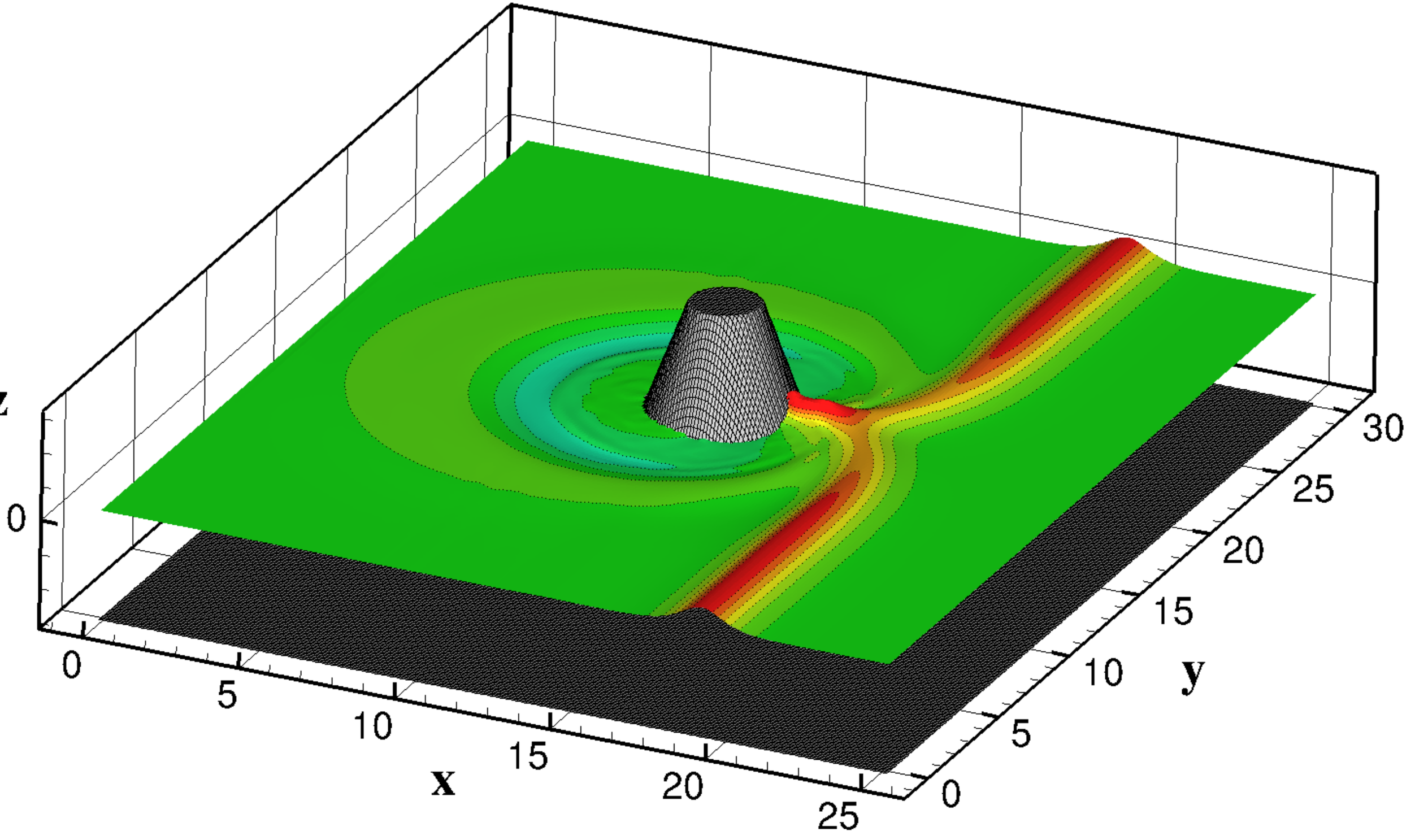
z
0
0
5
10
15
20
25
x
0
5
10
15
20
25
30
y

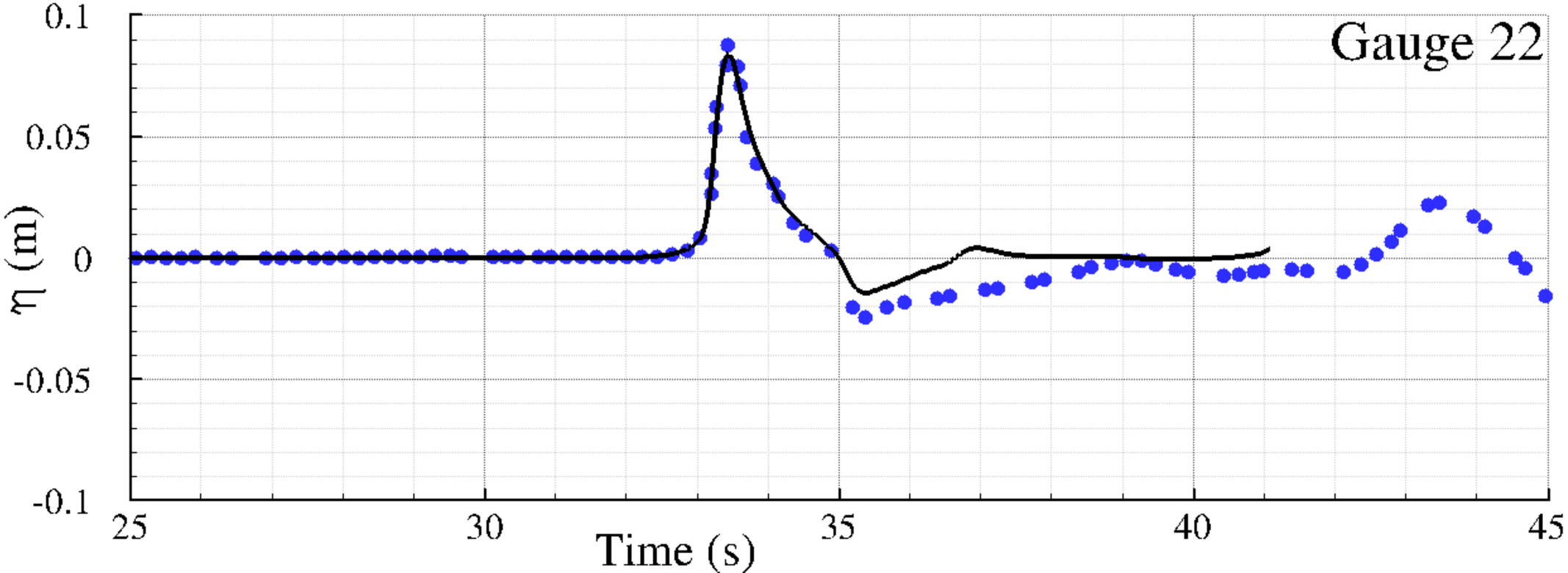
Gauge 22
0.1
0.05
0
-0.05
-0.1
η (m)
25
30
35
40
45
Time (s)

z

0

0

5

10

15

20

25

x

0

5

10

15

20

25

30

y

η(m)

-0.050 -0.032 -0.014 0.005 0.023 0.041

$\varepsilon = 0.05$

$\frac{1}{2}\pi$ $\frac{5}{8}\pi$ $\frac{3}{8}\pi$ $\frac{3}{4}\pi$ $\frac{1}{4}\pi$ $\frac{7}{8}\pi$ $\frac{1}{8}\pi$ $\pi$ 0 $-\frac{7}{8}\pi$ $-\frac{1}{8}\pi$ $-\frac{3}{4}\pi$ $-\frac{1}{4}\pi$ $-\frac{5}{8}\pi$ $-\frac{3}{8}\pi$ $-\frac{1}{2}\pi$

0 1.5 3

$\varepsilon = 0.05$

$\frac{1}{2}\pi$

$\frac{5}{8}\pi$

$\frac{3}{8}\pi$

$\frac{3}{4}\pi$

$\frac{1}{4}\pi$

$\frac{7}{8}\pi$

$\frac{1}{8}\pi$

$-\pi$

$0$

0

1.5

3

$-\frac{7}{8}\pi$

$-\frac{1}{8}\pi$

$-\frac{3}{4}\pi$

$-\frac{1}{4}\pi$

$-\frac{5}{8}\pi$

$-\frac{3}{8}\pi$

$-\frac{1}{2}\pi$

$\varepsilon = 0.1$

$\frac{1}{2}\pi$

$\frac{5}{8}\pi$

$\frac{3}{8}\pi$

$\frac{3}{4}\pi$

$\frac{1}{4}\pi$

$\frac{7}{8}\pi$

$\frac{1}{8}\pi$

$-\pi$

0

0

1.5

3

$-\frac{7}{8}\pi$

$-\frac{1}{8}\pi$

$-\frac{3}{4}\pi$

$-\frac{1}{4}\pi$

$-\frac{5}{8}\pi$

$-\frac{3}{8}\pi$

$-\frac{1}{2}\pi$

$\varepsilon = 0.1$

$\frac{1}{2}\pi$ $\frac{5}{8}\pi$ $\frac{3}{8}\pi$ $\frac{3}{4}\pi$ $\frac{1}{4}\pi$ $\frac{7}{8}\pi$ $\frac{1}{8}\pi$ $\pi$ 0 $-\frac{7}{8}\pi$ $-\frac{1}{8}\pi$ $-\frac{3}{4}\pi$ $-\frac{1}{4}\pi$ $-\frac{5}{8}\pi$ $-\frac{3}{8}\pi$ $-\frac{1}{2}\pi$

0 1.5 3

$\varepsilon = 0.2$

$\frac{1}{2}\pi$ $\frac{5}{8}\pi$ $\frac{3}{8}\pi$ $\frac{3}{4}\pi$ $\frac{1}{4}\pi$ $\frac{7}{8}\pi$ $\frac{1}{8}\pi$ $\pi$ 0 $-\frac{7}{8}\pi$ $-\frac{1}{8}\pi$ $-\frac{3}{4}\pi$ $-\frac{1}{4}\pi$ $-\frac{5}{8}\pi$ $-\frac{3}{8}\pi$ $-\frac{1}{2}\pi$

0 1.5 3

$\varepsilon = 0.2$

$\frac{1}{2}\pi$ $\frac{5}{8}\pi$ $\frac{3}{8}\pi$ $\frac{3}{4}\pi$ $\frac{1}{4}\pi$ $\frac{7}{8}\pi$ $\frac{1}{8}\pi$ $\pi$ $0$ $-\pi$ $-\frac{7}{8}\pi$ $-\frac{1}{8}\pi$ $-\frac{3}{4}\pi$ $-\frac{1}{4}\pi$ $-\frac{5}{8}\pi$ $-\frac{3}{8}\pi$ $-\frac{1}{2}\pi$

0 1.5 3

-0.50 -0.38 -0.26 -0.15 -0.03 0.09 0.21 0.32 0.44 0.50

10
5
0

40 30 20 10 0 -10 -20 -30 -40

0 20 40 60

-0.50 -0.29 -0.08 0.13 0.34 0.50

60

40

20

0

-10

10

0

4

2

0

-0.50 -0.38 -0.26 -0.15 -0.03 0.09 0.21 0.32 0.44 0.50

10
5
0

40 30 20 10 0 -10 -20 -30 -40

0 20 40 60

-0.50 -0.29 -0.08 0.13 0.34 0.50

4
2
0

10
0
-10

0
20
40
60

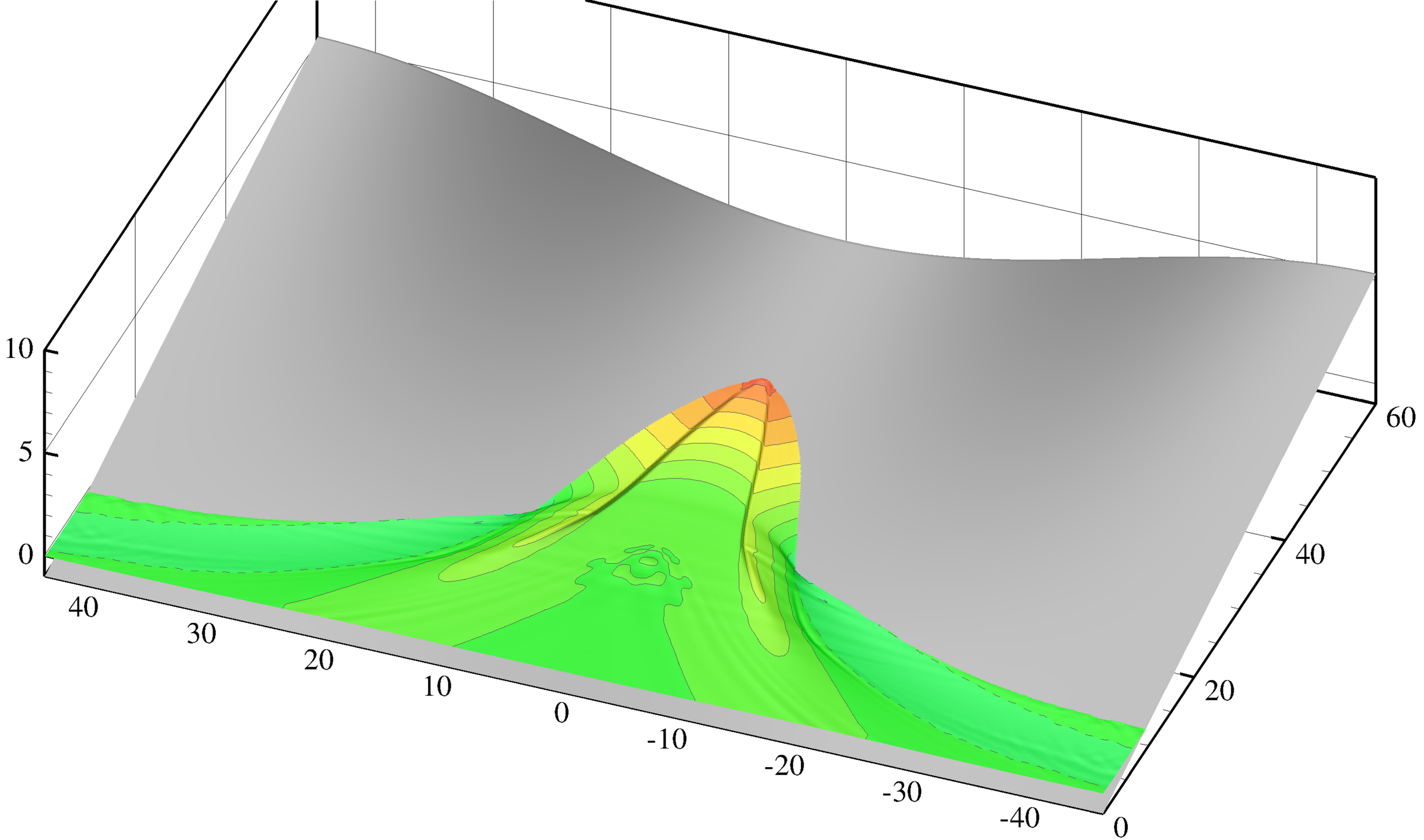
10
5
0
40
30
20
10
0
-10
-20
-30
-40
0
20
40
60

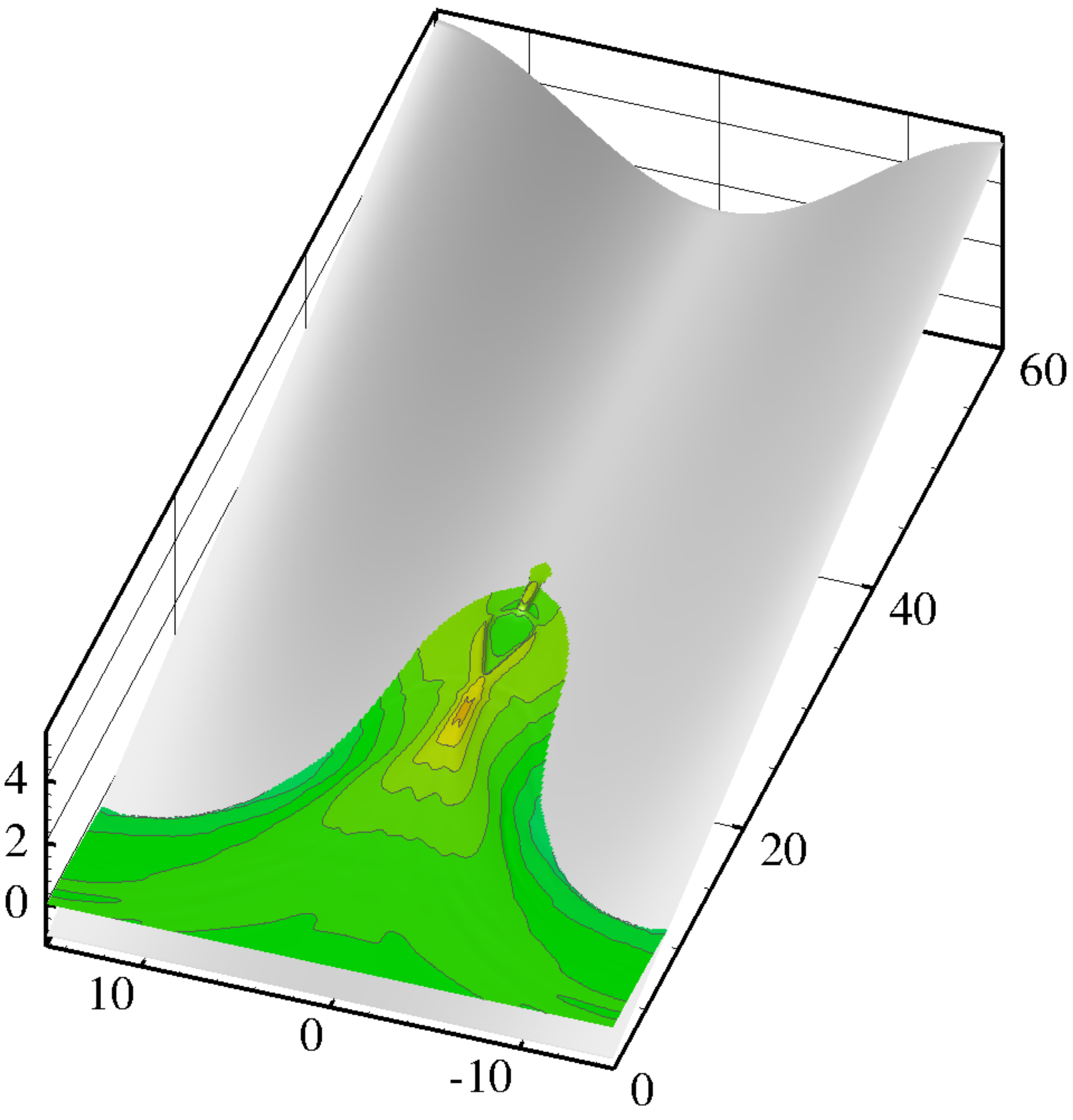
60
40
20
0
4
2
0
10
0
-10

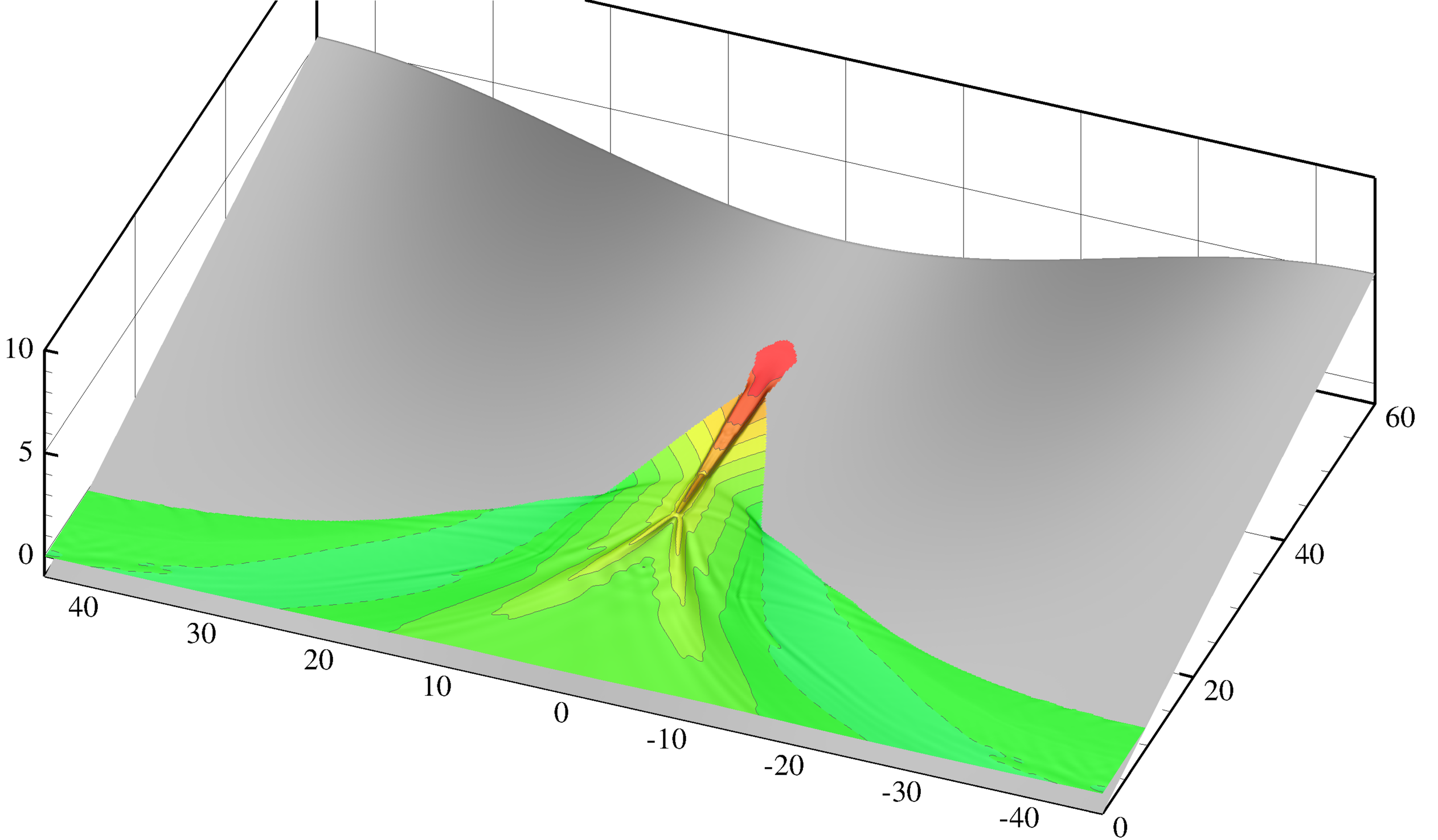
10
5
0
40
30
20
10
0
-10
-20
-30
-40
0
20
40
60

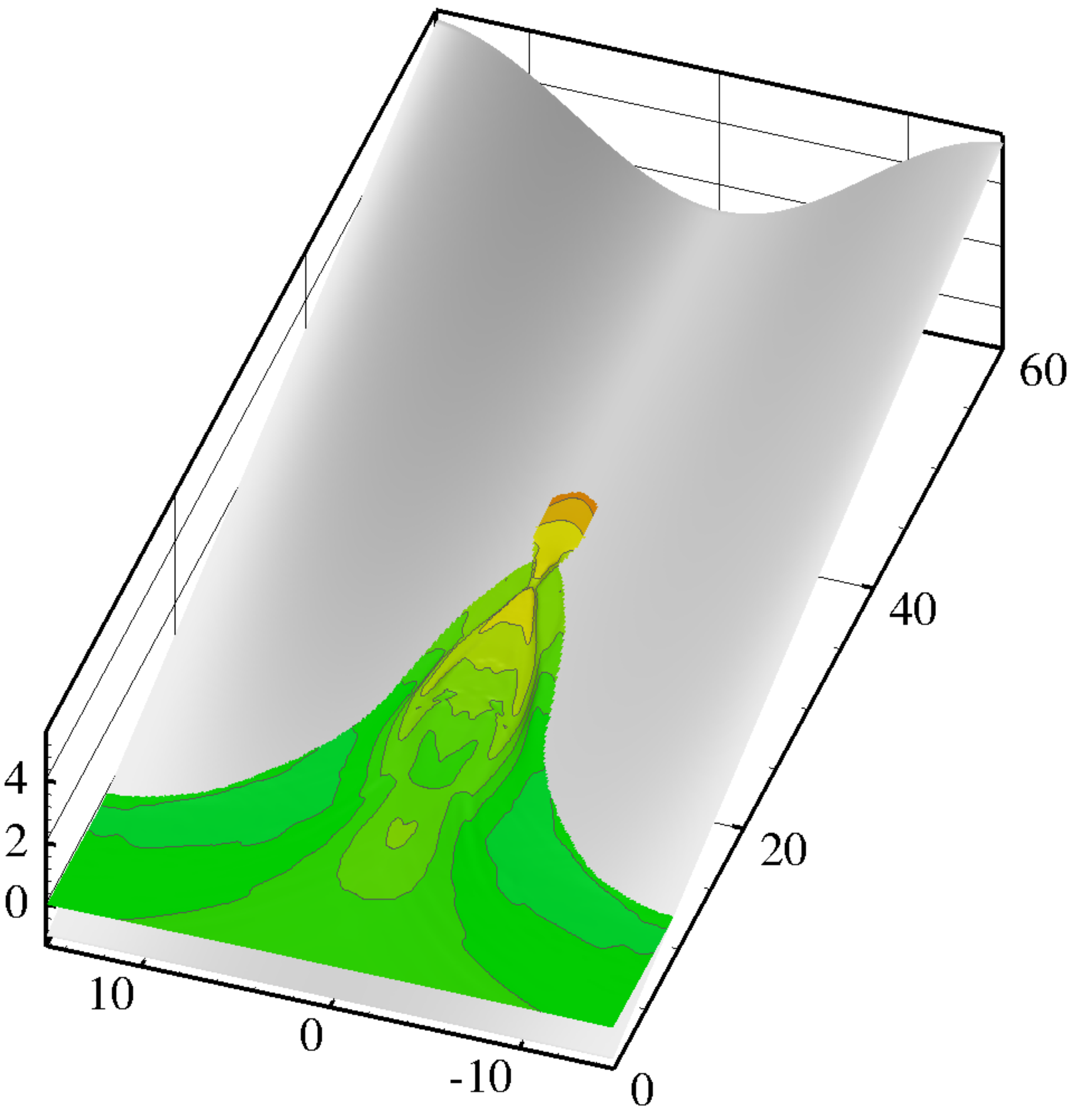
60
40
20
0
4
2
0
10
0
-10

-0.50 -0.38 -0.26 -0.15 -0.03 0.09 0.21 0.32 0.44 0.50

10
5
0

40 30 20 10 0 -10 -20 -30 -40

0 20 40 60

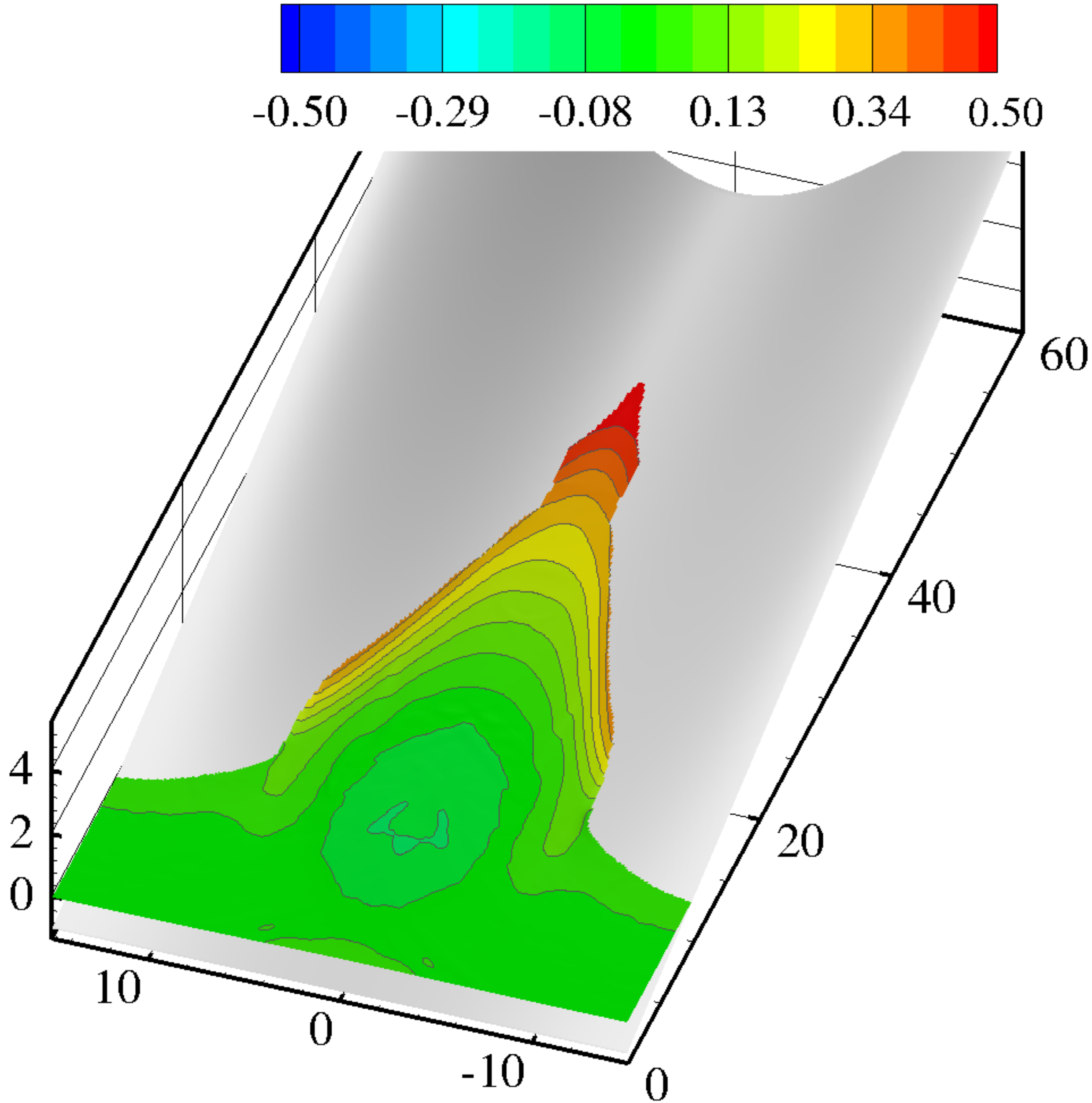
-0.50
-0.29
-0.08
0.13
0.34
0.50
60
40
20
0
-10
10
0
2
4

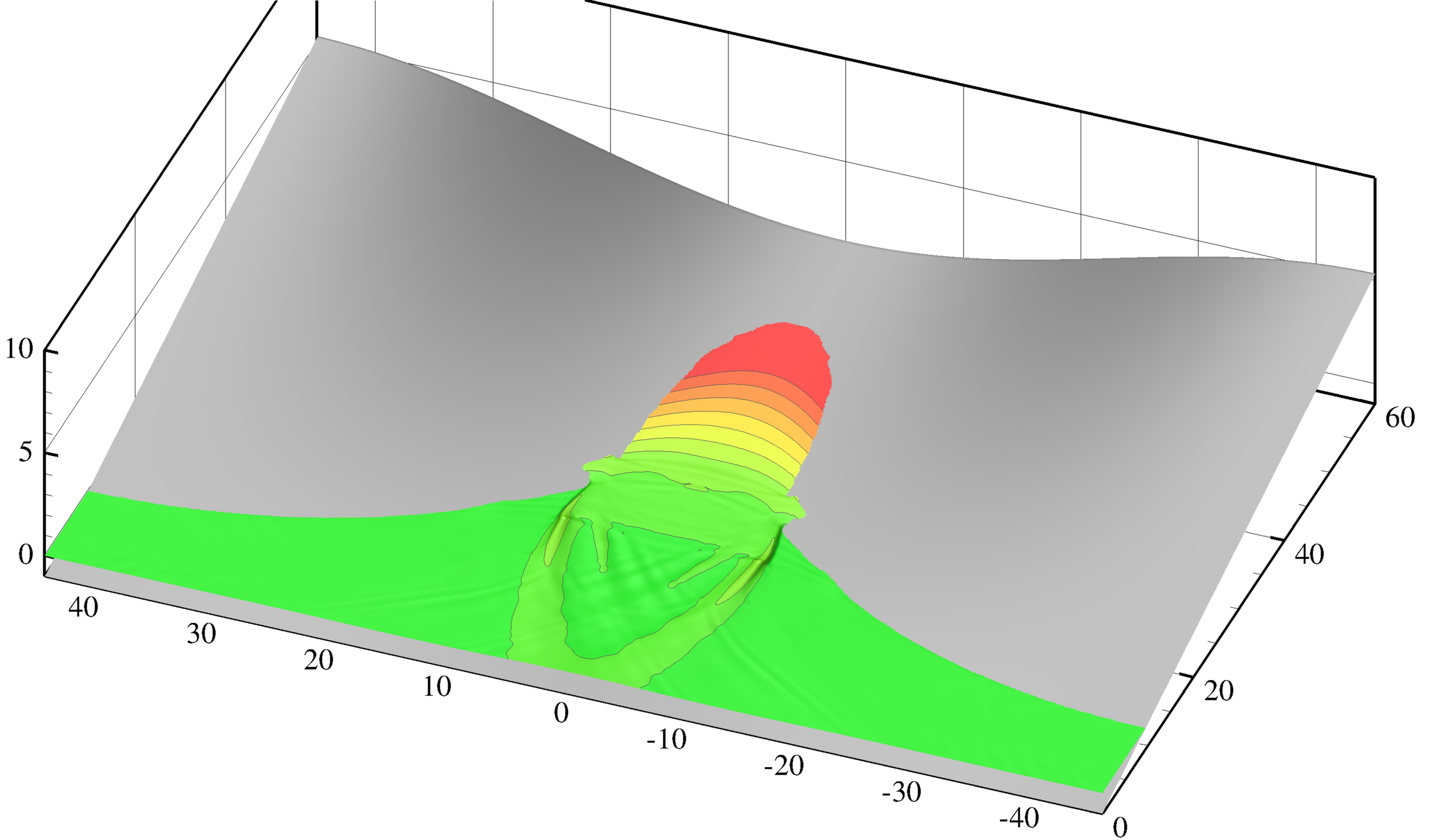
10
5
0
40
30
20
10
0
-10
-20
-30
-40
0
20
40
60

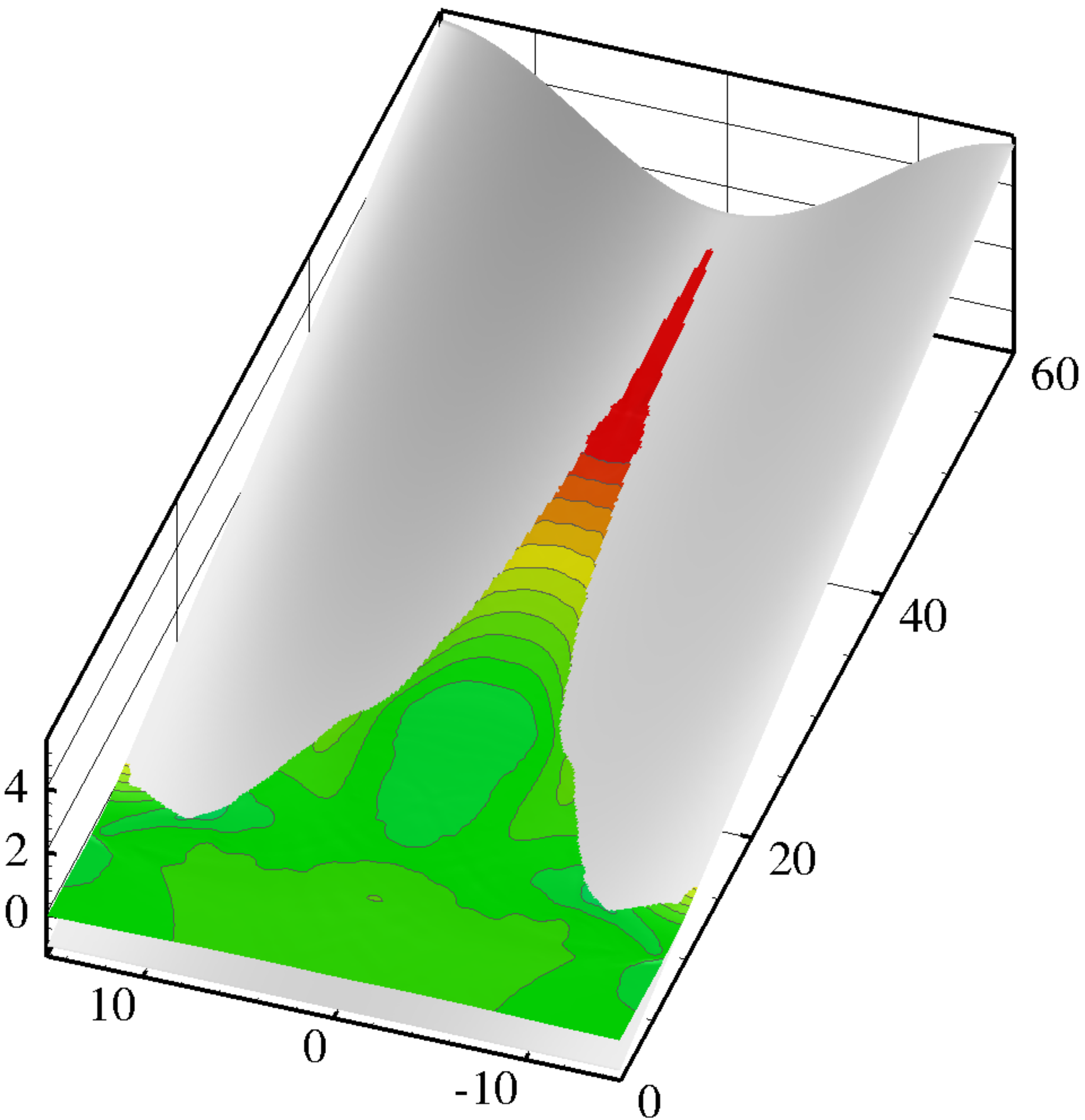
60
40
20
0
-10
10
0
2
4

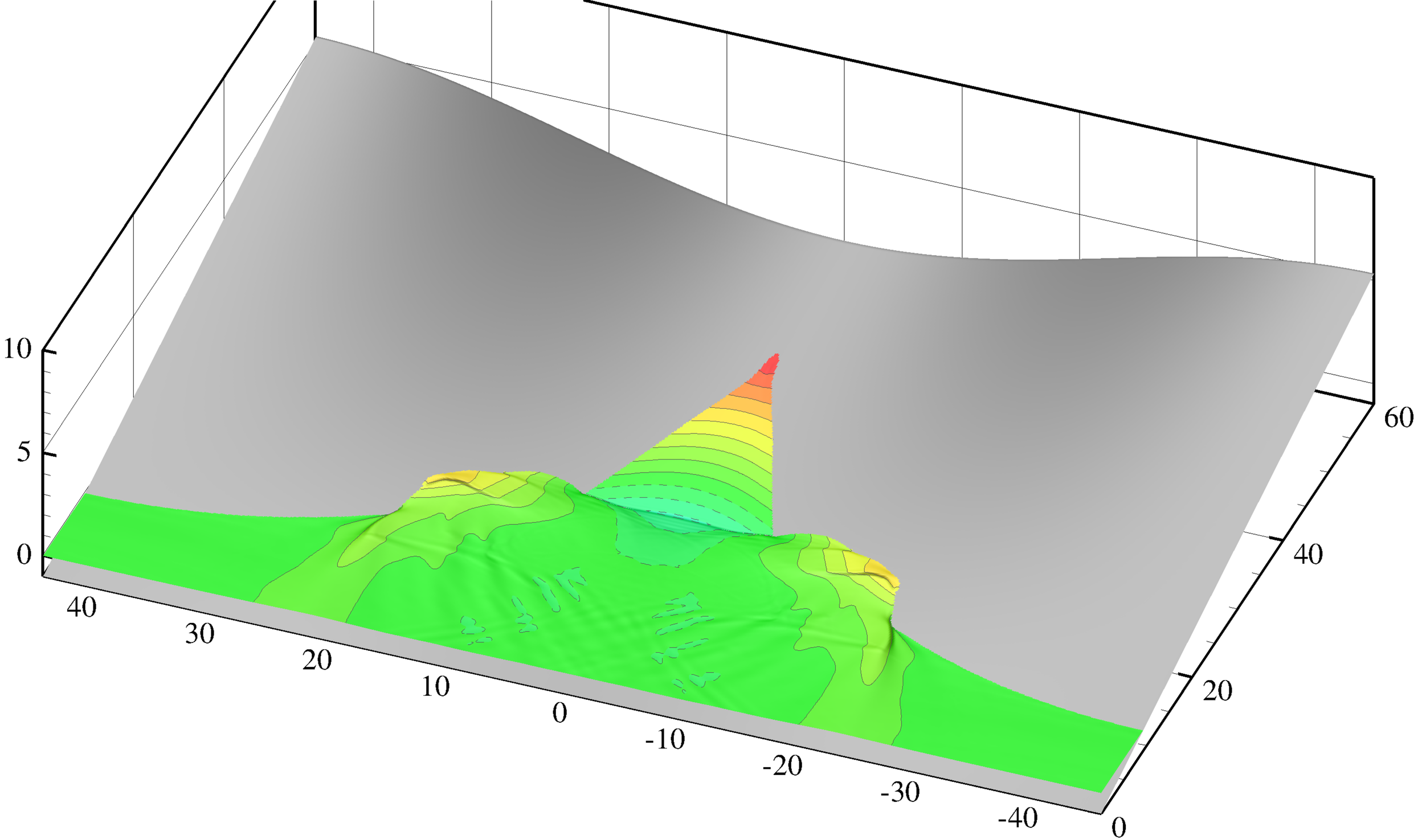
10
5
0
40
30
20
10
0
-10
-20
-30
-40
0
20
40
60

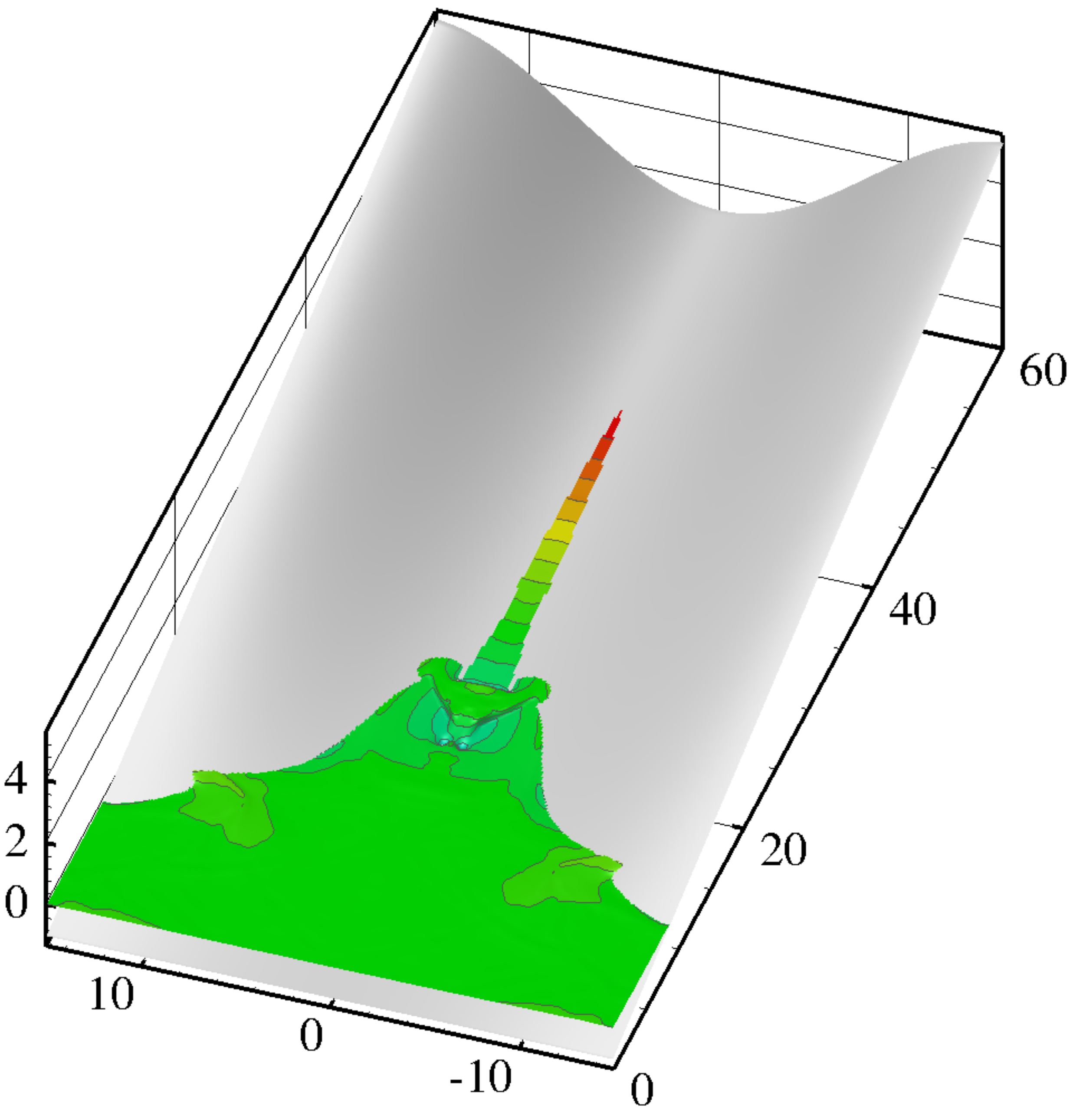
60
40
20
0
4
2
0
10
0
-10

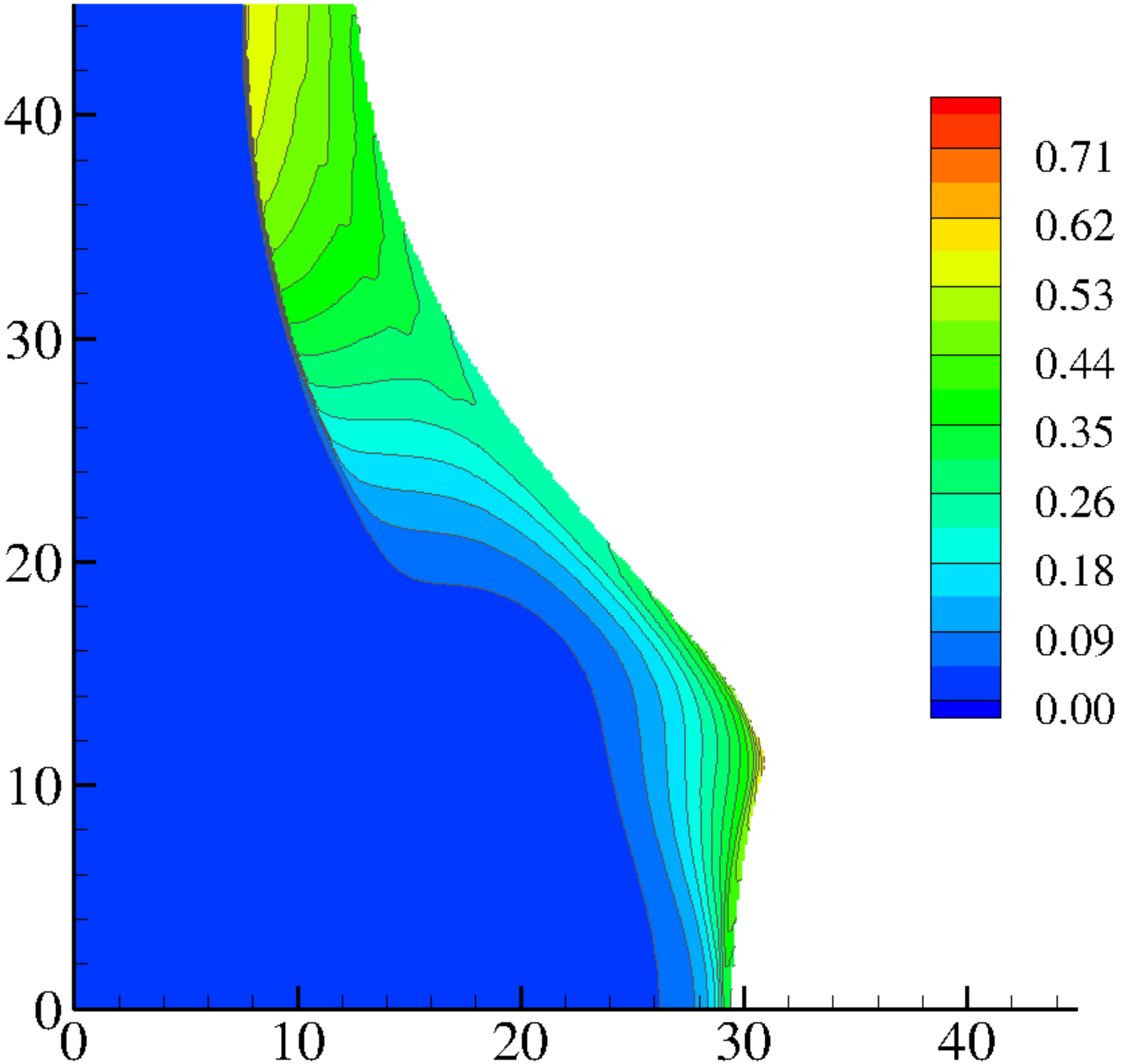
40
30
20
10
0
0
10
20
30
40
0.71
0.62
0.53
0.44
0.35
0.26
0.18
0.09
0.00

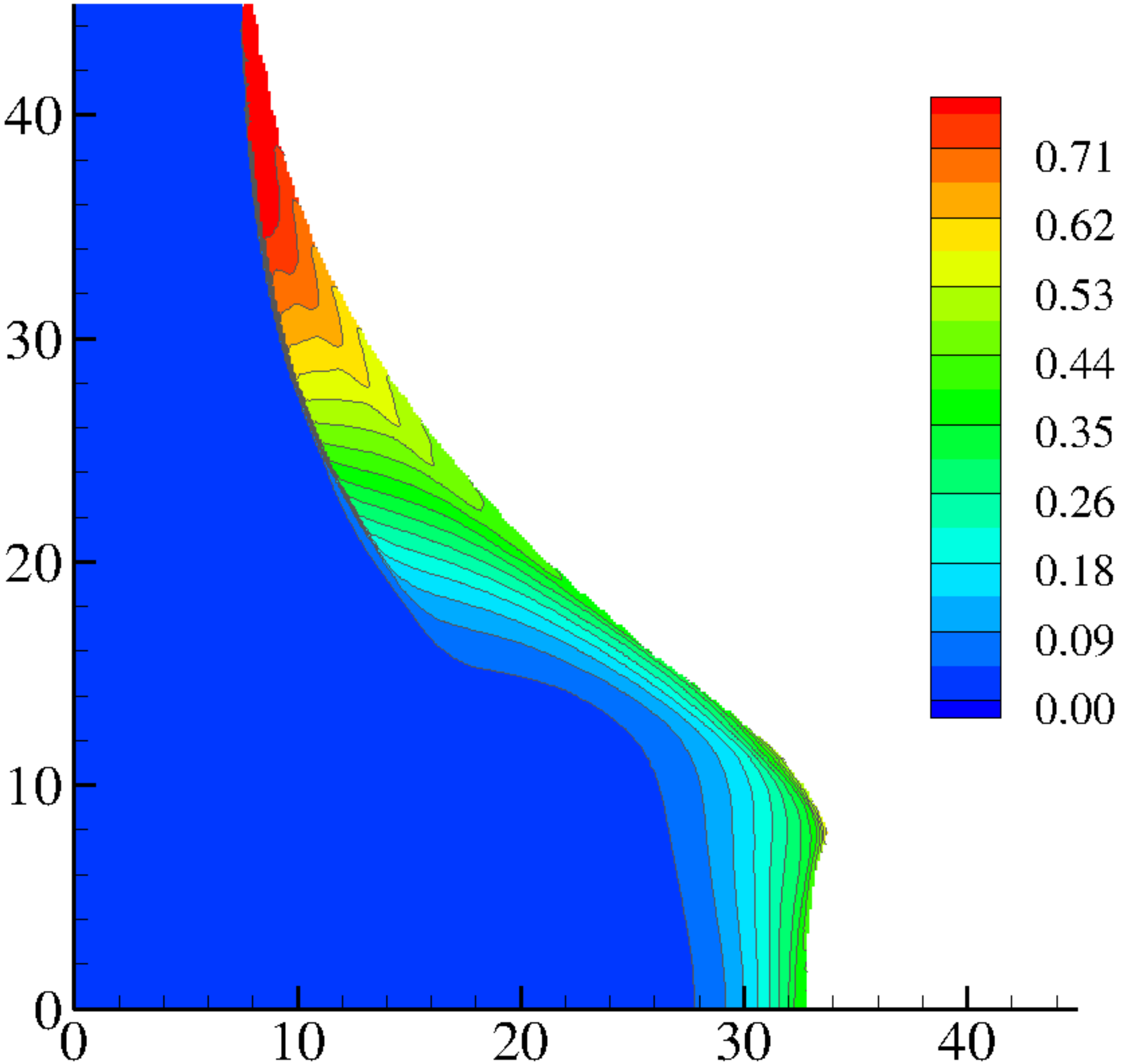
40
30
20
10
0
0
10
20
30
40
0.71
0.62
0.53
0.44
0.35
0.26
0.18
0.09
0.00

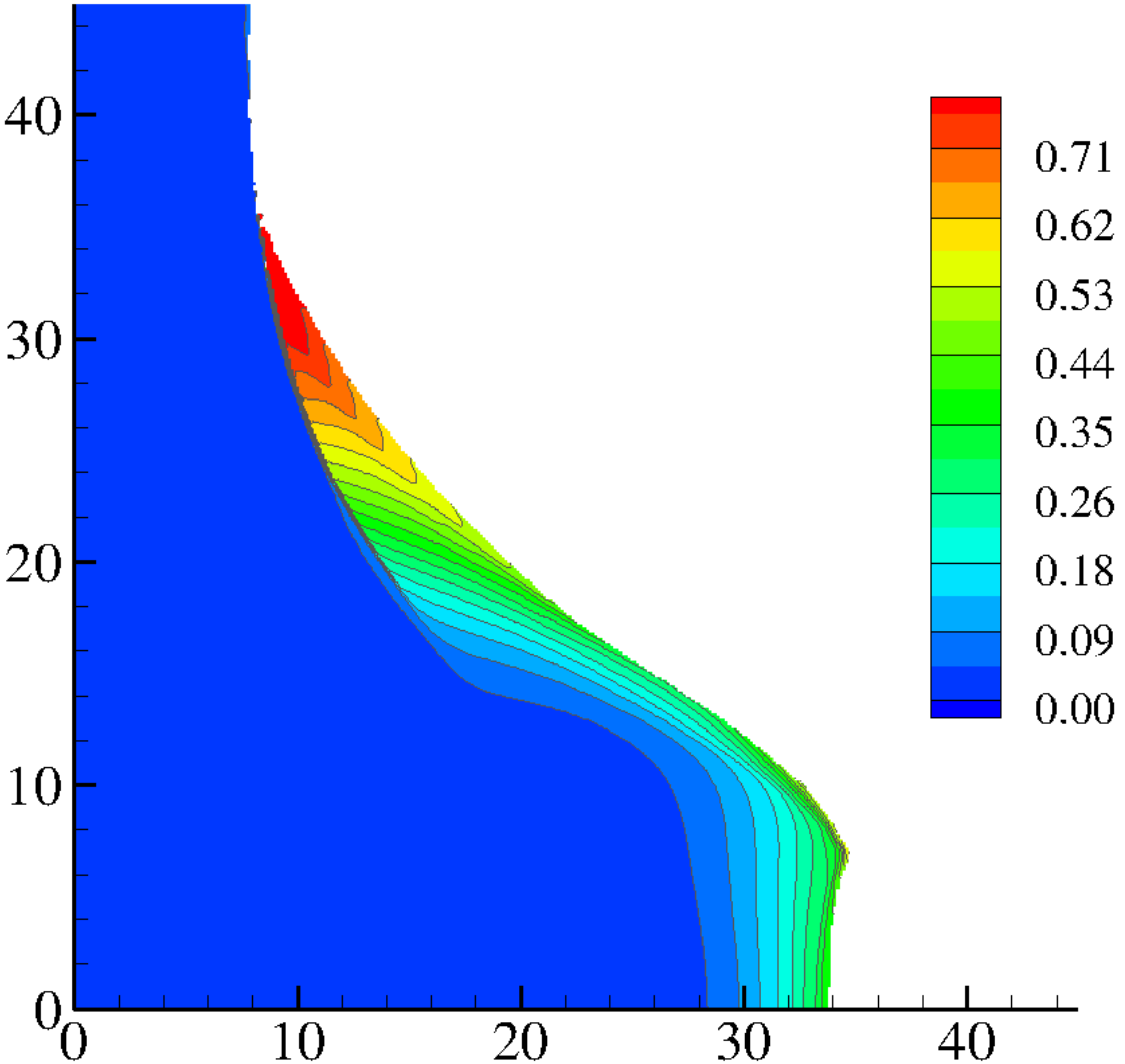
40
30
20
10
0
0
10
20
30
40
0.71
0.62
0.53
0.44
0.35
0.26
0.18
0.09
0.00

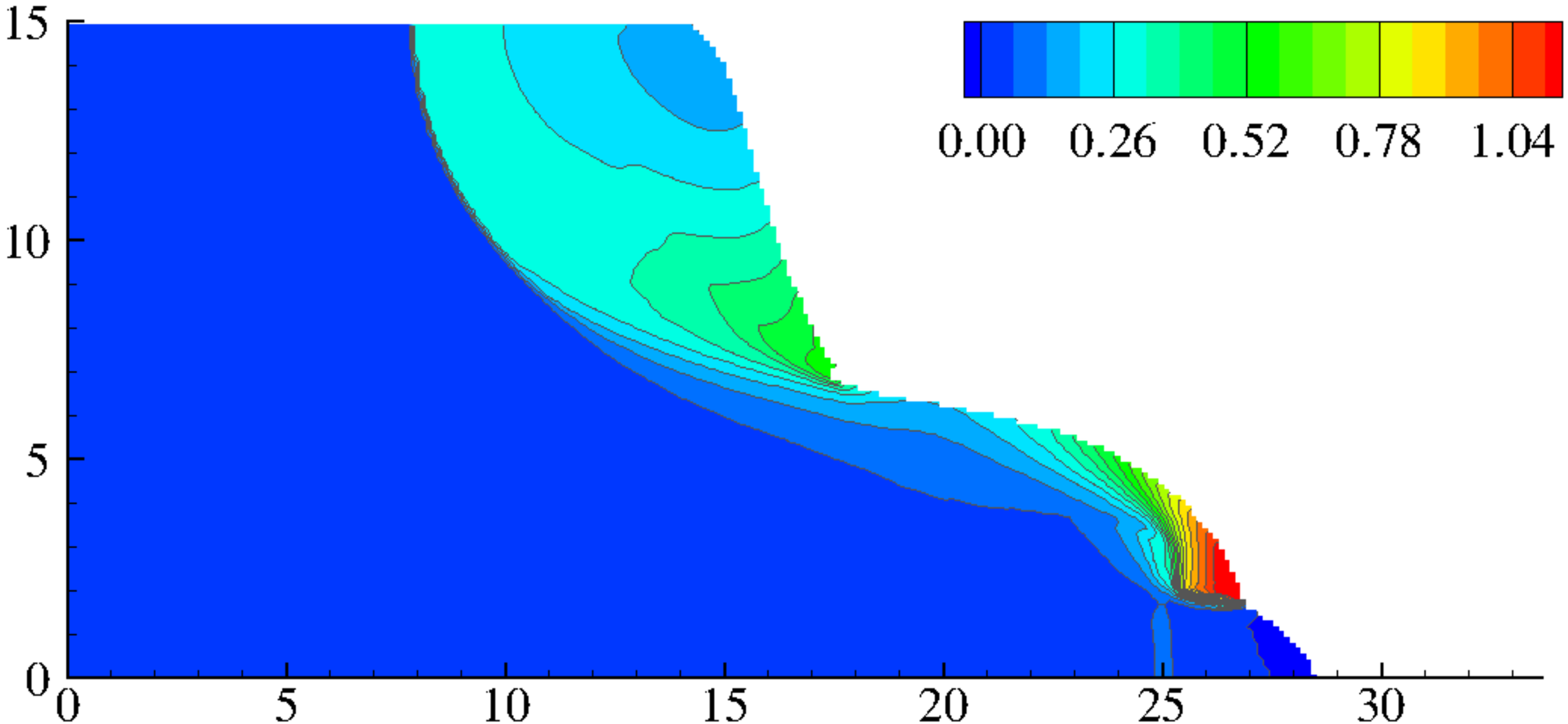
0.00
0.26
0.52
0.78
1.04
15
10
5
0
0
5
10
15
20
25
30

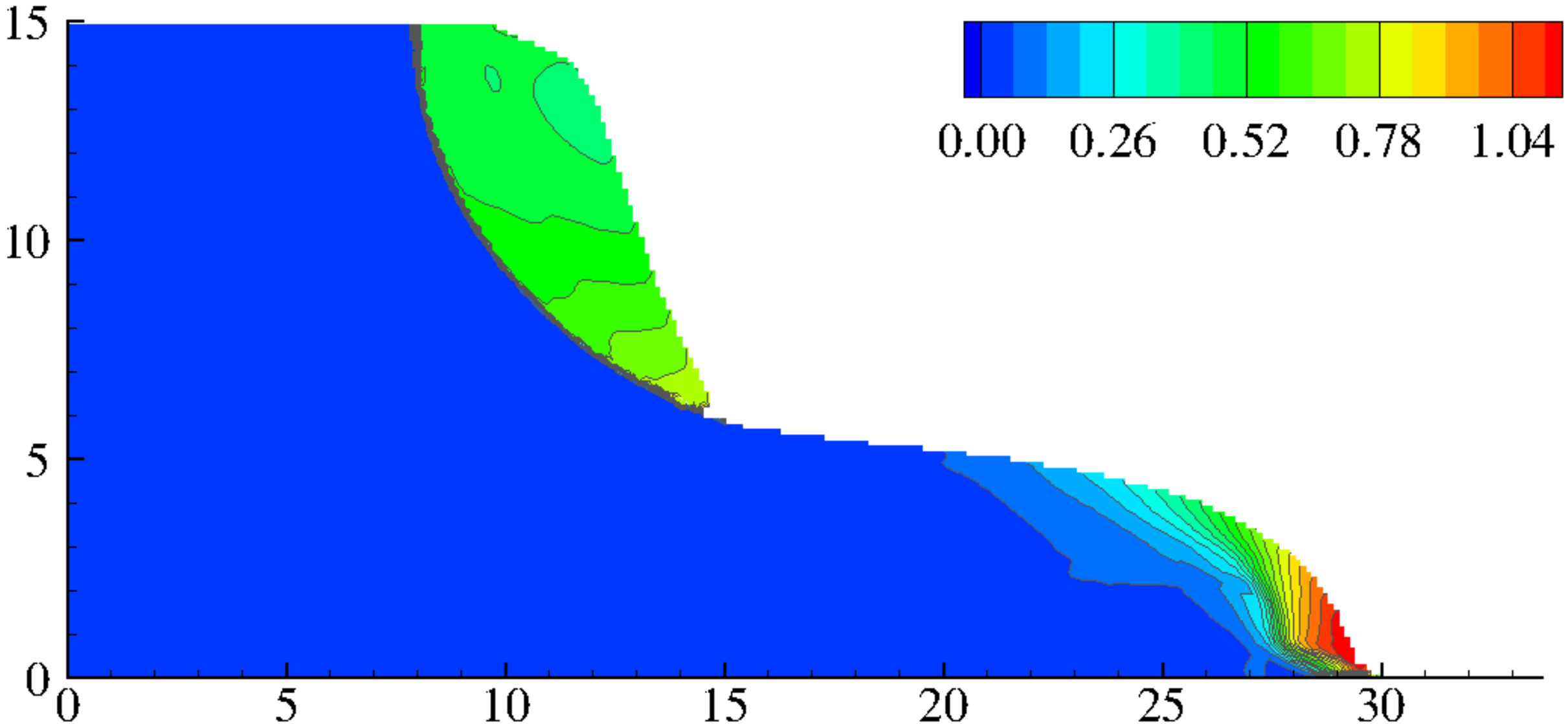
0.00
0.26
0.52
0.78
1.04
15
10
5
0
0
5
10
15
20
25
30